Doctoral Dissertation
Doctoral Program in Chemical Engineering (36th Cycle)

On the use of Computational Fluid Dynamics to assist modeling of pharmaceutical filling lines

By

Camilla Moino
******

Supervisor(s):
Prof. Pisano Roberto, Supervisor
Dr. Scutellà Bernadette, Supervisor
Prof. Boccardo Gianluca, Co-Supervisor

Doctoral Examination Committee:
Prof. Giuseppina Sandri, Referee, Università di Pavia
Prof. Matteo Icardi, Referee, University of Nottingham

Politecnico di Torino
2024

Declaration

I hereby declare that, the contents and organization of this dissertation constitute my own original work and does not compromise in any way the rights of third parties, including those relating to the security of personal data.

<div align="right">

Camilla Moino

2024

</div>

Acknowledgment

Gratitude also goes to the various researchers who reviewed our manuscripts. It may have seemed like a burden to me at the time, but in the end I always felt that their revisions contributed more value to the work.

A PhD is often seen as a journey of ups and downs, and no better description can be found for the last three years (and some change) of my life. Thanks to mom for always supporting me when things got tough, thanks to dad for always being proud of his daughter. Thanks to my siblings Carola, Andrea and Alessandra for heartening me during the journey. Thank you Greg for always being there when I need you.

Abstract

Fill-finish of protein-based parenteral formulations represents a crucial step in the pharmaceutical industry that necessitates careful monitoring of product stability down the line. Mixing, pumping, filtering, and filling are the most important steps which expose the parenteral product to various stressing conditions, including interfacial stress and shear stress. The combination of these elements is widely believed and proven to influence product stability, but the defined roles of these players in the product damage process have not yet been identified. The present work addresses a current industrial problem, by focusing on the analysis of shear stress on protein-based therapeutics flowing in filling lines by means of Computational Fluid Dynamics (CFD) simulations. The purpose of this work is not to pinpoint the mechanism triggering the damage of the product, but it represents the first step towards wider experimental investigations and introduces new strategies to quantify the average shear stress. First, an extended summary of existing literature that explores the experimental impact of shear stress in pharmaceutical operations is provided. Next, flow standard in tubing, fittings, sterilizing filtration, and pumping are analyzed. For each unit operation a specific path was followed to achieve a computational replica of the real geometry; standard flow conditions were then tested and the relevant shear stress exposures were investigated and further compared.

The field of scale-down approaches, used to scale the commercial process down to the laboratory level, is also explored with the aid of CFD modeling. Since quality control is critical in the pharmaceutical realm, it is essential that the scale-down approach preserves the same stress exposure as the commercial scale, which in the present work is considered to be that resulting from shear effects. Therefore, innovative approaches for scaling down the commercial process are proposed and numerically validated. The numerical work presented in this project helps to shed light in a field that has seen some confusion in the literature. Shear stress indeed contributes synergistically to product damage when combined with interfacial stress. Knowing the extent of shear is therefore the first step toward addressing the industrial problem and is precisely the goal and outcome of this project. Given a line component and its operating conditions, the proposed workflows allow estimation of the mean shear stress and fluid dynamics analysis. In the future, a coupling of CFD with experiments could facilitate even more targeted controls on product stability.

Contents

Nomenclature

A	streamline area of influence, m^2
C	filtration capacity, m^3
C_f	skin friction factor, -
CV	coefficient of variation, -
d	tubing diameter, m
DCF	damage critical factor, -
DF	damage factor, -
DFF	damage fitting factor, -
EFA	Effective Filtration Area, cm^2
k	porous medium permeability, m^2
L	characteristic length, m
p	pressure, Pa
$\Delta P/L$	pressure drop over porous medium length, kg m^{-2} s^{-2}
Q	volumetric flowrate, m^3 s^{-1}
R	tubing radius, m
Re	Reynolds number, -
St	Stokes number, -
SF	Safety Factor, -
SH	shear history, -
t	time, s
T	temperature, K
u	fluid velocity, m s^{-1}
V	filtration capacity or Darcy velocity, m s^{-1}
w	volumetric flowrate weight, m^3 s^{-1}
x	spatial coordinate, m

Greek letters

γ	shear rate, s^{-1}
ε	porous medium porosity, -
κ	turbulent kinetic energy, m^2 s^{-2}
μ	dynamic fluid viscosity, kg m^{-1} s^{-1}

μ_T	turbulent eddy viscosity, kg m^{-1} s^{-1}
ν	kinematic viscosity, m^2 s^{-1}
ν_T	turbulent kinematic viscosity, m^2 s^{-1}
ρ	fluid density, m^3 kg^{-1}
σ	shear stress, Pa
τ	residence time, s
Γ	filtered shear rate, s^{-1}
ω	specific turbulent dissipation rate, s^{-1}

Subscripts

c	commercial
fit	fitting
i	index
j	index
l	laboratory
lam	laminar
max	maximum
ms	microscale
out	outlet
p	particle
ta	time-averaged
$theo$	theoretical
tot	total
$turb$	turbulent
$wall$	wall

Abbreviations

AFM	Atomic Force Microscopy
BSA	Bovine Serum Albumin
CD	Circular Dichroism
CDF	Cumulative Distribution Function
CFD	Computational Fluid Dynamics
CLSM	Confocal-Laser Scanning Microscopy
CT	Computed Tomography

DLS	Dynamic Light Scattering
DNS	Dinitrosalicylic acid
DSC	Differential Scanning Calorimetry
DSF	Differential Scanning Fluorimetry
EP	European Pharmacopoeia
FSC	Fluorescence Correlation Spectroscopy
GAMG	Geometric Agglomerated Algebraic Multigrid
HPLC	High-Performance Liquid Chromatography
IA	Image Analysis
LPT	Lagrangian Particle Tracking
mAb	Monoclonal antibody
MD	Molecular dynamics
MF	Microfiltration
MFI	Micro-flow imaging
NMR	Nuclear Magnetic Resonance
NTA	Nanoparticle Tracking Analysis
NS	Native State
PCS	Photon Correlation Spectroscopy
PDF	Probability Distribution Function
PIV	Particle Image Velocimetry
PLL	Poly-L-lysine
RANS	Reynolds Averaged Navier–Stokes
ROI	Region of Interest
SANS	Small-Angle Neutron Scattering
SDS-PAGE	Sodium Dodecyl Sulfate-Polyacrylamide Gel Electrophoresis
SE-HPLC	Size-exclusion High-Performance Liquid Chromatography
SEC	Size Exclusion Chromatography
SEC-MALS	Size Exclusion Chromatography-Multiangle Light Scattering
SEM	Scanning Electron Microscopy
SST	Shear Stress Transport
SVP	Subvisible Particle
TEM	Transmission Electron Microscopy
TFF	Tangential Flow Filtration
UF	Ultrafiltration
US	Unfolded State
USP	United States Pharmacopoeia
UV-vis	Ultraviolet-visible
WHO	World Health Organization

Chapter 1

Introduction

1.1 Modeling of filling lines

Fill finish of protein-based parenteral drug product is a pharmaceutical process broadly used to fill sterile drug products into vials or syringes; the process is comprised of different steps, including pumping, sterile filtration, and final filling, as shown in **Figure 1.1**.
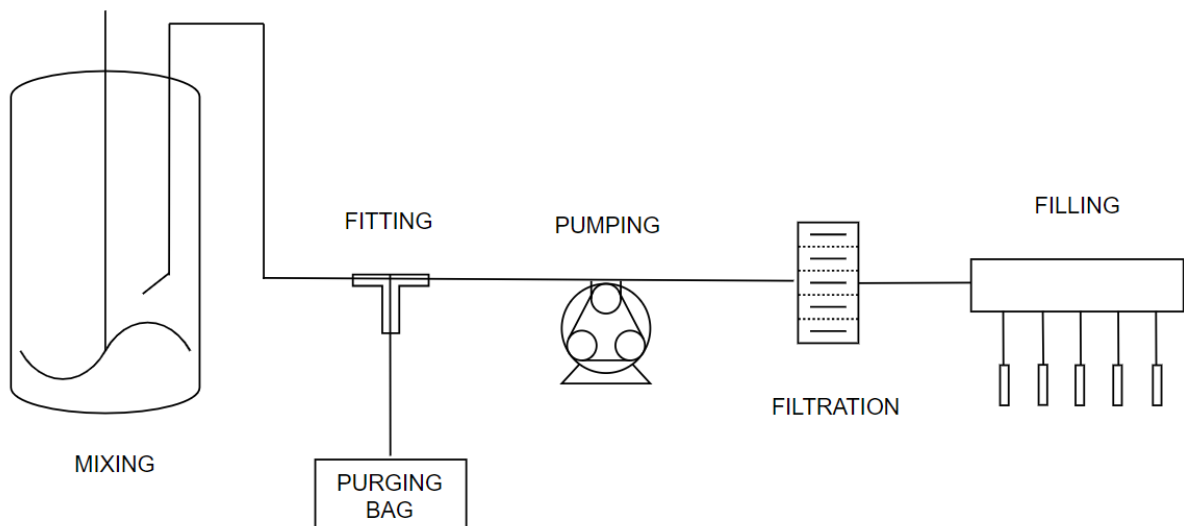
Figure 1.1 Typical filling line for parenteral drug products.

Mixing is a crucial step in drug production and, more specifically, ensures the homogeneity of the drug product before the formulation is filled (Das et al., 2022). It generally requires high turbulence to guarantee perfect mixing of the reactants which, however, can threaten the stability of shear-sensitive products. A peristaltic pump moves the product through a smooth polymeric tubing, by compression and decompression (Ostadfar, 2016). This generates a pulsatile flow, whose period depends on the number of rollers and their relative speed (Zhou

et al., 2014). Before the final filling, the product is processed in a sterilizing filter; this pressure-driven technique pushes the product across a semi-permeable membrane in order to separate the contaminants from the solution and ensure the product meets the sterility criterion. In the next filling section the product passes rapidly through a filling needle and other small-diameter filling parts (Carpenter et al., 2009), which are generally much smaller than the tubing that goes into them (Joyce and Witchey-Lakshmanan, 2013). Finally, fittings of various shapes (T-, Y-) are often present in the line to allow product sampling (WHO, 2005). This may be necessary for many reasons, which include pre-qualification, acceptance of consignments, and in-process control. **Figure 1.1** shows an example of a filling line. Operating conditions then depend on a number of factors, which include the properties of the product to be processed. Within this framework, the work here presented was conducted in collaboration with the pharmaceutical company GSK. It operates multiple filling lines, which differ in operating conditions and in process flow schemes.

Process validation is required in the biopharmaceutical industry to verify product conformity and safety (Rathore and Sofer, 2005). A proper understanding of each stage is therefore mandatory and the potential promotors to product instability must be identified. Among these actors, shear stress also seems to play a key role (ICH, 1996) and is particularly feared because of its ubiquitous presence in filling lines. Several authors tried to shed light on the actual impact of shear stress on protein-based products (Bee et al., 2009; Jaspe and Hagen, 2006) but the presence of additional stressors, i.e., interfacial stress, complicated the interpretation of the results. In this controversial landscape, it is therefore necessary to quantify shear stress in the operating units of the filling process as a first step for broader experimental investigations.

Several strategies can be used to quantify shear stress, via experimental or numerical analysis. Experimental methods are generally classified as direct or indirect devices. Direct devices measure the wall shear stress's integrated force on a flush-mounted floating element and allow for real-time measurement (Li et al., 2016), but show high sensitivity to external noise (Winter, 1979) which limits their use at industrial scale. Optical and thermal sensors are the most popular indirect devices. Particle Image Velocimetry (PIV) is an optical, non-intrusive technique that allows to obtain the entire, instantaneous flow from two high-speed images (Roghair et al., 2014) and therefore calculates the shear stresses (Scharnowski et al., 2010). On the other hand, PIV has a well-known challenge in shear stress estimation (by biasing the velocity gradients in the near-wall region (Kefayati et al., 2014)), and is generally very expensive (Lopez-Gavilan and Barrero-Gil, 2023); in particular, the high cost represents a practical barrier to the widespread use of PIV. Similarly, wall shear stress is estimated starting from the velocity profile measurements by Laser Doppler Velocimetry (LDV) (Anderson, 2019). Finally, thermal sensors work on temperature transduction to voltage; they are designed to achieve fast response time and high sensitivity but might be affected by measurements errors because of the temperature drift. It is worth noting that these methods allow the estimation of local field only, i.e., wall shear stress. An alternative to direct and indirect measurement of the shear stress is represented by numerical analysis. In particular, Computational Fluid Dynamics (CFD) modeling is non-invasive, does not use any product and allows for estimation of full-

field data. This uses mathematical modeling and numerical methods to analyze and solve problems in fluid dynamics (Versteeg and Malalasekera, 2007). CFD is experiencing significant growth in pharmaceutical applications, as it can accelerate product and process development, facilitate optimization of existing processes, energy savings, and efficiency.

In the pharmaceutical field, through knowledge and control of the process, batch failures are minimized (Rathore and Sofer, 2005). In this scenario, scale-down models ease the translation from commercial to laboratory scale, as shown in **Figure 1.2**; they are indispensable for process development, characterization, optimization, and validation (Moscariello, 2016). With a scale-down model, process developers can evaluate the parameters by which a process would run correctly (Mirasol, 2019).
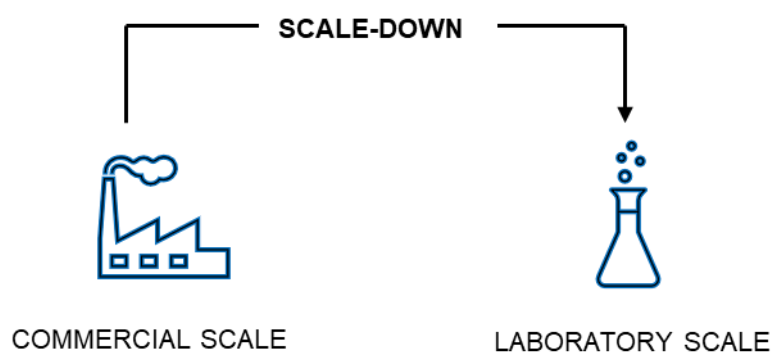
Figure 1.2 Scale-down operation in the pharmaceutical field.

More specifically, they allow accurate characterization of the commercial process by performing process evaluations at the laboratory level, resulting in a design space of the process that enables the control of the pharmaceutical product's Critical Quality Attributes. Such analyses are not feasible or cost-prohibitive at the commercial unit. In general, two processes are similar if they possess a geometric, kinematic, and dynamic similarity. Geometric similarity requires that linear dimensions of the original and the scaled-down systems are scaled by the same ratios (Byron Bird et al., 2002). In turn, kinematic similarity requires geometric similarity, and the same ratio scales the velocities. Finally, dynamic similarity requires both geometric and kinematic similarity, and adds the condition that characteristic forces scale by the same ratio: specific dimensionless groups in the differential equations and boundary conditions must be the same. To provide an example, Reynolds number can be used to scale industrial processes; by definition, it is derived to describe the physical system in a scale-independent manner (Al-Chi et al., 2013).

A common practice in pharmaceutical operations prescribes the replication in a laboratory unit of the worst-case scenario of the commercial line, in order to identify and employ a reasonable safety margin (Levin, 2001). However, this method is time- and product-consuming, and it is not possible to make predictions in case of changes from the standard conditions of the line.

1.2 Scopes of the project

Given the high variability in terms of process flow schemes and operating conditions, mathematical-based modeling of a filling line is highly necessary. First, a scouting of the various lines is conducted in order to gather relevant information and identify appropriate case studies to be analyzed. Then, CFD analysis is adopted to investigate the fluid dynamics within some of these typical filling operations. More specifically, analysis is conducted on tubing, fittings, sterilizing filtration, and peristaltic pumping. As far as operating conditions, those generally used at the industrial case are considered and both laminar and turbulent regimes are considered. The mixing operation is not explored as extensive literature has been already devoted to the case (Mishra et al., 2021; A. S. Rathore et al., 2012) and was not requested by the company with which the project was collaborated.

Novel strategies are developed to estimate the average shear stress experienced by the product when flowing through each component. The field of scale-down approaches, used to scale the commercial process down to the laboratory level, is also explored. They allow to perform product characterization experiments using smaller volumes of the drug products. New approaches for scaling down the commercial process are proposed and are compared to current scale-down approaches. These latter are based on the so-called design of experiments or worst-case scenario, which generally require large amount of product and do not allow to conduct prevision in case of deviation from standard conditions.

1.3 Research questions

The present work aimed at addressing some very important scientifical industrial questions which are summarized below:

1. How does CFD fit into the current state of the art of shear stress modeling? How does CFD provide aids for industrial practices?

2. Is it possible to derive modeling-based scale-down approaches which ensure representativeness between laboratory and commercial scales?

3. Given that the role of the exposure time to a defined shear stress is not universally understood, how to take into account the time of exposure when estimating the average shear stress?

4. Is the proposed shear stress estimation strategy extendable to other components of the line? Are comparisons within equipment possible?

5. Which unit operation of the filling line exposes the product to the maximum shear stress? How do you move from a single block process view to an overview along the entire process line?

6. What are the perspective of CFD modeling for filling lines, especially from an experimental perspective?

1.4 Thesis structure

1.4.1 Outline of the work

The thesis is divided into several chapters.

Chapter 1 frames the industrial problem under study and poses some research questions.

Chapter 2 surveys a review of works conducted to evaluate the impact of shear stress on pharmaceutical products and lays the foundation for the following modeling work.

Chapter 3 presents the theoretical background behind the different fluid dynamics conditions investigated and introduces the particle tracking techniques.

Next, *Chapters 4*, *5*, *6*, and *7* shows the methods and results of the different case studies investigated (tubing, fittings, sterilizing filtration, and pumping, respectively).

The thesis ends with *Chapter 8* where some final conclusions and remarks are drawn and answers to the initially posed research questions are provided.

1.4.2 Contributions of the thesis

The present work addresses a current industrial problem, by focusing on the analysis of shear stress on protein-based therapeutics processes through a filling line by means of CFD simulations. The purpose of this work is not to pinpoint the mechanism triggering the damage of the product, but to introduce new ways to model filling line's components and new strategies to quantify the average shear stress. Since scale-down approaches cover a pivotal role in the pharmaceutical industrial realm, extensive efforts were put in figuring out modeling-based scale-down strategies and constant support was given to the company in an effort to help conduct laboratory scale experiments.

Some of the results hereafter presented have been already presented in the following papers and conference proceedings:

- Moino, C., Scutellà, B., Bellini, M., Bourlès, E., Boccardo, G., Pisano, R., 2023. Analysis of the shear stresses in a filling line of parenteral products: The role of tubing. *Processes*, 11, 833.

- Moino, C., Scutellà, B., Bellini, M., Bourlès, E., Boccardo, G., Pisano, R., 2023. Analysis of the shear stresses in a filling line of parenteral products: The role of fittings. *Processes*, 11, 1797.

- Moino, C., Agostini, E., Scutellà, B., Albano, A., Bellini, M., Bourlès, E., Boccardo,

G., Pisano, R., 2024. Analysis of the shear stresses in a filling line of parenteral products: The role of sterilizing filters. *Separation and Purification Technology*, 344, 127248.

- Moino, C., Albano, A., Scutellà, B., Boccardo, G., Pisano, R., 2024. Analysis of the shear stresses in a filling line of parenteral products: The role of peristaltic pumping. *Pharmaceutical Development and Technology* (submitted).

- Moino, C., Artusio, A., Pisano, R., 2024. Shear stress as a driver of degradation for protein-based therapeutics: More accomplice than culprit. *International Journal of Pharmaceutics*, 650, 123679.

- Moino, C., Scutellà, B., Bellini, M., Bourlès, E., Boccardo, G., Pisano, R., 2022. Analysis of the shear stresses in a filling line of parental products: the role of tubing and fittings. PBP conference (poster presentation).

- Moino, C., Scutellà, B., Albano A., Bellini, M., Bourlès, E., Boccardo, G., Pisano, R., 2023. Analysis of the shear stresses in a filling line of parenteral products. PDA conference (poster presentation).

- Moino, C., Scutellà, B., Albano A., Bellini, M., Bourlès, E., Boccardo, G., Pisano, R., 2023. Scale-down modeling of the filling process for vaccine production. ECCE ECAB (oral presentation).

- Moino, C., Scutellà, B., Albano A., Bellini, M., Bourlès, E., Boccardo, G., Pisano, R., 2023. Scale-down modeling of the filling process for protein-based parenteral drug products. AAPS (poster presentation).

- Moino, C., Scutellà, B., Albano A., Bellini, M., Bourlès, E., Boccardo, G., Pisano, R., 2023. Scale-down modeling of the filling process for protein-based parenteral drug products. In: *Proceedings of the 2023 AIChE Annual Meeting, Orlando (FL, USA), November 5-10, 2023*.

Chapter 2

How shear stress concerns pharmaceutical operations: synergistic combination with interfacial stress

Process validation is required in the biopharmaceutical industry to verify product conformity and safety (Rathore and Sofer, 2005). Understanding and controlling each stage of the process is thus mandatory (Conner et al., 2014; Shire, 2009), with particular attention to those aspects that can lead to out-of-specification products. A key aspect of the biopharmaceutical industry regards the preservation of biotherapeutics stability, which guarantees drug safety and efficacy. The stability of a pharmaceutical product is defined in the World Health Organization (WHO) guidelines on stability testing of pharmaceutical products as 'the ability of a pharmaceutical product to retain its chemical, physical, microbiological and biopharmaceutical properties within specified limits throughout its shelf-life' (WHO, 1996). A product may be sensitive to numerous stability stressors, such as temperature changes, oxidation, light exposure, ionic strength, and shear, as discussed in the International Conference of Harmonization's topic Q5C, (ICH, 1996). In particular, shear is gaining increasing attention due to its frequent occurrence in manufacturing lines*. Exposure to shear stress conditions can induce aggregation and particle formation, altering the drug's biological activity and raising the potential for side effects (Wang et al., 2010).

Along with shear stress, interfacial stress is another potential contributor to product instability, whose control is not straightforward. Aggregation of therapeutic proteins can result from stresses encountered at vapour-liquid, solid-liquid, and liquid-liquid interfaces (Babinchak and Surewicz, 2020; Duerkop et al., 2018a; Perevozchikova et al., 2015). A recent theory holds that the loss in product stability in a bioprocessing line is due to the combined effect of interface and shear stresses, and it is unlikely that shear stress alone causes protein aggregation (Nesta et al., 2017).

---

* The literature review addressed in this chapter has been previously published in "Moino, C., Artusio, F., Pisano, R., 2024. Shear stress as a driver of degradation for protein-based therapeutics: More accomplice than culprit. *International Journal of Pharmaceutics*, 650, 123679".

Nevertheless, it is practically difficult to deconvolute the effects of shear and interfacial stresses on product stability. Much work has been invested in figuring out how to evaluate the impact of shear stress on protein stability. In this sense, separating shear forces from other denaturation factors, mainly solid-liquid and air-liquid interfaces, poses unique challenges since it is difficult to quantify shear stress under interface-free conditions. The values of shear stress threshold appear not only dependent on the determination method, i.e., the flow condition in the adopted device, but also on the evaluated product (Sieck et al., 2013). For instance, Brückl et al. (Brückl et al., 2016b) found that shear stress was unlikely to unfold rhGH, IgG1 up to shear rates of at least 10^4 s^{-1} under interface free conditions. Nonetheless, in another work (McBride et al., 2015), even lower shear rates were able to promote aggregate formation for human insulin. If finding the shear stress threshold experimentally is not straightforward, molecular dynamics (MD) approaches could potentially come to the rescue to study protein behavior upon shear. A recent study focusing on the rotational dynamics of a small protein, i.e., ubiquitin, under different shear flows highlighted that MD can help understanding the effects of mechanical stress induced by shear flow on proteins (Papež et al., 2023).

This chapter provides a review of the effect of shear stress on protein-based drug products in major filling line operations. Recommendations for limiting the negative effects caused by shear stress are also presented. Finally, several devices developed in the literature to evaluate the impact of shear stress on product stability are discussed. Many works are thus cited, both experimental and numerical. This shows the relevance of the industrial problem studied, which in the present attempt is analyzed from a computational point of view, laying the foundation for future experimental investigation.

2.1 Background

2.1.1 Shear stress

Various forces can be exerted on a fluid element. Among these, it is worth mentioning viscous stresses, which are defined as a force per unit area acting on a fluid element and are commonly expressed in Pa. These stresses can be classified into two categories:

- Normal stresses if applied perpendicularly to the surface;
- Shear stresses if applied tangentially to the surface and generated by velocity gradients in the fluid.

For clarity, **Figure 2.1** shows the viscous stresses (τ) that can act on an element isolated from a generic fluid.
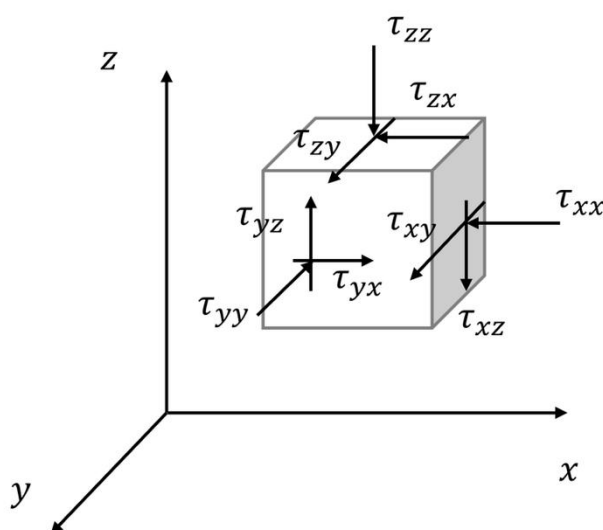
Figure 2.1 Viscous forces acting on a fluid element.

The viscous stress is a tensor composed of three normal components and six shear components. The fluid velocity gradient is defined as the shear rate (γ), which has units of inverse time (s^{-1}) (Bekard et al., 2011a). The forces that the fluid in motion exerts on the surface of an immersed body (i.e., a protein) are the integral over the surface of the viscous shear and the normal stresses.

In most cases, the rheological behaviour of formulations containing therapeutic proteins can be assimilated to that of Newtonian fluids, except for highly concentrated drug products, which may exhibit shear thinning behaviour (N. Rathore et al., 2012). For such non-Newtonian fluids, a non-monotone relation exists between the shear stress and the shear rate (Malkus et al., 1990).

2.1.2 Protein structure

Proteins are complex structures made of polymer chains, whose building blocks are named amino acids. It is essential to distinguish configuration and conformation when dealing with protein structure. The former is the absolute arrangement of atoms in space around a given atom, while the latter refers to the tri-dimensional arrangement of groups of atoms that can change without breaking any covalent bond. Given this premise, proteins can assume an infinite number of conformations, since they are composed of many single bonds that are free to rotate. However, under normal biological conditions, proteins only assume a few of the most stable conformations, which are critical in determining the specificity of proteins' biological functions. In this framework, the folding mechanism holds a great deal of biological importance (Creighton, 1990; Whitford, 2005). This mechanism involves an orderly sequential process, which gives the polypeptide the lowest possible energy state. The folding process involves a reversible reaction that is described as:

$$US \underset{k_2}{\overset{k_1}{\rightleftharpoons}} NS$$

(2.1)

where the equilibrium is shifted to the right so that the native state (NS) is more stable than the unfolded state (US). Therefore, proteins are said to be in their native state when their conformation is adequately folded and assembled with operative structure and function. Typically, the native state is the most stable among all the protein conformations and corresponds to minimum free energy. The conformation stability is then identified in terms of the unfolding Gibbs free energy difference (Pace et al., 1997) as follows:

$$\Delta G^0 = -RT lnK$$

(2.2)

where K is the unfolding kinetic constant, R is the universal gas constant, and T is the temperature.

An appropriate tertiary folded structure ensures the protein's biological activity. However, a protein may be reversibly unfolded in several ways (Lapidus, 2017) and chemical denaturants, e.g., guanidine hydrochloride and urea, are often used to promote its unfolding. Protein unfolding can also be fostered by acting on environmental conditions, e.g., increasing or decreasing temperature and pressure. Eventually, if proteins are exposed to viscous stresses, their unfolded state can become more energetically favoured and, hence, more likely to be populated by the protein (Jagannathan and Marqusee, 2013).

The unfolding process causes the protein to lose its compact conformation and, in some cases, its biological activity. Moreover, this process often promotes the formation of aggregates that, of course, are undesired for drug products (Devkate et al., 2016). The aggregation process may lead to soluble and/or insoluble aggregates which, under specific conditions, may precipitate (Mahler et al., 2009, 2005). Soluble aggregates can be reversible and have a low molecular mass. However, the soluble aggregates in a product should be no more than 5-10% because it is impractical to eliminate them above this threshold value (Wang et al., 2012). On the other hand, insoluble aggregates originate when protein aggregation exceeds the solubility limit. In such conditions, the aggregates become irreversible and precipitate out of the solution (Pham and Meng, 2020). The acceptable limit for insoluble aggregates correlates with the size of particulates detected in the protein solution upon reconstitution. Particles and protein aggregates in drug products are classified as visible particles if visible during visual inspection (Narhi et al., 2015), subvisible particles (SVP) if not visible during visual inspection (USP 788, 2006), and high molecular weight species. The advancement of particle detection techniques together with improved characterisation technologies set the framework for the current acceptance criteria for particle count (Ibrahim et al., 2023). As set forth by the United States Pharmacopoeia (USP) and the European Pharmacopoeia (EP), injectable solutions must be

"practically/essentially free of visible particles" (Den Engelsman et al., 2011). As for SVP, USP 788 prescribes limits of ≤ 6000/container and ≤ 600/container for sizes greater than 10 and 25 μm, respectively (USP 788, 2006). This criterium allows for low levels of particles, which also reduces risks of safety concerns due to insoluble particles.

2.1.3 Stress-induced protein instability

Several stressors have been identified as protein instability promotors, including interfaces (Babinchak and Surewicz, 2020; Duerkop et al., 2018a; Perevozchikova et al., 2015). Since proteins are surface-active molecules (Li et al., 2021), they frequently adsorb to interfaces, which could lead to conformation changes or even denaturation. During the development and manufacturing of therapeutics, proteins are subjected to interfacial stresses at each stage, because of the almost ubiquitous presence of air-liquid, solid-liquid, and liquid-liquid interfaces. Therefore, an accurate analysis to ensure the stability of protein molecules must be put in place. Several works investigated the instability resulting from the adsorption of proteins to an air-liquid interface (Duerkop et al., 2018a; Leiske et al., 2016; Maa and Hsu, 1997; Rospiccio et al., 2021); excipients like surfactants can be incorporated to the formulations in such a way to suppress such interfacial stress. Biologics are also vulnerable to exposure to solid-liquid interfaces, which are constantly present during the drug manufacturing process (Li et al., 2019) and whose effect has been thoroughly examined (Arsiccio et al., 2020, 2018; Arsiccio and Pisano, 2020). As an example, it was proven that insulin could adsorb to several types of containers, including glass vials, plastic vials, and infusion bottles; this significantly reduced the dose available for the patients (Weisenfeld et al., 1968). Unfolding and aggregation can result from protein adsorption to solid surfaces. Moreover, when the denatured proteins desorb from the solid surface, they can trigger protein aggregation in the bulk solution. Protein adsorption may also be promoted by the tube walls through which the therapeutic fluid flows (Deiringer et al., 2023). The choice of material is crucial to avoid clogging problems in any following filtration units. In fact, membrane fouling can result in decreased permeate flow, prolonged processing durations, and even process failure. Other than physical degradation, exposure to solid surfaces can also result in chemical degradation and protein cleavage (Li et al., 2019). A final class is represented by the liquid-liquid interface, which often occurs in delivery devices such as glass syringes. It is common practice to use silicon oil as a lubricant to allow a smoother sliding of the plungers within the barrels (Li et al., 2021). In such a case, proteins are known to unfold and form oil-protein particles at the lubricant–liquid interface of the syringe (Jones et al., 2005).

In the proteins' instability landscape, viscous stresses were suggested to be an additional driving force to the protein unfolding (Di Stasio and De Cristofaro, 2010), as discussed in Section 2.3.

2.2 Influence of shear stress in industrial applications

2.2.1 Shear stress in unit operations

Drug manufacturing includes various operations, namely 'formulation, fill and finish'. First, the purified form of the drug product is formulated with selected excipients; then, it is filled into vials or syringes and is thus ready for packing, labelling and quality inspection before its distribution (Patro et al., 2002). The filling process is critical for preserving product quality among the various steps. Mixing, pumping, filtration, and filling are typically involved in the filling process, as shown in **Figure 2.2**. The biotherapeutic formulations can be subjected to not negligible shear stresses during these unit operations.
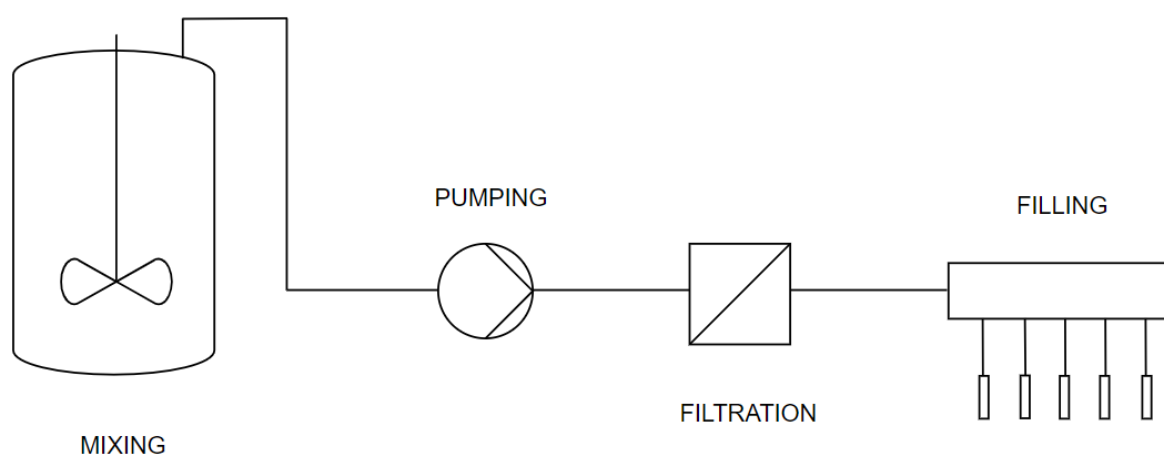
Figure 2.2 Typical steps of a filling line for drug products.

The formulated product may also be freeze-dried to increase biotherapeutic stability, improve shelf life, and facilitate storage. Recently, spray-freeze drying and spray-drying opened avenues for research to overcome some of the challenges associated with standard freeze-drying technologies (Sharma et al., 2021). Yet, shear stress can occur at some stages of the spray-freeze drying and spray-drying process, including the atomization step. **Figure 2.3** displays an example of a nozzle used for atomization.
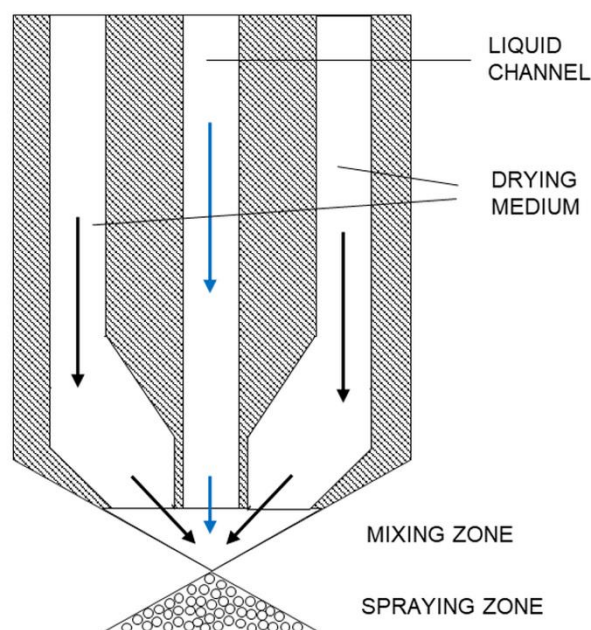
Figure 2.3 Schematic diagram of an external two-fluid nozzle.

When processed through these lines, the product is exposed to high fluid dynamic shear and interfaces that can threaten protein stability (Jameel and Hershenshon, 2010; Thomas and Geer, 2011); careful control of the process is therefore needed as the product is generally intended for parenteral administration.

The shear stress exerted in each operating unit of these two processes tightly depends on some geometric parameters and processing conditions, e.g., flowrate and equipment size. However, to provide an idea of the order of magnitude of shear stress and expected exposure time, **Table 2.1** summarises some relevant values referred to the various unit operations gleaned from the literature (Bee et al., 2009; Maa and Prestrelski, 2000; Nema and Ludwig, 2010; Ogunyankin et al., 2019).

Table 2.1 Typical shear rate and relative exposure time for unit operations in pharmaceutical manufacturing lines.

Operation	Shear rate, s^{-1}	Exposure time	Reference
Mixing	Up to 200	Minutes to hours	(Ogunyankin et al., 2019)
Pumping	Up to 2,000	Milliseconds to seconds	(Nema and Ludwig, 2010)
Filtration	$1,000 - 10,000$	Few seconds	(Bee et al., 2009)
Filling	Up to 20,000	Milliseconds	(Bee et al., 2009)
Atomization	$10,000 - 100,000$	Milliseconds to seconds	(Maa and Prestrelski, 2000)

To account for the combined effect of shear rate and exposure time, some authors introduced a new variable, known as 'total shear' (Ogunyankin et al., 2019) or 'shear history',

SH, (Bekard et al., 2011a; Jaspe and Hagen, 2006), although the general notion is expressed as:

$$SH = \gamma t_{exp}$$

(2.3)

where t_{exp} is the time of exposure which makes SH dimensionless.

Several sensors were developed to experimentally evaluate the shear stress at the solid-liquid interface for the various unit operations (Schmirler et al., 2013). Direct sensors, such as floating-element devices, and indirect sensors, such as thermal or optical sensors, are the most popular (Naughton and Sheplak, 2002). Direct devices measure the wall shear stress's integrated force on a flush-mounted floating element, which may be connected to a displacement transducer. On the other hand, the floating element sensor has several drawbacks. It can cause measurement errors associated with sensor misalignment; moreover, it is sensitive to pressure gradients, vibration, acceleration, and thermal expansion effects (Winter, 1979). Furthermore, thermal sensors work on temperature transduction to voltage. They are designed to achieve fast response time and high sensitivity; however, obtaining a unique calibration between wall shear stress and heat transfer is hard, and measurement errors can occur because of the temperature drift. Optical sensors, finally, rely on the Doppler shift of light scattered by particles. Due to challenges in geometric design, their application is restricted.

An alternative to the direct and indirect measuring of the shear stress is represented by Computational Fluid Dynamics (CFD) modelling (Katritsis et al., 2007). This approach offers an inexpensive way to perform a qualitative fluid dynamics prediction that would be extremely difficult to achieve using experimental techniques. Indeed, CFD is experiencing considerable development in the biotechnological field, and applications are reported for upstream and downstream processing (Sharma et al., 2011). CFD provides full-field data and data at multiple locations, which are not achievable by probes, which instead provide point values (Pordal et al., 2002). This feature supports process monitoring and improvement. In addition, CFD is shown to be effective in enabling the identification of a design space (A. S. Rathore et al., 2012), which refers to the combination of materials and operating conditions which assures quality for pharmaceuticals (U.S. Department of Health and Human Services Food and Drug Administration, 2009).

Furthermore, the complex nature of protein-based therapeutics poses unique challenges in the industrial field, which include the definition of appropriate scaling parameters to scale up the process from the laboratory unit. Similarly, scaling up from the Research & Development stage to the pilot stage must be carefully controlled to avoid batch failures (Al-Chi et al., 2013). An ideal scale-down (and -up) approach would mimic conditions at a commercial (or laboratory) scale and accurately predict and characterise its performance (Levin, 2001; Moino et al., 2023; Moscariello, 2016). In this light, potential scale-down methods to mimic shear stresses encountered in industrial unit operations will also be presented.

Hereafter, papers relevant to the effect of shear stress in common operations along a pharmaceutical manufacturing line will be presented, along with CFD details and relevant results.

Mixing

Mixing is a crucial step in drug production and occurs at various stages of the manufacturing process (Das et al., 2022). First, it is used to achieve homogeneous solutions of the drug substance and its excipients during the formulation stage (Crowley, 1999). In addition, mixing is crucial in ensuring the homogeneity of the drug product before the filling process (Das et al., 2022).

Mixing is generally conducted in a stirred tank (Piedmonte et al., 2018). Selecting the most appropriate impeller is crucial for maximising the process performance and can result in different shear stresses (Mirro and Voll, 2009). To provide an example, axial flow impellers are generally employed for shear-sensitive products due to milder shear conditions. On the other hand, magnetically driven bottom-mounted mixers may result in product aggregation when there is contact between the impeller and the drive unit (Brückl et al., 2016a); in the latter mixer configuration, cavitation and shear seem potential triggers of aggregation phenomena for monoclonal antibodies (mAb) (Gikanga et al., 2015). Furthermore, single use configurations are beginning to make inroads because of their reduced risk of contamination and increased flexibility (de Boulard and Kienle, 2022). Several single use mixing systems are commercially available, generally categorized as mechanically and hydraulically driven systems (Eibl and Eibl, 2011). In particular, the availability of several types of single use systems offers solutions with significantly low shear rates, thus making them suitable for shear-sensitive products (Junne and Neubauer, 2018).

Similarly, the choice of process parameters is critical. Typically, the mixing process requires high turbulence to ensure perfect mixing of the components. However, this can be harmful to shear-sensitive products, especially if high shear stresses are maintained for an extended time (Mcconville and Kessler, 2019). Several relationships have been developed to predict the shear stress expected around the impeller under different process conditions (Campesi et al., 2009; Metzner et al., 1961). Sánchez et al. (Sánchez Pérez et al., 2006) demonstrated that the average shear rate is a function of the rotational speed (N) only, under both laminar and turbulent conditions:

$$\bar{\gamma}_{lam} = k_{lam}N_{lam}$$

(2.4)

$$\bar{\gamma}_{turb} = k_{turb}N_{turb}^{3/2}$$

(2.5)

where k is a proportional constant.

Nonetheless, as shown in **Table 2.1**, biotherapeutics are subjected to a modest shear rate during mixing procedures, which usually lasts minutes to hours (Nesta et al., 2017; Ogunyankin et al., 2019). In a recent study, Chaubard et al. (Chaubard et al., 2010) focused on four mixing configurations; they applied Particle Image Velocimetry (PIV) technique to identify the shear stress distributions in the impeller area. Ultimately, they identified two configurations that appeared to show a good trade-off between acceptable mixing time and low shear stress.

It must be noted that, in addition to shear stress, biotherapeutics are exposed to solid surfaces during the mixing process, on which proteins could adsorb. As mentioned in Section 2.1, shear stress alone does not seem to cause protein aggregation (Thite et al., 2023); rather, its synergistic combination with interfacial stress represents the triggering phenomenon (Kopp et al., 2023; Nesta et al., 2017; Tavakoli-Keshe et al., 2014). In particular, Lin et al. found that shear stresses and interfacial stresses during mixing exposed aggregation-prone regions in the protein and resulted in protein aggregates (Lin et al., 2016).

Controlling shear stress during scale-up operations can become a complex undertaking (Babnik et al., 2020). Smaller versions of the commercial-scale tank are routinely used for scale-down process evaluations (Li et al., 2021), but it may be challenging to accurately scale up fill volume, impeller, and tank geometry. It is worth mentioning the work carried out by Sieck et al. (Sieck et al., 2013); they developed a scale-down model of hydrodynamic stress conditions similar to those of a production scale bioreactor and tested a mAb's robustness to such hydrodynamic conditions. The throughput of specific mAb dropped at high levels of hydrodynamic stress; this decrease was considerably greater when mimicking the recurrent transit of cells through the impeller area. Another valuable alternative is represented by CFD, which allows the investigation of different process scenarios for a given mixing tank at varying parameters (Mishra et al., 2021; A. S. Rathore et al., 2012). For reference, **Figure 2.4** displays the velocity trend in the impeller plane at different pump speeds. The velocity gradients generate shear stress, which results to be higher at higher pump speeds.
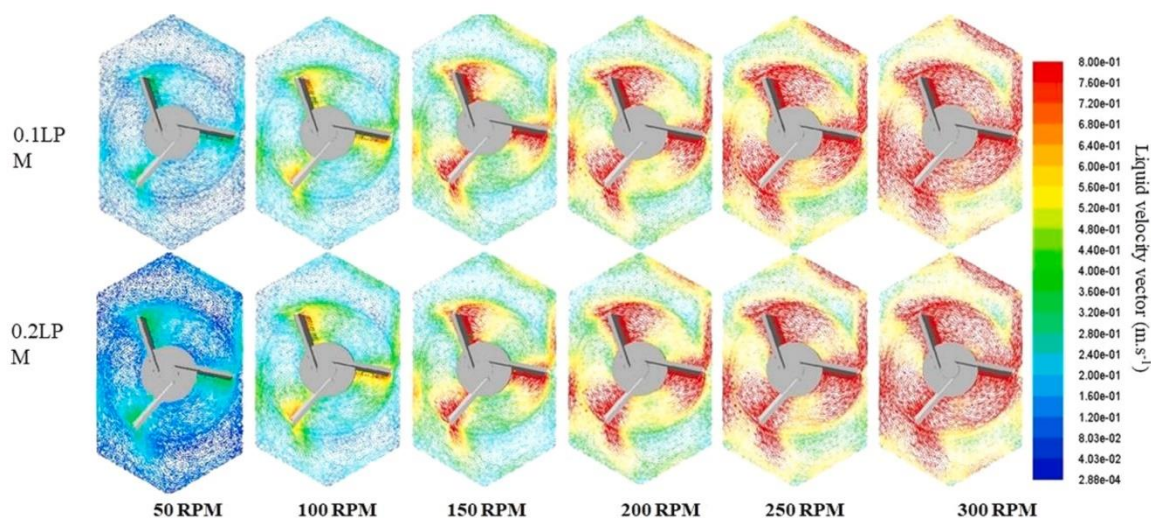
Figure 2.4 Velocity plots in the impeller plane for different agitation rates at different aeration rates (0.1 and 0.2 LPM). Reprinted with permission from (Mishra et al., 2021).

In addition to enabling the evaluation of the shear stress distribution within a typical mixing unit, they permit the identification of design space to assure quality.

Pumping

Shear stresses in pumping systems are widely documented, ultimately through CFD simulations (Song et al., 2003). They result from many factors, which include velocity, energy, pump efficiency, and tubing diameter. The pumping step is widely believed to impact product stability, which is why pump compatibility is chosen based on stability studies (Allmendinger et al., 2015). In this light, pumps can be classified as high-shear or low-shear pumps, and their selection is linked to product sensitivity.

Positive-displacement pumps and time-over-pressure fillers are two pumping systems used to handle biopharmaceuticals. Among the first category, the most used are piston pumps, rotary piston pumps, rolling-diaphragm (Karassik et al., 2001), and peristaltic pump fillers (Jameel and Hershenshon, 2010). Particularly, piston pumps and rolling-diaphragm fillers reduce the product's exposure to shear stress. Rolling-diaphragm pumps ensure the lack of seals or packing and show a low risk of particle formation (Nayak et al., 2011). On the other hand, peristaltic pumps exhibit more flexibility than piston pumps (Jørgensen and Lambert, 2008) and provide a gentle pumping action (Kovarcik, 2016), thus minimizing the stress on the product. However, they exhibit a lower accuracy (Saller et al., 2015), especially when handling highly viscous products. In the time-pressure system, the product, exiting from a pressurized manifold, passes through flow orifices which help regulating the flowrate (Peterson et al., 2007). The opening time of the shut-off valves and the manifold pressure are the main parameters controlling the pumping step.

Various authors have investigated how shear stress might affect protein degradation in the pumping stage; once again, its ubiquitous role cannot be assessed easily, as other drivers for product degradation can occur simultaneously, including interfacial stress, foaming, physical grinding, and cavitation (Nayak et al., 2011). Physical grinding refers to the trapping of product between moving parts of the pump, while cavitation refers to the violent creation and implosion of microbubbles (Bee et al., 2009). Each filling system has pros and cons regarding the impact on protein stability based on pump size, filling volume, filling rates, and needle specifications (Das et al., 2022).

Tyagi et al. (Tyagi et al., 2009) tested several piston pumps during filling and found that they resulted in variations in the amount of stainless-steel nanoparticles which further served as nuclei for protein particle formation. In a further attempt (Roffi et al., 2021), the effects of filling pump type, pump speed, and protein concentration on particle formation were investigated by performing experiments at the laboratory scale and then scaling up at the industrial unit. According to the authors, SVP formation was not proportional to the exerted shear rate in rotary piston pumps. A stainless-steel rotary piston pump was then used on mAb to test its effect on SVP (Kalonia et al., 2018). It was found that product concentration and interface material were more likely responsible for the formation of SVP rather than shear rate or passage number. Furthermore, Duerkop et al. (Duerkop et al., 2018b) demonstrated that the impact of isolated shear conditions on Human Serum Albumin integrity was low, and aggregation occurred as a result of the cavitation. According to Wu & Randolph (Wu and Randolph, 2020), instead, cavitation within the pump, if present, plays a minor role in generating aggregates because the protein adsorption initiates the aggregation in the pump chamber. Industrially relevant levels of shear rates seem, in fact, to be insufficient to cause protein denaturation in bulk solutions (Sediq et al., 2016). In a recent paper (Dreckmann et al., 2020a), the effect of three different types of pumps (rotary piston, radial peristaltic and linear peristaltic pump), was investigated, and particle formation was detected. CFD was used to explore the fluid dynamics within these configurations and the resulting shear stresses are reported in **Figure 2.5**.
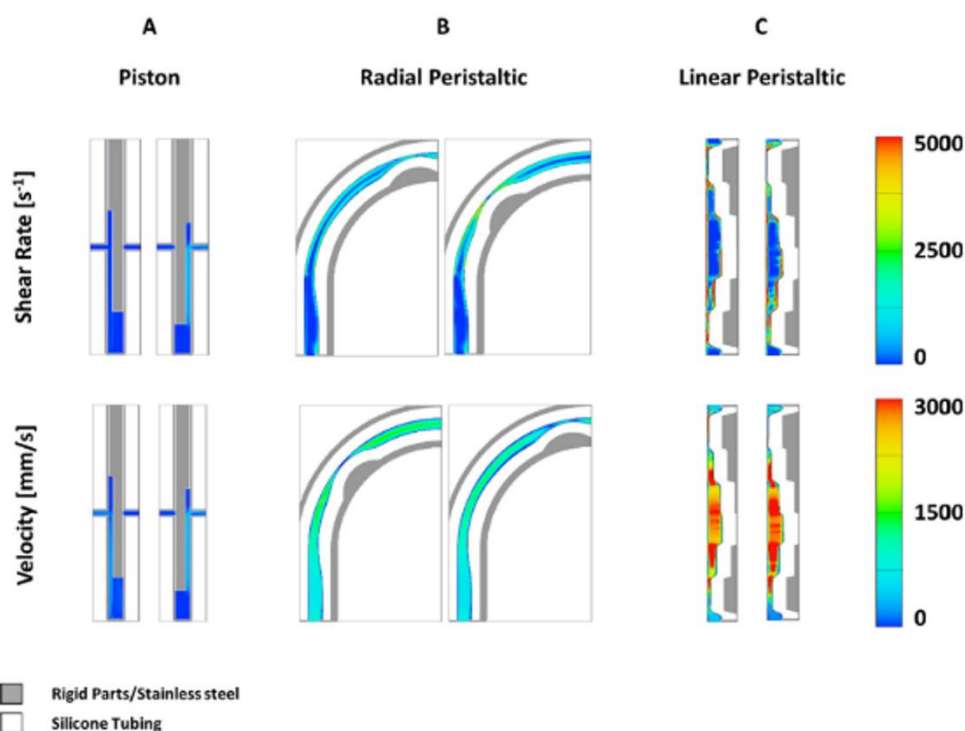
Figure 2.5 CFD analysis for piston pump (A), radial peristaltic pump (B) and linear peristaltic pump (C). Reprinted with permission from (Dreckmann et al., 2020).

In particular, the rotary piston pump resulted in the most notable protein aggregation even though the peristaltic pump operated at higher shear rates; according to the authors, this was because rotary piston pumps created a recirculation zone which further enhanced protein degradation due to repetitive exposure of the product to solid surfaces. This result confirmed the tendency for rotary piston pumps to damage biopharmaceuticals, as previously reported (Bausch, 2008; Cromwell et al., 2006). It must be noted that the cause for aggregation was not imputated to the shear stress per se, which rather enhanced the degradation. Similarly, the direct contact with the product in the piston pump might lead to product aggregation, as suggested in (Rajan et al., 2021).

In a time-pressure pumping system, the estimated shear rate is relatively small (2×10^2 s^{-1}) (Nema and Ludwig, 2010) and its impact on drug product stability is considered minimum (Das et al., 2022; Lim et al., 2015).

A last category of pumping systems suitable for handling pharmaceuticals is represented by syringe pumps, which are easy to use but involve a product volume dependent on the syringe volume. However, they are generally used in microfluidics experiments (Hallow et al., 2008) rather than industrial applications.

Regarding the scale-down approach, Li et al. (Li et al., 2019) suggest performing laboratory-scale experiments using a pump with representative pumping parameters and rates. In this way, any potential risk associated with the pumping process can be identified (Li et al., 2019).

Filtration

Protein-based therapeutics often undergo filtration to prevent microbial and/or particulate contamination (Pillai et al., 2016). Filtration is a pressure-driven process aiming to separate solids from a mixture by forcing it through a semi-permeable membrane (Jornitz, 2020); the upstream pressure forces the fluid through the membrane pores and out the permeate.

In the realm of bioprocessing steps, filtration is generally classified as depth filtration, dead-end filtration, and cross-flow filtration (Affandy, 2013). During in-depth filtration, undesired particles are trapped as they flow through the fibrous membrane of the filter. In dead-end filtration, all the flows are directed through the membrane with material building up on the filter surface (Nathan et al., 2008). Ultimately, the flow is addressed across the membrane surface in cross-flow filtration, also known as Tangential Flow Filtration (TFF). This last technique holds great industrial importance; its principle is based on pumping the feed in a tangential direction to the membrane to avoid build-up and clogging of the membrane pores. Both flat sheets and hollow fibres membranes were reported in the literature, but the second one involves lower shear forces. It must be noted that high shear can result in better cleaning and improved flux but it is suggested to avoid it in bioprocessing (Bekard et al., 2011a). Moreover, this technique is increasingly used for the concentration, separation, or purification of biological material in the laboratory as well as industrial scale units (Baruah et al., 2005; Elias and Joshi, 1998). It benefits from running under mild operative conditions, i.e., low temperatures and pressures, and high throughputs, which are convenient for processing shear-sensitive products (Hussain, 2019). Ultrafiltration (UF) and microfiltration (MF) are two of the most widely used TFF processes. UF is designed to retain macromolecules (Elias and Joshi, 1998) and is industrially used to produce vaccines, plasma, and serum (Ligon, 2020). On the other hand, MF is designed to retain particulates (Fernandez-Cerezo et al., 2019) in the 0.25 to 10 μm size range (Nathan et al., 2008) and finds successful applications in the biotechnological industry.

Sterile filtration in filling operations is commonly performed using dead-end filtration through a membrane with a small filtration rating; this allows complete retainment of up to 10^7 colony-forming units/cm^2 of filter area (Jornitz and Meltzer, 2008). Following the United States Food and Drug Administration and the USP guidelines, sterilising filters should be product compatible (Kong, 2006) and made of non-fibre releasing materials with a nominal rating of 0.2 μm and 0.22 μm respectively (Meltzer and Jornitz, 2003; Ramstorp, 2003). These filter membranes are often made of Polyvinylidene Fluoride or Polyethersulfone, whereas the housing is composed of a polymer, such as polycarbonate or polypropylene (Meyer and Coless, 2012). The choice of the proper filter is driven by some performance criteria, such as the total throughput, flowrate and yield loss associated with the filtration step (Priebe et al., 2003).

Pleated membrane configurations are generally used in pharmaceutical manufacturing as they allow a large membrane area to be packed into an element to increase filtration performance (Brown et al., 2009; Dippel et al., 2021). Capsule (Dixit, 2008) and cartridge filter

(Kumar et al., 2015) types belong to this class. Disc configurations are also available but are generally used for filterability trials (Dixit, 2008; Giglia and Yavorsky, 2007).

Shear stress in the filtration unit generates by forcing the formulation through narrow channels, like the filter's pores. As a result, shear stress – and wall shear stress – is not constant but a function of the radial position across the membrane; moreover, it depends on geometric parameters such as the filter structure, i.e., the pore size. These high levels of shear stress are often generated at the interface of the filter membrane and the product; protein aggregation could therefore arise as a result of the interfacial stress (Li et al., 2019).

Determining the actual shear stress experienced by the formulation when it flows through a filtration unit is very challenging. In one of the earliest studies (Maa and Hsu, 1998), it was assumed that the pore could be approximated to a straight cylinder with a diameter equal to the pore size, i.e. 0.22 μm, and thus the average shear rate was calculated using **Equation 2.6**:

$$\bar{\gamma} = \frac{8Q}{3\pi r^3}$$

(2.6)

where Q is the volumetric flowrate and r the distance from the centre of the pore.

Later, shear rates of $4 \times 10^4 - 4.8 \times 10^5$ s[-1] were estimated for antibody solutions filtered through 0.2 μm sterilising membranes (Nema and Ludwig, 2010). Furthermore, as the drug product concentration increases, the product viscosity increases, which results in higher pressures and, thus, higher shear stress exerted on the product (Krause et al., 2018). Combined effect of shear and hydrophobic interface was instead thought to be responsible for protein aggregation in the study conducted by (Aimar and Bacchin, 2010); in particular, shear forces seemed to accelerate degradation. In a recent study, Zhan et al. (Zhan et al., 2020), found values of shear rates of $2 \times 10^3 - 1 \times 10^4$ s[-1] in a TFF configuration for human embryonic kidney cells; the highest shear rates could cause cellular stress resulting in apoptosis. Further experiments were conducted on the UF/diafiltration unit operation by Callahan et al. (Callahan et al., 2014); the goal was to identify the dominant factor in protein particle formation among shear stress, impurities, interfacial interactions, or some combinations of those elements. It was demonstrated that the interfacial adsorption-desorption mechanism of the protein during the filtration operation was the principal cause of particle formation.

On the other hand, a few authors used CFD simulations to model and explore the filtration unit. Two different approaches can be adopted, named macro-scale and micro-scale approaches. The membrane is considered a porous medium in the macro-scale framework (Dippel et al., 2021; Velali et al., 2020). Several techniques were employed to reconstruct the pleat geometry in (Velali et al., 2020), as shown in **Figure 2.6;** this allowed the investigation of the impact of the plastic cage on the flow resistance.
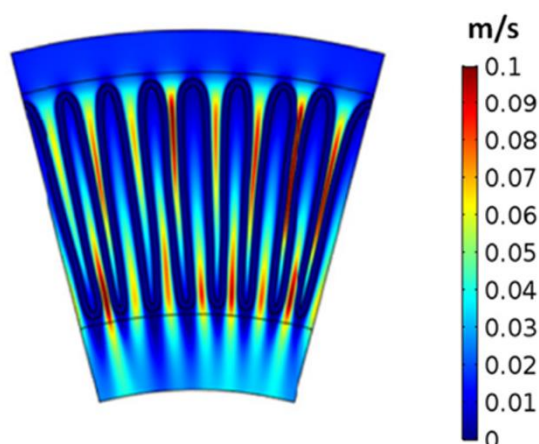
Figure 2.6 Simulated velocity profiles in a 2D cross section for a pressure drop of 0.5 bar. Figure taken from (Velali et al., 2020) with modifications.

Nonetheless, such a macro-scale framework does not allow for monitoring local properties (i.e., shear stress arising from the flow through the pores). Therefore, a micro-scale approach is needed where the pore network is modelled. One of the most significant barriers to implementing this approach is modelling such a small yet complex structure. A few works were reported (Affandy, 2013) but further research should be conducted to shed more light on the shear stress resulting from the sterile filtration unit.

Different phenomena, such as product adsorption to the membrane, can occur besides exposure to shear stress (Bódalo et al., 2004). Furthermore, filters can shed particles or cause leachable to get into the product (Werner and Winter, 2015); this represents a major concern as foreign particles may remain in the final product, thus impacting product quality and resulting in immunogenicity reactions (Pillai et al., 2016).

In addition, scale-down of filtration to bench scale poses unique challenges (Fernandez-Cerezo et al., 2019). An ideal scale-down approach should maintain flow path length and similar wall and entrance effect to help mimic the hydrodynamic shear characteristics. In parallel, pumping and piping flow effects should remain unchanged. Notable approaches were made by Fernandez-Cerezo et al. (Fernandez-Cerezo et al., 2019) and Hussain (Hussain, 2019); their goal was to develop an ultra-scale-down model in order to accurately predict the performance of large-scale TFF.

Filling

The filling is the final step in the overall drug manufacturing process. The drug is transferred from a filling needle to the container, usually a vial or a syringe for administration. Specifically, the product passes rapidly through the filling needle and other small-diameter filling parts (Carpenter et al., 2009). The filling needles are usually much smaller than the tubing that goes into them (Joyce and Witchey-Lakshmanan, 2013). Filling speed is often very high to decrease the overall process time (Peterson et al., 2007). Several authors have investigated the injection

forces of filling needles with various fluids. As general guidelines, the higher the product viscosity, the greater the forces involved (Allmendinger et al., 2014; Krayukhina et al., 2020).

Proteins are simultaneously exposed to interfacial (by contact with the solid needle surface) and shear stresses during filling. Because of interfacial stresses, the material used during the filling step can greatly affect product stability (Rathore and Rajan, 2008). Filling is made possible by the use of a dosage pumping system, the details and implications of which were given before. The filling technology must be chosen based on compatibility with the product and the various process parameters, which include filling rates, pump size and volume, and needle size and configuration (Jameel and Hershenshon, 2010).

The maximum shear stress experienced by a model product through a needle can be determined using the well-known analytical equations for laminar and turbulent flow(Moino et al., 2023). Filling an antibody solution into vials through a 5 mm needle would expose the product to a shear lower than 10^3 s^{-1} (Nema and Ludwig, 2010); if 20-gauge needles of 10 cm are used, instead, a shear rate of 2×10^4 s^{-1} would be exerted on the protein for about 50 ms given a flowrate of 0.5 mL s^{-1} (Bee et al., 2009). Although the experimental maximum shear and exposure time were far more than the calculated ones, no relevant aggregation was detected in their work. Later on, Nesta et al. (Nesta et al., 2017) simulated the passage of mAb through a 27-gauge, syringe-guided needle, and once again, no aggregation phenomena were encountered. Nevertheless, their calculations show that with the reduction of the needle diameter, the filling needle shear rate increases, but so does also the shear stress. Furthermore, for non-Newtonian solutions, shear rates in the range of $3 \times 10^4 - 1.6 \times 10^5$ s^{-1} for injection rates between 0.5 mL and 2.0 mL/10 s were calculated for 0.21 mm diameter needles (Allmendinger et al., 2014).

As far as the scale-down strategy, combined with the dosing system previously reported, the filling needle size should be chosen to represent the manufacturing scale (Li et al., 2019).

2.2.2 Potential impact of interfacial and shear stress combination on the finished product

Shear stress was initially believed to impact the catalytic activity of protein therapeutics (Elias and Joshi, 1998). Downstream the proposed literature analysis, however, it seems that the primary source of damage occurring in most bioprocessing steps is the synergistic presence of shear stress and interfacial stress; if proteins still maintain their tertiary structure even under extreme shear rate conditions (10^5 s^{-1}) (Jaspe and Hagen, 2006), it is rather its combination with interfacial stress the potential cause for product instability (Kopp et al., 2023). Indeed, shear stress can promote product turnover close to interfaces which accelerates aggregation (Aimar and Bacchin, 2010; Thite et al., 2023).

Product stability throughout the entire processing of protein-based therapeutics must be ensured (Rathore and Rajan, 2008). The International Council of Harmonization's Q5C

document (ICH, 1996) on the quality of biotechnological products claims that: "The products are susceptible to environmental factors such as temperature changes, oxidation, light, ionic content, and shear. To ensure maintenance of biologic activity and to avoid degradation, stringent conditions for their storage are usually necessary". A proper characterisation of the product stability is necessary to avoid the stresses encountered in fill-finish operations, resulting in aggregation and visible particles in the final product. Aggregation is indeed undesirable as it may have side effects on humans or can lead to drug instability issues (Brange and Havelund, 1983; James et al., 1981; Lehr et al., 2002; Zweifach, 1955). Moreover, it could cause a decrease in drug potency due to a lower dose in solution or induction of immunogenicity (Ratanji et al., 2014; Rosenberg, 2006; Schellekens, 2005). Consequences range from patient discomfort to permanent damage and potential death (Hoots, 2006; Reipert et al., 2007). Little is known about which aggregate species trigger the immune system; however, the immune system is thought to more easily recognise aggregates than the native parent protein (Den Engelsman et al., 2011). Thus, the product can be unacceptable if there is even a small amount of aggregates (Carpenter et al., 1999). Products must be tested according to the USP and EP procedures for subvisible ("Particulate contamination: Sub-visible particles," 2016; USP 788, 2006) and visible particles ("Particulate contamination: visible particles," 2008; USP 29-NF 24, 2006), to make sure that the product is suitable for administration to patients.

Extensive research and experiments on the physical stability of the product must therefore be conducted to choose the optimal formulation and dosage form that minimises immunogenicity (Hermeling et al., 2004).

Different strategies can be adopted to mitigate the impact of stressing conditions on the product. The precise choice depends on multiple factors, including the product's specificity and operating conditions. However, some general guidelines can be drawn for each unit step.

In the case of mixing, for instance, the impeller and the placement must be chosen with care, and low-shear mixers must be preferred (Chaubard et al., 2010; Converti et al., 1996). It may also be possible to inhibit agitation–induced aggregation by carefully choosing excipients (Serno et al., 2010).

In the case of shear-sensitive products, it might be necessary to optimise pumping (and filling) parameters to minimise the impact on the product, including using a lower pumping rate or a larger nozzle size (Jameel and Hershenshon, 2010). If the challenge is severe, the pump must be chosen to limit both the resultant shear stress and the exposure time to that shear (Dreckmann et al., 2020a), thus preferring low-shear pumps (Jameel and Hershenshon, 2010).

The concomitant effects of exposure to solid-liquid or air-liquid interfaces, as well as shear, can compromise product quality (Li et al., 2021). Given the complex interplay of interfacial and stress-induced denaturation, it is challenging to draw some general guidelines. Nonetheless, single-pass filtration should be preferred as it significantly reduces the overall exposure of the protein to interfaces as well as the shear stress within the pump and filter.

Furthermore, in the industrial realm, experiments can be carried out to investigate product stability under different process scenarios and thus ease the translation to manufacturing; in this light, identifying appropriate scale-down (and scale-up) methods is paramount. To transfer the filling process from the manufacturing to the laboratory unit, the pump, filling speed, and tubing size should be characterised so that they result in shear rates comparable to those encountered at the manufacturing scale (Jameel and Hershenshon, 2010).

In addition, it is crucial highlighting the importance of performing experiments at the laboratory level using lab chips because, as suggested by (Ashton et al., 2009), the shear-sensitivity of protein-based therapeutics might be product-dependent.

2.3 Lab chips for shear stress investigation

Considerable efforts have been made to develop potential devices to study the effect of shear stress on specific products. They differ based on the type of device and the technique used to characterise the product upon stressing. It is worth noting that they are not intended to mimic manufacturing unit operations, i.e., scale-down devices, but were designed to generate defined shear stresses and assess their impact of the product stability.

Chapter 2 The literature describing shear-induced degradation experiments on proteins goes back to the early 1970s. Forced degradation studies are crucial in developing protein-based therapeutics (Hawe et al., 2012). The devices hereafter presented differ in the product chosen for the analysis and in the properties studied to quantify the damage; moreover, the type or duration of protein stressing varies significantly among the various experiments. The devices are generally classified into capillary and rotational, and their working principle is shown in **Figure 2.7**.
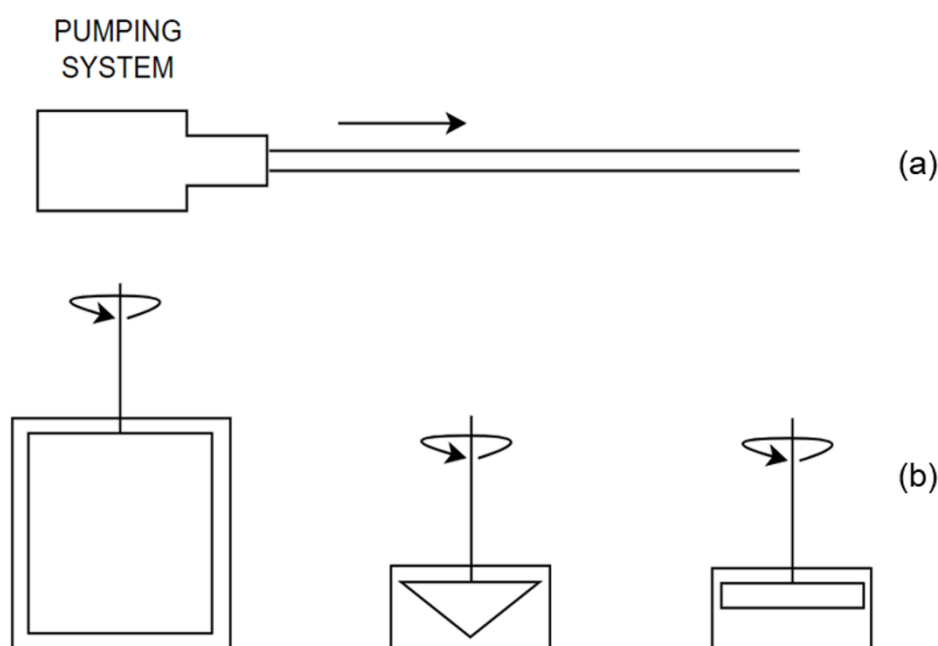
Figure 2.7 Traditional scheme for (a) capillary devices and (b) rotational devices (concentric
cylinder, cone-and-plate and parallel plate device).

If performing experiments with simple interfacial stresses is relatively easy, exploring the effect of pure shear is not straightforward. Indeed, in practice, it is not possible to isolate shear stress from other stress phenomena. This is precisely the reason for the confusion generated by old work that imputated the cause of product damage to shear, without considering the synergistic effect of shear and interfacial stresses. Nonetheless, devices that have been developed more recently attempted to minimise other forms of stress, which include solid-liquid and air-liquid interfaces (Thomas and Geer, 2011). According to Hudson et al. (Hudson et al., 2015), the ideal shear device should involve a small product volume, allow a large dynamic range of shear stresses to be investigated and limit the air-liquid interface.

Given these premises, capillary and rotational devices are further discussed in the following sections.

2.3.1 Capillary devices

The product is generally forced through a conduit of known dimension in capillary devices by applying a pressure difference between its inlet and outlet. The generated flow is of the Poiseuille type, with a parabolic velocity profile reaching the maximum value at the centerline ("Viscosity and shear stresses," n.d.; White, 2006); therefore, the shear is maximum at the wall boundaries and reduces gradually towards the conduit centre. Even though the shear stress is not constant, it is common practice to refer to an average shear stress.

In the analysed designs, the driving force for the motion of the fluid is either provided by a finger pump (Charm and Wong, 1970a), a piston (Murphy et al., 2020), a syringe (Dobson et

al., 2017), or a high-pressure liquid pump (Ogunyankin et al., 2019). In general, they allow the application of high shear rates (up to 2.5×10^5 s^{-1}) over short residence times. If needed, recirculation of the formulation can be used to increase the product exposure to shear stresses; nonetheless, this leads to an increased risk of interfacial denaturation at the solid-liquid interface. A critical advantage of using the capillary device in place of the rotational one lies in the lower product consumption.

One of the first documented attempts at stressing products in capillary devices was made by Charm & Wong (Charm and Wong, 1970a); the activity of catalase flowing through a Teflon capillary tube was tested as a function of the applied shear stress and the relative exposure time. Loss in activity was found at a relatively low shear rate, i.e., 67 s^{-1}, and long exposure time, i.e., 90 min, showing a strong correlation between shear history and protein damage. Later on, a further capillary device was developed (Thomas and Dunnill, 1979). A piston forced catalase solutions through the capillary device built from stainless-steel capillary tubes. The authors found no significant activity loss at shear rates up to 10^6 s^{-1}. These conflicting results raised the question of whether the enzymes in the earlier study were denaturating through an interaction with an air-liquid interface or solid surfaces, rather than as a consequence of shear. In this light, Jaspe & Hagen (Jaspe and Hagen, 2006) investigated the stability of cytochrome when flowing through a narrow capillary (d = 0.15 mm), exploiting fluorescence spectroscopy to detect any degree of unfolding. They found no evidence that even high shear rates alone could destabilize the folded protein. A further device called PSA (Protein Shear stress Application) was designed and patented by Heinzelmann et al. (Heinzelmann et al., 2008); the goal was to subject molecules in solution to shear stress and determine by analytical processes the changes in the stability characteristics. Tests were carried out at constant shear and over different residence times; it was found that as the shear stress increased, aggregated particles and turbidity increased considerably. In another work, a capillary rheometer was exploited to apply high shear rates for short periods; solutions of mAb were driven through the capillary using a piston. Dynamic Light Scattering (DLS) was used to analyse the sheared samples, but no aggregation was detected for shear rates up to 2.5×10^5 s^{-1} (Bee et al., 2009). Hudson et al. (Hudson et al., 2015) developed a miniaturised capillary rheometer to assess the fluid viscosity; it could utilise a small amount of product, i.e., a few microliters of sample. Ultraviolet-visible (UV-vis) spectrophotometer was employed to determine the concentration of the product (mAb).

Another remarkable investigation was conducted by (Nesta et al., 2017) on mAb stressed by a syringe pump up to 3×10^5 s^{-1}; the work aimed at assessing whether surface interaction, shear stress, a combination of those, or other events, i.e., cavitation, were causative for protein aggregation. No visible aggregates were detected showing that a more likely driver for product degradation was the exposure to the solid surface rather than the high shear rate. Dobson et al. (Dobson et al., 2017) developed a low-volume flow device able to deconvolute the effects of shearing (resulting from the flow within a capillary) and extensional flow (resulting from a rapid constriction). Two syringes drove the fluid motion to avoid exerting high shear stress on the product. They concluded that extensional flow could trigger the aggregation of Bovine

Serum Albumin (BSA). This, together with previously published articles (Simon et al., 2011), suggests that the ability of shear and extensional flow to induce aggregation is protein-dependent. Another valuable work was carried out by (Ogunyankin et al., 2019), who developed two small-scale tools to isolate interfacial and shear stresses. In particular, the interfacial stress was generated by the contact with uniform bubbles which passed through the solution for finite periods. On the other hand, shear stress was created using a small-scale high-pressure pump connected to fine stainless-steel tubing. The quality attributes assessed after applying the stress focused on detecting physical aggregation by High-Performance Liquid Chromatography (HPLC). Recently, Murphy et al. (Murphy et al., 2020) developed a novel capillary device to stress the product and then, analyse its microstructure through small-angle neutron scattering (SANS). Tests on mAb at 25 mg/L showed that nano-structural changes were expected at a shear rate higher than 1×10^4 s^{-1}.

A summary of the most relevant experiments involving capillary devices is reported in **Table 2.2**, where essential details of the tests are reported for clarity.

Table 2.2 Main details for relevant protein degradation studies using capillary devices.

Product	Shear rate	Focus	Technique	Reference
Catalase	67 s^{-1}	Activity	Rheogoniometer	(Charm and Wong, 1970a)
Catalase	4.6×10^4 s^{-1}	Unfolding	Absorbance	(Thomas and Dunnill, 1979)
Horse cytochrome c	1×10^5 s^{-1}	Unfolding	Fluorescence	(Jaspe and Hagen, 2006)
mAb	6.4×10^4 s^{-1}	Aggregation	PCS, turbidity	(Heinzelmann et al., 2008)
mAb	2.5×10^5 s^{-1}	Aggregation	DLS, TEM, SEC	(Bee et al., 2009)
mAb	$10 - 3 \times 10^3$ s^{-1}	Aggregation	UV-vis	(Hudson et al., 2015)
mAb	3×10^5 s^{-1}	Aggregation	SEC-MALS, DLS, MFI	(Nesta et al., 2017)
BSA	1×10^4 s^{-1}	Aggregation	DLS, NTA, TEM, FCS	(Dobson et al., 2017)
mAb	1×10^5 s^{-1}	Unfolding Aggregation	MFI, SE-HPLC, DSF, IA	(Ogunyankin et al., 2019)
mAb	1×10^4 s^{-1}	Aggregation	SANS	(Murphy et al., 2020)

2.3.2 Rotational devices

Rotational devices generally impart shear stress on the formulation across a narrow gap and are composed of a rotating and a stationary part (Bekard et al., 2011a). They include cone and plate, parallel plate, and concentric cylinder viscometers. The generated flow is of the Taylor - Couette type, with a linear velocity profile reaching the maximum in correspondence to the moving wall ("Viscosity and shear stresses," n.d.; White, 2006). Extensive research has been devoted to the analysis of the effect of shear on proteins stressed in rotational devices, since

their design minimises any end effects and, if the gap width is far lower than the radius of the inner cylinder, the shear rate can be considered constant for the entire solution (Bekard et al., 2011a). On the other hand, they require a relatively high product volume and the air-sample interface can be an issue (Hudson et al., 2015).

Various designs have been developed to generate shear flow, which include the Couette flow-cell, cone and plate, and concentric cylinder. In the Couette flow-cell and the concentric cylinder layout, the average shear rate can be calculated as follows:

$$\bar{\gamma} = \frac{4\omega \left(\frac{R_i}{R_o}\right)^2 \ln\left(\frac{R_i}{R_o}\right)}{\left(1 - \left(\frac{R_i}{R_o}\right)^2\right)^2}$$

(2.7)

where ω is the angular velocity of the rotating inner tubing, R_i and R_o are the inner and outer cylinder radii, respectively (Edwards et al., 2010). In the cone and plate design, instead, the average shear rate depends on the cone angle θ:

$$\bar{\gamma} = \frac{\omega}{\sin(\theta)}$$

(2.8)

One of the first attempts at shear-induced degradation in rotational devices dates back to the 1970s. Charm & Wong adopted a cone-and-plate device and stressed fibrinogen up to 290 s^{-1} (Charm and Wong, 1970b). They found that shearing could be the major responsible for fibrinogen degradation in the circulation. Rennet and catalase were the subject of further research conducted by Charm & Lai (Charm and Lai, 1971); they were stressed up to 91.5 s^{-1} in a cone-and-plate device, and activity loss was detected in a rheogoniometer.

Peterson et al. stressed (up to 8.2×10^3 s^{-1}) some glycoproteins in a cone-and-plate device; the product was characterised in terms of particle count and size, and particle formation was detected (Peterson et al., 1987). Ikeda et al. (Ikeda et al., 1991) exposed platelets to shear stress up to 6.7×10^3 s^{-1} using a cone-and-plate viscometer, and aggregation phenomena were monitored through an aggregometer. Works on rotational devices continue with Maa & Hsu (Maa and Hsu, 1996) who designed a novel concentric-cylinder device and stressed deoxyribonuclease and growth hormone at 1.5×10^3 rpm; various techniques were adopted, which included sodium dodecyl sulfate-polyacrylamide gel electrophoresis (SDS-PAGE) to determine protein fragmentation. They found no significant change in the sheared deoxyribonuclease, whilst unfolding and fragmentation occurred for the growth hormone.

A cone-and-plate design was adopted in a subsequent study (Van Der Veen et al., 2004); α-amylase was subjected to shear stress up to 120 s^{-1} and the relative activity was determined. It was found that hardly any inactivation could occur at low shear stress; however, increasing the shear stress resulted in significant irreversible inactivation of α-amylase.

Biddlecombe et al. (Biddlecombe et al., 2007) designed a rotating-disk shear device to assess the impact of high shear rates on protein stability at the solid-liquid interface; it provided an air-free environment and allowed sampling while the device was in operation. The authors stressed 1.0 and 0.5 mg/mL immunoglobulin in phosphate-buffered saline up to 3.4×10^4 s^{-1}; high shear rates resulted in significant protein aggregation and precipitation levels. A Couette flow cell was used by Ashton et al. to investigate the shear-induced unfolding of lysozyme in situ with Raman spectroscopy and PIV (Ashton et al., 2009); reversible conformational changes were monitored. Afterwards, Bee et al. (Bee et al., 2009) stressed monoclonal antibody formulations (100 mg/mL) up to 20,000 s^{-1} for up to 300 ms in a parallel-plate rheometer; SEC analysis was adopted to characterise aggregate formation. It was found that shear exposure alone during bioprocessing should not cause aggregation; air-bubble entrainment, adsorption to solid surfaces, pump cavitation stresses are rather believed to be the primary causes. In another thorough study (Bekard and Dunstan, 2009), a Couette cell was exploited to study the effect of shear on insulin in situ and in real-time; using Tyr fluorescence and circular dichroism (CD), it was found that aggregates could be expected at relatively low shear rates, i.e., 200 s^{-1}. In addition, the authors proved that the size of insulin aggregates decreased with an increasing shear rate.

In a further study on a Couette cell (Bekard et al., 2011b), poly-L-lysine (PLL) was stressed at various shear rates for 1 h and in-line CD analysis was conducted to probe unfolding; it was found that the α-helical-PLL structure unfolds in simple shear flow and the extent of unfolding depends on monomer size, shear rate, and duration of shear application. A few years later, Tavakoli-Keshe et al. (Tavakoli-Keshe et al., 2014) developed a shear device capable of generating a high-shear environment and tested it on modified mAb; the device was composed of a round device chamber containing a stainless-steel disk and the air-liquid interface was eliminated and a well-controlled shear and interface environment was created. The relative stability of mAb was measured, and molecular modelling techniques were employed to investigate the proteins' secondary and tertiary structures upon stressing. It resulted that the proposed technique could be used as an orthogonal method for antibody screening. Brückl et al. (Brückl et al., 2016b) developed a Couette device and stressed ghGh and IgG1 in free solution, where the interfacial effects are negligible; shear stress was unlikely to unfold the proteins up to shear rates of at least 1×10^4 s^{-1}.

In another Couette device experiment, instead, aggregates were detected for human insulin even at low shear rates (McBride et al., 2015). In the work of Nesta et al. (Nesta et al., 2017), already mentioned in the previous section, a parallel-plate rheometer was used to stress mAb up to 20,000 s^{-1} for relatively high residence time. They detected an increase in particles throughout all size ranges induced by the applied shear stress that, according to the authors,

exacerbated the degradation pathway of the surface-stressed formulation. Another remarkable device is the one developed by (Morimoto et al., 2017); the researchers established a novel Rheo-NMR (Nuclear Magnetic Resonance) approach that allowed to observe protein dynamics during shear and trace atomic-level structural change. Shear rates of $510 - 950$ s^{-1} applied to ubiquitin resulted in amyloid fibrils formation. Similarly, in a further work from the same research group (Iwakawa et al., 2021), shear rates of $290 - 540$ s^{-1} were applied to SOD1 (amyotrophic lateral sclerosis-related) protein in the Rheo-NMR and aggregation through amyloid formation was monitored.

The details of these shear-induced rotational devices degradation tests are summarized in **Table 2.3**.

Table 2.3 Main details for relevant protein degradation studies using rotational devices.

Product	Shear rate / Rotational velocity	Focus	Technique	Reference
Fibrinogen	$290\ s^{-1}$	Degradation	Thrombin addition	(Charm and Wong, 1970b)
Catalase	$91.5\ s^{-1}$	Activity	Rheogoniometer	(Charm and Lai, 1971)
Rennet	$91.5\ s^{-1}$	Activity	Rheogoniometer	(Charm and Lai, 1971)
Glycoprotein	$8.2 \times 10^3\ s^{-1}$	Unfolding	Particle size, count	(Peterson et al., 1987)
Platelet	$6.7 \times 10^3\ s^{-1}$	Aggregation	Aggregometer	(Ikeda et al., 1991)
Deoxyribonuclease	$1.5 \times 10^3\ rpm$	Aggregation	SDS-PAGE	(Maa and Hsu, 1996)
Growth hormone	$1.5 \times 10^3\ rpm$	Aggregation	SDS-PAGE	(Maa and Hsu, 1996)
α-Amylase	$120\ s^{-1}$	Activity	Modified DNS	(Van Der Veen et al., 2004)
Immunoglobulin	$3.4 \times 10^4\ s^{-1}$	Aggregation	UV-vis	(Biddlecombe et al., 2007)
Lysozyme	$7 \times 10^2\ s^{-1}$	Aggregation	Raman	(Ashton et al., 2009)
mAb	$2 \times 10^4\ s^{-1}$	Aggregation	SEC	(Bee et al., 2009)
Insulin	$600\ s^{-1}$	Unfolding	Fluorescence, CD	(Bekard and Dunstan, 2009)
Polylysine	$715\ s^{-1}$	Unfolding	CD	(Bekard and Dunstan, 2009)
Modified mAb	$9 \times 10^3\ rpm$	Aggregation	SE-HPLC, DSC	(Tavakoli-Keshe et al., 2014)
rhGH, IgG1	$1 \times 10^4\ s^{-1}$	Unfolding	CD, LD, Fluorescence	(Brückl et al., 2016b)
Human insulin	$150\ s^{-1}$	Aggregation	turbidity, absorbance, AFM, CD	(McBride et al., 2015)
mAb	$2 \times 10^4\ s^{-1}$	Aggregation	SEC-MALS, DLS, MFI	(Nesta et al., 2017)
Ubiquitin	$510 - 950\ s^{-1}$	Aggregation	NMR	(Morimoto et al., 2017)
SOD1	$290 - 540\ s^{-1}$	Aggregation	NMR	(Iwakawa et al., 2021)

2.4 Conclusions

Interest in the impact of shear stress on protein stability began many decades ago, and still more and more papers are being published to try to discern its effects. Downstream of this literature review, the authors believe that early attempts misinterpreted the results and incorrectly attributed the main cause of protein degradation to mere shear stress. In fact, the primary role appears to be played by interfacial stress, possibly amplified by shear stress that promotes product turnover in areas in contact with the interface. Finding a shear stress threshold for protein denaturation is far from simple: it depends not only on the product, but also on the method of determination (and thus the extent of the interface). Protein-based therapeutic products are often processed through production lines that may include mixing, pumping, filtration, filling, and atomization. Because shear stresses commonly originate during these steps, a more critical understanding of its impact on product stability has been gained through screening the available literature. The importance of laboratory chips for investigating shear stresses should be emphasized, as they allow the product to be stressed to a defined extent and study the consequences on the product behavior. Again, a broad spectrum of results was observed for different devices, showing not only that shear susceptibility depends on the product, but more importantly that the presence of interfacial stress is the main cause of protein degradation. In a future perspective, MD could be adopted to gain further insights into product behavior in shear flow. In addition, we foster technological advancements in designing lab chips for controlled shear stress experiments under conditions that limit the influence of interfaces so as to deconvolute shear stress-induced and interfacial denaturation of proteins.

Chapter 3

Theoretical background

The analyses presented in this work are run using the finite volume method-based open-source code OpenFOAM. Different versions of the software were used throughout the project to exploit unique solvers or tools of specific releases. For the sake of clarity, the details are therefore given in the individual chapters.

Before delving into the theoretical background, it is appropriate to make a nomenclature clarification. Unlike standard notations which refers to shear stress as τ (Byron Bird et al., 2002), we will be referring to the shear stress as σ across the manuscript. This is because in the present cases τ indicates the residence time a product experiences a defined σ.

3.1 Governing equations

The continuity equation and the Navier-Stokes equation express the conservation equations of mass and momentum, and are used to estimate the pressure and velocity fields. In the case of incompressible fluids, they read as follows:

$$\frac{\partial u_i}{\partial x_i} = 0$$

(3.1)

$$\frac{\partial u_i}{\partial t} + u_j \frac{\partial u_i}{\partial x_j} = -\frac{1}{\rho} \frac{\partial p}{\partial x_i} + \nu \frac{\partial^2 u_i}{\partial x_j^2}$$

(3.2)

where u_i is the ith component of the fluid velocity, p is the fluid pressure, and ρ and ν are its density and kinematic viscosity, respectively.

These equations hold true for all the analyzed geometries; particular attention should be given to the sterilizing filtration where the characteristic length of the pores of the membrane is rather small, i.e., in the order of hundreds of nm. In such a case, nonetheless, the continuum hypothesis still holds true (Liu and Li, 2011) and, therefore, the transport phenomena inside the pores are governed by **Equation 3.1** and **3.2**. For such filtration unit, simulation results are then interpreted based on macroscale continuum equations for fluid flows in porous media. The parameters of these spatially smoothed equations (e.g., porosity and permeability) are derived from averaging procedures performed on the microscopic governing equations of both the porous medium and fluid flow, as explained by Whitaker (Whitaker, 2013). Thus, **Equations 3.1** and **3.2** become:

$$\frac{\partial V_i}{\partial x_i} = 0$$

(3.3)

$$\frac{\partial V_i}{\partial t} + V_j \left(\varepsilon \frac{\partial V_i}{\partial x_j} \right) = -\frac{1}{\rho} \frac{\partial p}{\partial x_i} + g_i + \frac{\nu}{k} V_i$$

(3.4)

where V_i is the Darcy velocity in the porous medium, ε the medium porosity, and k the membrane permeability. Assuming the flow is stationary, the regime is laminar and the gravity effects are unimportant, some terms can be neglected; this leads to the well-known Darcy's Law written as a one-dimensional expression:

$$\frac{\Delta P}{L} = -\frac{\mu |V|}{k}$$

(3.5)

where $\Delta P/L$ is the pressure drop over the length of the porous medium and μ is the dynamic fluid viscosity.

3.2 Investigated conditions

Various conditions can be encountered in filling lines, i.e., laminar and turbulent conditions. In laminar flow, fluid layers move smoothly over one another in the direction of the flow (Byron Bird et al., 2002). On the other hand, under turbulent conditions, a random and chaotic state of motion develops in which pressure and velocity undergo significant fluctuations with time (Pope, 2000; Wilcox, 1994).

In the pharmaceutical realm, turbulent conditions are often desired as they promote mixing of the reactants and ensure higher throughput within the same time. Nonetheless, laminar conditions occur when the product is processed through the sterilizing filtration and the final filling needles. The fluid dynamic regime is based on the characteristic Re, which is defined as the ratio between inertial and viscous forces. In the case of a fluid flowing in a circular pipe with diameter d, Re is calculated as:

$$Re = \frac{\rho u d}{\mu}$$

(3.6)

where u is the fluid velocity, while ρ and μ are the fluid density and viscosity, respectively. More specifically, laminar flow occurs when Re is lower than 2100 while turbulent when it is greater than 4000. When dealing with turbulence, various modeling approaches can be used, named Reynolds Averaged Navier–Stokes (RANS), Large Eddy Simulation (LES), and Direct Numerical Simulation (DNS). The first approach resolves the mean flow, whereas the fluctuating components resulting from turbulence are modeled (Tu et al., 2018). LES and DNS

methods, on the other hand, are intrinsically more accurate, but entail a significant increase in the computational demand (van Hooff et al., 2017). The RANS approach was therefore adopted under the given conditions. Within this framework, the $\kappa - \omega$ Shear Stress Transport (SST) model was used to characterize the turbulence, being a two-equation model that successfully applies in a large variety of flows (Menter, 1994). It utilizes the traditional $\kappa - \omega$ model in the inner region of the boundary layer and switches to the $\kappa - \varepsilon$ model in free shear flows, thus resulting in improved capabilities (Versteeg and Malalasekera, 2007). The model involves the introduction of new transport equations, namely for turbulent kinetic energy (κ) and specific turbulent dissipation rate (ω). The latter is expressed as:

$$\omega = \frac{\varepsilon}{\kappa}$$

(3.7)

where ω is the turbulent dissipation rate. The transport equations for the turbulent properties are expressed as:

$$\frac{\partial \kappa}{\partial t} + \frac{\partial}{\partial x_i}(u_i \kappa) = P_\kappa - \beta^* \kappa \omega + \frac{\partial}{\partial x_i}\left[\left(\nu + \frac{\nu_T}{\sigma_\kappa}\right)\frac{\partial \kappa}{\partial x_i}\right]$$

(3.8)

$$\frac{\partial \omega}{\partial t} + \frac{\partial}{\partial x_i}(u_i \omega) = \alpha S^2 - \beta \omega^2 + \frac{\partial}{\partial x_i}\left[\left(\nu + \frac{\nu_T}{\sigma_\omega}\right)\frac{\partial \omega}{\partial x_i}\right] + 2(1 - F_1)\sigma_{\omega 2}\frac{1}{\omega}\frac{\partial \kappa}{\partial x_i}\frac{\partial \omega}{\partial x_i}$$

(3.9)

where F_1 is a blending function, ν_T is the turbulent kinematic viscosity, S is the invariant measure of the strain rate, and P_κ is a turbulent production term.

On the other hand, in the case of a fluid flowing through a porous media, the below equation holds:

$$Re = \frac{\rho u_{pore} D_{pore}}{\mu}$$

(3.10)

where u_{pore} is the pore-scale velocity and D_{pore} is the mean pore diameter of the membrane, defined as the diameter of a sphere having the same volume as the mean pore. As visible in **Figure 3.1**, three different regimes can occur based on Re (Xiao et al., 2017). In particular, the Forchheimer zone (b) for the flow nonlinearity is located between the Darcy zone (a) and the turbulent flow zone (c). The critical Re can be found from the transition between the Darcy ($Re < 5{\sim}10$), Forchheimer ($Re < 40{\sim}100$), and turbulent flow (Lee and Yang, 1997; Liu et al., 1994). More specifically, the Darcy zone is dominated by viscous effects while the Forchheimer zone by inertia effects.
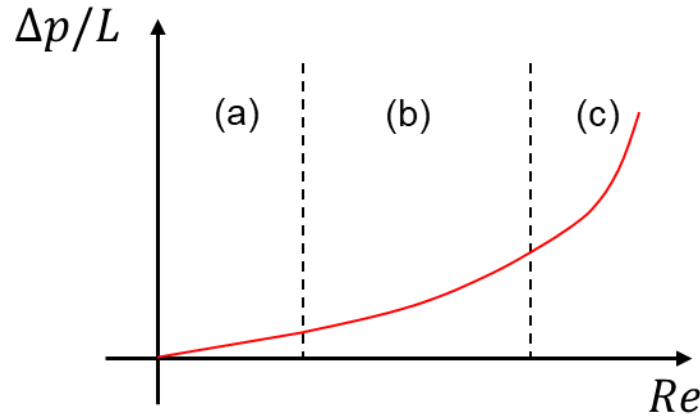
Figure 3.1 Flow states in a porous medium.

Nonetheless, given the examined operating conditions ($D_{pore} \cong 0.2 \cdot 10^{-7}$m, small u_{pore} given by $\frac{u}{\varepsilon}$, Darcy zone occurs and, therefore, a linear relationship between the pressure drop and Re, i.e., flowrate, is expected.

Given these premises, both fluid dynamic conditions were investigated. Hereafter, the relevant equations for each category for fluid flowing in a circular pipe are reported. In the porous medium, the pore can in fact be considered as a cylinder with diameter D_{pore} and, hence, the same equations can be employed for some preliminary estimations.

3.1.1 Laminar flow

The radial velocity profile is well-known in the literature and depends on the distance from the center (r):

$$u_{lam} = 2\bar{u}\left(1 - \frac{r^2}{R^2}\right)$$

(3.11)

where $\bar{u}$ is the average fluid velocity and R is the tubing radius.

The shear stress is also a function of the distance from the center and reached its maximum value at the tubing wall. The equation is as follows:

$$\sigma = Q\frac{4\mu}{\pi R^4}r$$

(3.12)

where Q is the volumetric flowrate.

3.1.2 Turbulent flow

Under turbulent condition the flow pattern is complex and time-dependent. The velocity is therefore decomposed into a steady mean value with a fluctuating component (Versteeg and Malalasekera, 2007). The mean radial velocity can be expressed as follows (Stigler, 2014):

$$u_{turb} = u_{max} \left(1 - \frac{r}{R}\right)^{1/n}$$

(3.13)

where n is a function on Re (Schlichting, 1979) and u_{max} is calculated as:

$$u_{max} = \bar{u} \frac{(n+1)(2n+1)}{2n^2}$$

(3.14)

Furthermore, the shear stress is the sum of two contributions, named viscous and turbulent shear stresses. The new turbulent term results from the Reynolds stresses but it is difficult to estimate (Kudela, n.d.). However, the total shear stress at the wall is still a function of the distance from the center and can be calculated as follows:

$$\sigma_{tot,wall} = \frac{1}{2}\rho\bar{u}^2 C_f$$

(3.15)

where C_f refers to the skin friction factor. This parameter can be calculated starting from the expression of the mean velocity profile for the logarithmic-law correlation, also called Prandtl's friction law (Pope, 2000). Such equation involves a non-linear relationship between C_f and Re, which is hence difficult to determine. Therefore, several approximations are available for defined Re ranges. Among those, the Blasius approximation was chosen (Trinh, 2010), being valid in the Re range of interest $(2.1 \cdot 10^3 - 10^5)$ (Byron Bird et al., 2002).

$$C_f = \frac{0.079}{Re^{1/4}}$$

(3.16)

3.3 Particle tracking techniques

In the present project, innovative strategies are introduced to track biological particles of fluid through their trajectories and detect their relevant fields. This made it possible to develop shear stress statistics which accounted for the actual shear stress history of each individual particles.

Therefore, the Stokes number (St) for these particles was initially estimated; this correlates the particles response time (τ_P) and the fluid time scale (τ_f), as follows:

$$St = \frac{\tau_P}{\tau_f}$$

(3.17)

The biological particles in the drug product have about the density of water (Fischer et al., 2009), and their size is smaller than 200 nm (Bachmann and Jennings, 2010). This results in St below the unity for all the operating conditions described. In such conditions, particles are expected to follow streamlines closely. Lagrangian Particle Tracking (LPT) is a powerful technique employed in Computational Fluid Dynamics (CFD) to simulate the behaviour of individual particles as they move through a fluid system. The interaction between the particles and the fluid is modelled, and different categories of coupling can be used (Elghobashi, 1994), as visible in **Figure 3.2**.
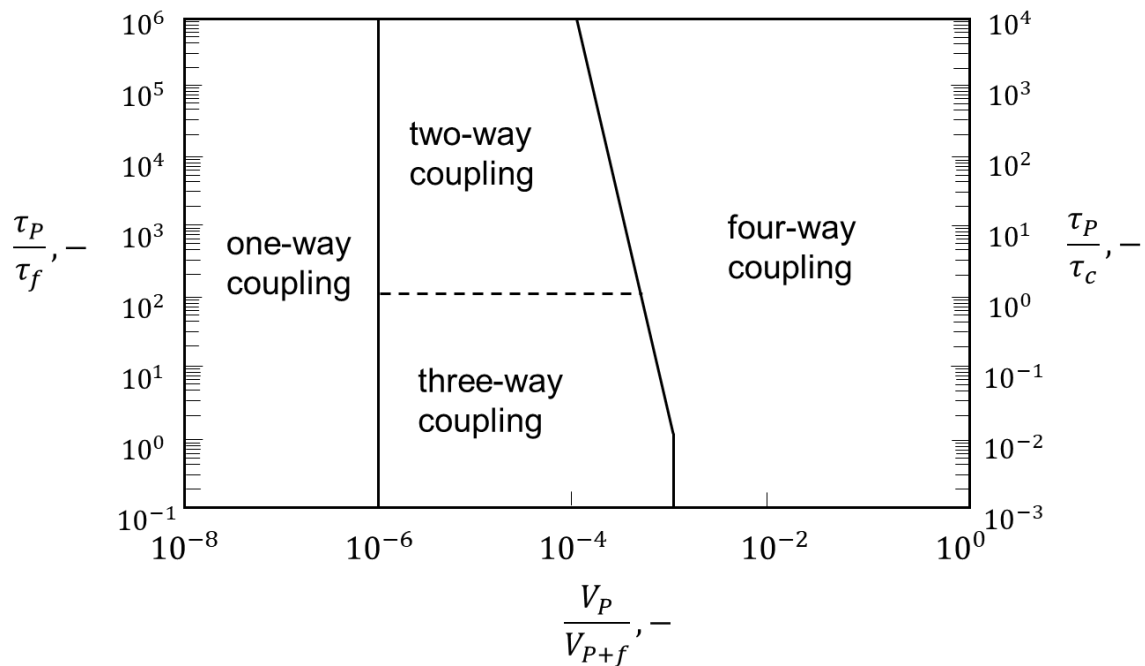
Figure 3.2 Map of regimes of interaction between particles and fluid.

where τ_c refers to the turnover time of large eddy, and V_P/V_{P+f} + is the volume of a single particle normalized by the volume occupied by particles and fluid.

In one-way coupling particles are assumed to have no effect in the fluid flow. On the other hand, particles' effect on the fluid flow is considered in the two-way coupling, as well the fluid's effect on the particles. The three-way coupling is an extension of the second-way coupling, as it accounts also for the effect of the influent of a particle's motion through the fluid on another particle. In addition to this, four-way coupling considers particle-particle collision. One-way coupling was chosen given the premises made earlier. One of the biggest

40

benefits of using LPT is that you learn more about the fluid dynamics behaviours of individual particles than you might from using traditional contour plots investigations.

In this light, a particular type of LPT was used to track massless tracers for some of the case studies investigated (tubing, fittings, and sterilizing filtration); this tracking was made possible by the use of the 'Stream tracer with custom source' algorithm available in ParaView. Here, no diffusive or dispersive are accounted for and allows the study of the time evolution of the position and fluid dynamics condition of these tracers as if they were particulate flow parcels. This algorithm works by taking a set of points in the data set, called 'seed points', and then integrating the streamlines starting at these points. Streamlines are curves that are instantaneously tangential to the vector field in the dataset and indicate the direction in which particles in the dataset would travel at that instant of time (Moreland, 2014). The integration was tuned by choosing the integration direction and the maximum streamline length (which was chosen high enough so as to follow the complete trajectories of the tracers through each geometry). The seed point locations were given as input to the integrator, and their release is fully described in **Chapter 4**, **5**, **6**, **7**.

Instead, LPT was used to investigate the shear history in the case of the pumping system. Given the more complex structure and design (dynamic mesh, transient simulation), conventional static tracers were unable to detect the actual behaviour of the parcels. Therefore, a one-way LPT was chosen to precisely follow parcels at each time step, generally called 'pathline' (Johnson and Hansen, 2005). This was done by using the function object 'icoUncoupledKinematicCloud' available in OpenFOAM.com 1806, and the details of the implementation are given in Appendix A1.

By definition, parcels refer to a collection of particles with the same physical properties; however, for the sake of clarity, they are simply referred to particles throughout the manuscript. Additional details on the set up of this LPT technique will be given in **Chapter 7**.

42

Chapter 4

The role of tubing

Parenteral drug products flow in smooth tubing in filling lines. The residence time is very high (from hours to days) which is why an accurate investigation of fluid dynamics became necessary. This chapter presents the workflow developed for modeling a water-like flow in smooth tubing and the resulting shear stress estimation for two case studies, in laminar and turbulent flow conditions, respectively. In addition, the field of scale-down approaches was deeply explored; new strategies for scaling down the industrial process were proposed and compared with traditional ones. Conclusively, discussions on the proposed workflows and scale-down strategies will be outlined*.

4.1 Methods

4.1.1 Numerical set up

Analysis of the shear stress distribution experienced by the product when flowing through standard filling operations is performed thanks to CFD simulations. The finite volume method-based open-source code OpenFOAM 9 (https://github.com/OpenFOAM/OpenFOAM-9 (accessed on 1 January 2022)) was used for the purpose. The simulations were carried out on an Intel(R) Xeon (R) Gold 5118 CPU at 2.30 GHz and 128 GB of RAM. The simulations' post-processing was conducted via Python 3.8 scripts and the ParaView application. An incompressible and Newtonian fluid was considered (Dreckmann et al., 2020a) and gravity was neglected. The numerical set up specific for each component of the line analyzed is given in the next sections.

The peristaltic pump is commonly used in bioprocessing lines to drive the fluid across the process. It works by alternating compression and relaxation of the tubing, drawing content in and moving product away from the pump, (Klespitz and Kovács, 2014) thus creating a pulsating flow. (Womersley, 1955) Since the time-averaged properties in pulsating flow are those of the steady flow under laminar and turbulent conditions, (Shemer et al., 1985) steady-state simulations were implemented rather than transient ones because of the more straightforward set up and lower computational cost needed.

---

* The work described in this chapter has been previously published in "Moino, C., Scutellà, B., Bellini, M., Bourlès, E., Boccardo, G., Pisano, R., 2023. Analysis of the shear stresses in a filling line of parenteral products: The role of tubing. *Processes*, 11, 833."

The mesh was designed via the OpenFOAM utility *blockMesh*. A structured O-grid topology was chosen for the layout and smooth tubing was considered. Moreover, a traditional scale-down approach (same Re among the scales) and worst-case scenario approach (same u) were tested numerically, named, respectively Approach 1 and Approach 2, aiming to study their effect on shear stress. For clarity, Approach 1 is a simple approach that leverages dimensional analysis. Scale disparities are resolved by matching Re. Since the product used for laboratory-scale experiments is the same as the commercial scale (and hence same ρ and μ) the only parameter to be changed is the fluid velocity. The commercial internal diameter was chosen equal to 9.53 mm while the laboratory tubing was smaller, i.e., 4.76 mm, in such a way as to decrease the product consumption. These dimensions were chosen because they are those generally used industrially for pharmaceutical processes. Regarding the velocity, 0.208 m s^{-1} and 1.145 m s^{-1} were chosen for laminar and turbulent simulations, respectively. The domains were discretized by structured grids comprised of hexahedral cells. Geometric grid expansions were used to achieve local refinement of the mesh near the boundaries, as shown in the cross-sectional tubing area of **Figure 4.1**.
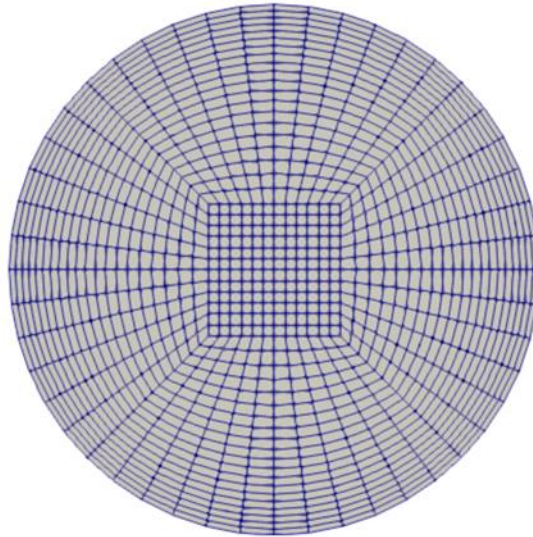

Figure 4.1 Typical cross-sectional mesh of the tubing

Within the framework of the $\kappa - \omega \, SST$ model, y^+ insensitive wall functions were adopted. y^+ is a non-dimensional scalar quantity used to define the distance from the wall as follows (Liu, 2016):

$$y^+ = \frac{y u^t}{\nu}$$

(4.1)

where y is the absolute distance from the wall, and u^t the friction velocity which, in turn, is derived from the wall shear stress. The boundary conditions for the turbulent properties at the wall patch were therefore chosen from those of the wall function treatment framework.

Defined boundary conditions were specified for the other variables; at the wall, a Dirichlet boundary condition, *i.e.,* no-slip condition, was imposed for the velocity while at the outlet a

Neumann boundary condition, *i.e.,* zero-gradient condition, was set. A uniform velocity was then imposed at the inlet of the tubing, since the dynamics would develop once in the fully developed region. Regarding pressure, a zero-gradient condition was chosen for the wall and the inlet of the geometry while a uniform value (equal to 0) was used for the tubing outlet; it needs to be reminded that having employed an incompressible solver, these are values of relative pressure.

A Semi-Implicit Method for Pressure Linked Equations algorithm was used through the implementation of the *simpleFoam* solver, applying under-relaxation factors equal to 0.9. A Geometric Agglomerated Algebraic Multigrid (GAMG) solver was implemented for pressure, while a smooth solver coupled with the Gauss-Seidel smoother was chosen for the other variables. Regarding the convergence criterion, the threshold values for the scaled residuals were set to 10^{-6} for pressure and velocity. Along with the convergence criterion, monitoring of values of interest was performed to ensure they reached an accurate and steady solution. To this end, the analytical equations previously reported in **Sections 3.1.1**, **3.1.2** were utilized for the comparison.

A grid independence analysis was conducted by increasing the cell number in order to find the optimal grid, resulting from a trade-off between computational cost and solution's accuracy. Such grid independence analysis was done by varying the number of cells in the blocks forming the O-grid topology and the number of cells in the z-direction. Results of the grid independence study for flow through a 9.53 mm diameter tubing in laminar and turbulent flows are shown in **Figure 4.2**, where the maximum shear stress was chosen as monitored parameter. For the sake of clarity, these values were validated by comparison to the analytical equations reported in **Sections 3.1.1** and **3.1.2**. Under laminar conditions, an observation can be drawn by comparing the meshes corresponding to approximately 3.3×10^4 and 1.1×10^5 cells (**Figure 4.2** (a)). Increasing the number of cells by an order of magnitude does not lead to a significant improvement in the accuracy of the maximum shear stress (i.e., 0.1%) and, therefore, the computationally less demanding mesh can be used for the analysis. Similar considerations can be drawn under turbulent conditions (**Figure 4.2** (b)).
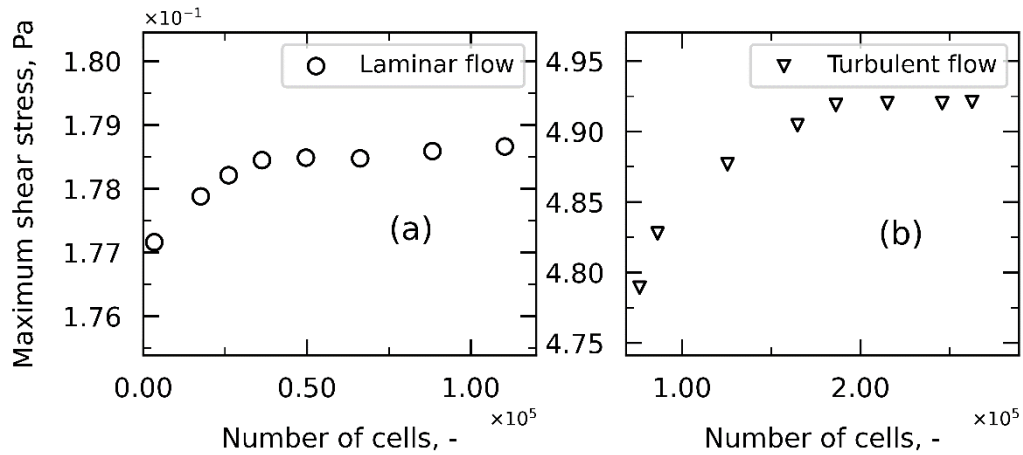
Figure 4.2 Grid independence analysis for the case of 9.53 mm diameter tubing under laminar (a) and turbulent (b) conditions.

Around $3.3 \cdot 10^4$ cells were used for the laminar simulations, and $1.8 \cdot 10^5$ for the turbulent simulations. Given the same fluid dynamic regime, the mesh resolution between the commercial and laboratory scales was preserved.

4.1.2 Shear stress distribution

As described in **Sections 3.1.1** and **3.1.2**, shear stress under both laminar and turbulent conditions varies linearly with the distance from the tubing center. This is shown in **Figure 4.3**, where the colored lines are representative of particle's trajectories uniformly released across the diameter in the tubing's fully developed region. This provides a neat visualization of the shear stress profile through the cross-sectional area.
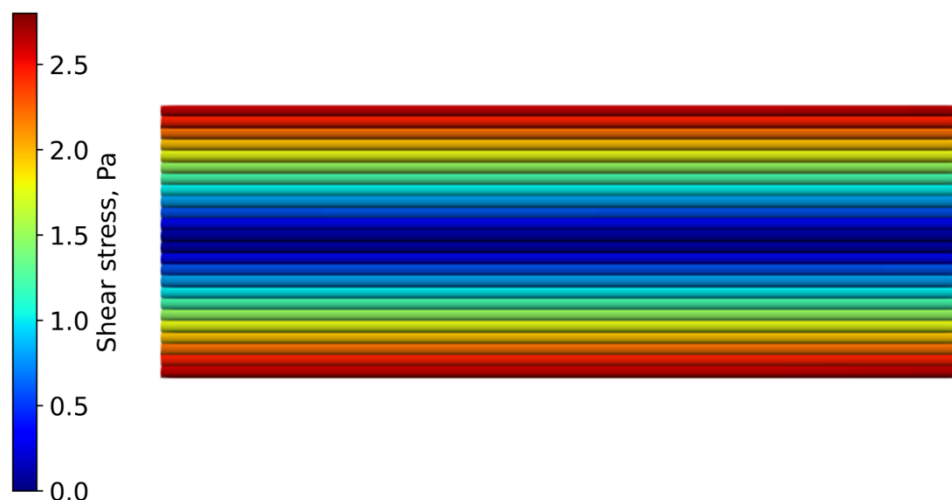
Figure 4.3 Shear stress characteristic of defined particles' trajectories in the cross-section of the tubing lengthwise. Follow the color scale from blue (low shear stress) to red (high shear stress).

In bioprocessing steps, it is a common practice to refer to the maximum shear stress to characterize the hydrodynamic force acting on the product (Bee et al., 2009). However, this phenomenon is experienced only by the fluid flowing close to the wall. In addition, the fluid residence time varies through the sectional area of the tubing and reaches the lowest values at the wall, where the shear stress is the maximum. These points reveal how the effective average shear stress on the product might be a function of the volumetric flowrate that it experiences. Not surprisingly, the volumetric flowrate varies along the radial coordinate of the tubing, reaching its maximum value at the tubing center.

$$\bar{\sigma} = \frac{1}{Q_{tot}} \sum_i \sigma_i Q_i$$

(4.2)

Therefore, **Equation 4.2** was developed, in which the average shear stress is obtained by summing the contributions of the local shear stress weighted on the relative volumetric flowrate. For the sake of clarity, the local properties are collected by considering each cell of a tubing slice in the fully developed region. To provide an example, **Figure 4.4** shows a typical plot for the shear stress distribution under laminar conditions; considering an arbitrary shear threshold that is 80% of the maximum value, i.e., $1.44 \cdot 10^{-1}$ Pa, **Figure 4.4** indicates that only a small percentage of the overall product, i.e., around 12%, can experience it. Sturges' rule was applied to calculate the optimum number of bins for all the histograms hereafter presented (Scott, 2009).
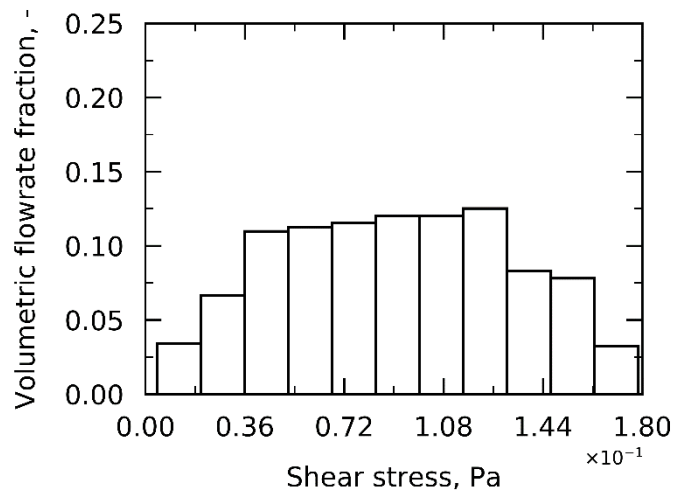

Figure 4.4 Shear stress distribution weighted on normalized volumetric flowrate under laminar conditions.

Similar considerations can be drawn for **Figure 4.5**, representative of turbulent conditions.
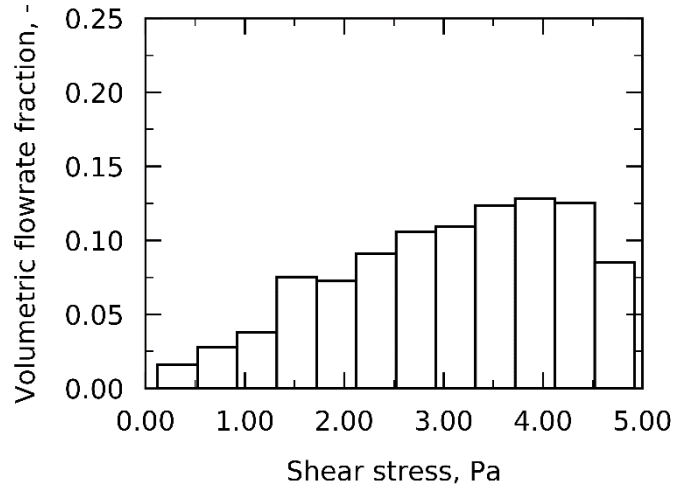
Figure 4.5 Shear stress distribution weighted on normalized volumetric flowrate under turbulent conditions.

4.1.3 Scale-down approaches

Approaches 1 and 2 were numerically tested to transition from commercial to laboratory size. In addition, a new method was proposed to scale down pipe tubing using the shear stress distribution as a scaling parameter and will be further referred as Approach 3. Both laminar and turbulent regimes were investigated and are presented in two separate sections.

Laminar regime

As the shear stress distribution is the desired scale-down parameter, through manipulation of **Equation 3.12**, the inlet velocity at the laboratory level results from that used on the commercial scale as follows:

$$\bar{u}_l = \bar{u}_c \left(\frac{R_l}{R_c} \right)$$

(4.3)

where the suffixes c and l stand for commercial and laboratory, respectively. The tubing length is calculated as to ensure the same shear stress history, i.e., same residence time:

$$\tau_l = \tau_c$$

(4.4)

$$\frac{L_l}{R_l} = \frac{L_c}{R_c}$$

(4.5)

48

Equation 4.3 presents a major benefit: while scaling to the laboratory unit, i.e., decreasing the tubing diameter, the fluid velocity is also diminished. This strategy preserves the fluid dynamics regime to be preserved among the plant scales.

Turbulent regime

The wall shear stress introduced in **Equation 3.15** was set as a scaling parameter.

$$\frac{\bar{u}_l^7}{R_l} = \frac{\bar{u}_c^7}{R_c}$$

(4.6)

By making the skin friction factor explicit, **Equation 4.6** shows the relation which enables the wall shear stress to be constant between commercial and laboratory units. It is worth pointing out that the skin friction factor was calculated using Blasius approximation, as presented in **Section 3.1.2**; therefore, **Equation 4.6** is applicable only within its validity range ($2.1 \cdot 10^3 - 10^5$). A more widely applicable equation could be obtained by exploiting Prandtl's equation (Byron Bird et al., 2002), where the skin friction factor is a non-linear function of the Re; however, its application is not trivial. Furthermore, when using **Equation 4.6**, care must be taken with the characteristic Re; when decreasing the tubing size at the laboratory level, the fluid velocity decreases, and so does Re. Hence, it is essential to check the Re number of the laboratory scale to avoid working under different fluid dynamics regimes; to avoid this concern, for example, a higher tubing diameter can be selected in the laboratory. In a similar fashion to laminar flow, the tubing length under turbulent conditions is chosen to preserve the shear history between the scale, and thus **Equation 4.4** is followed.

4.2 Results

Approaches 1 and 2 previously explained were numerically tested under laminar and turbulent conditions. Through CFD simulations, it was found that their application does not maintain the same distribution of shear stress between the scales. **Figure 4.6** presents the results of the application of Approach 1 under both laminar and turbulent conditions. At the laboratory level, where the diameter, and hence the radius, is half that of the commercial scale, the maximum shear stress is four times higher. Therefore, the laboratory unit would not be representative of the commercial line from the perspective of the shear stress exerted on the product.
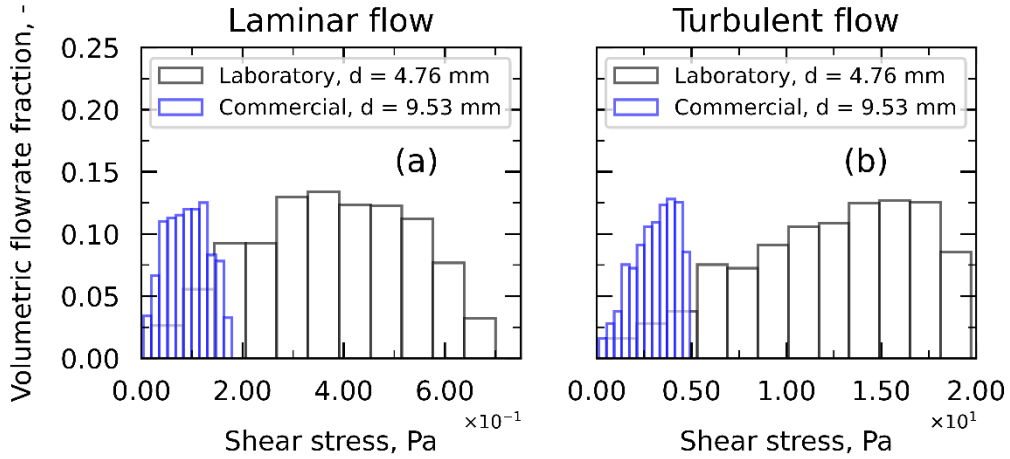
Figure 4.6 Shear stress distribution weighted on normalized volumetric flowrate for commercial (blue histogram) and laboratory (black histogram) unit following application of Approach 1 for laminar flow (a) and turbulent flow (b).

Similarly, the application of Approach 2 is shown in **Figure 4.7**. It results that under laminar conditions (**Figure 4.7** (a)), the maximum shear stress at the laboratory level would be overestimated by a factor of 2, being the ratio between the commercial and laboratory diameter. On the other hand, under turbulent conditions (**Figure 4.7** (b)), the difference between the shear stress distributions does not appear to be as pronounced; however, referring to **Equations 3.15** and **3.16**, this disagreement increases as the diameter chosen at the laboratory scale decreases.
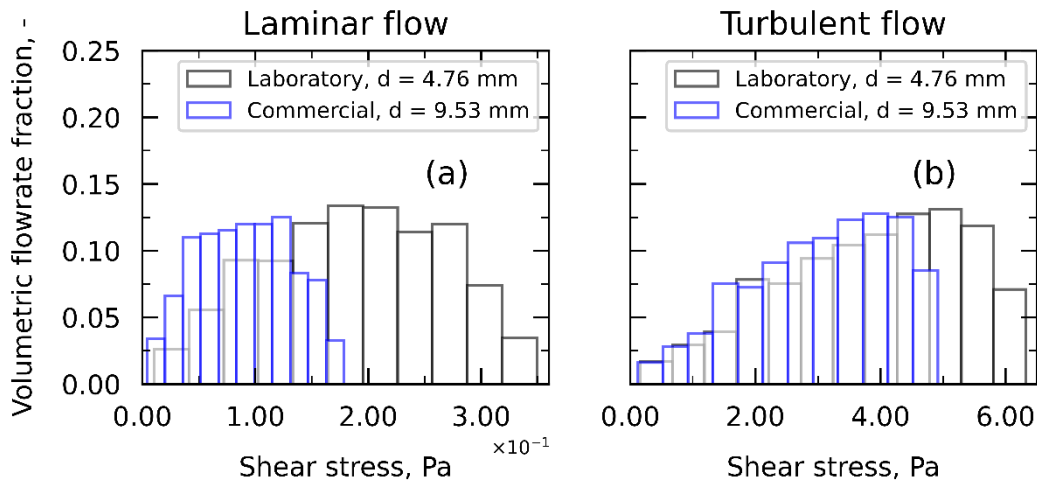

Figure 4.7 Shear stress distribution weighted on normalized volumetric flowrate for commercial (blue histogram) and laboratory (black histogram) unit following application of Approach 2 for laminar flow (a) and turbulent flow (b).

The application of Approach 3 (under laminar conditions) is shown in **Figure 4.8** (a) and (b); a good consistency is observed between the shear stress distributions in the two scales.
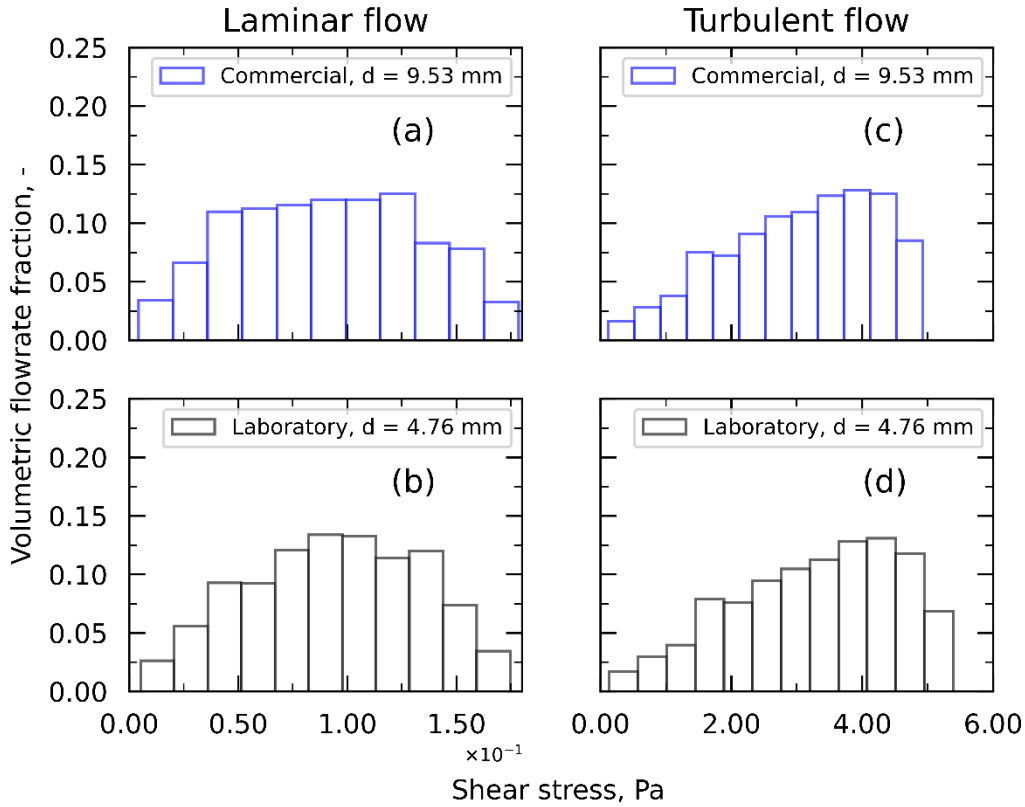
Figure 4.8 Shear stress distribution weighted on normalized volumetric flowrate following application of Approach 3 under laminar (a,b) and turbulent conditions (c,d) for the commercial (a,c) and laboratory scales (b,d), respectively.

Furthermore, under turbulent conditions (**Figure 4.8** (c) and (d)), the maximum shear stress is aligned between the laboratory unit and the commercial process, and so is the shear stress distribution. The slight discrepancy between the two units could be due to the fact that the average velocity at the laboratory unit is assessed using Blasius approximation and not the original equation. This choice was made to derive an equation easy to be implemented. **Table 4.1** summarizes the results of the tested approaches between the commercial and laboratory scales in terms of the maximum shear stresses (σ_{max}, Pa) and the effective average shear stress ($\bar{\sigma}$, Pa) calculated according to **Equation 4.2** using the operating conditions provided in **Section 4.1.1**. Again, it can be observed that Approach 3 is the one that best ensures representativeness between commercial and laboratory units in terms of shear stress exposure.

Table 4.1 Comparison between the tested approaches under laminar and turbulent flow in terms of maximum shear stress (σ_{max}, Pa) and effective average shear stress ($\bar{\sigma}$, Pa) between commercial and laboratory scales.

	Approach 1		Approach 2		Approach 3	
	commercial	laboratory	commercial	laboratory	commercial	laboratory
laminar	$Re_l = Re_c$		$\bar{u}_l = \bar{u}_c$		$\dfrac{\bar{u}_l}{R_l} = \dfrac{\bar{u}_c}{R_c}$	
σ_{max}, Pa	0.18	0.70	0.18	0.35	0.18	0.17
$\bar{\sigma}$, Pa	0.09	0.37	0.09	0.19	0.09	0.09
turbulent	$Re_l = Re_c$		$\bar{u}_l = \bar{u}_c$		$\dfrac{\bar{u}_l^7}{R_l} = \dfrac{\bar{u}_c^7}{R_c}$	
σ_{max}, Pa	4.92	19.72	4.92	6.32	4.92	5.39
$\bar{\sigma}$, Pa	3.04	12.20	3.04	3.85	3.04	3.27

4.3 Conclusions

In the present work, CFD modeling was used to analyze the shear stress distribution experienced by a model product when flowing through a pipe under laminar and turbulent conditions. Numerical validation of the results was performed using the well-known analytical equations for laminar and turbulent flows. It was found that the average shear stress could be effectively calculated as a function of the volumetric flowrate that it experiences. Furthermore, a new scale-down strategy was proposed and compared with the most conventional approaches. While the traditional (Approach 1) and worst-case scenario (Approach 2) approaches were not able to ensure representativeness between commercial and laboratory scales in terms of shear stress distribution, the new approach (Approach 3) was successful. From the perspective of scale-down, maintaining the fluid dynamic regime between the commercial and laboratory scales is an essential prerequisite during the application of any scale-down approach. By applying the new scale-down method, this is ensured under laminar conditions; in turbulent flow, however, a decrease in tubing diameter can lead to a decrease in Re. Therefore, it is essential to carry out a careful control of the Re at the laboratory scale and, if necessary, choose a higher tubing diameter to remain in the turbulent regime.

This work introduces a novelty in the pharmaceutical field, where scale-down is never completed considering the process from the product's perspective. However, unlike other industrial processes, product quality control is critical; therefore, it is essential that the scale-down strategy preserves the same shear stress exposure as the commercial scale, which in the present work was considered to be that resulting from shear effects. The following steps of this study will/could involve (i) performing experimental tests to study the effect of such shear stress distribution on product stability, (ii) wider investigating the actual shear stress distribution in pulsating flow, typical of peristaltic pumps, and (iii) extending the analysis reported in this paper to all the other components commonly present in a filling line.

Chapter 5

The role of fittings

Fittings of various shapes are often used in filling lines to allow product sampling. More specifically, when sampling is necessary, the flow coming from one exit is stopped and directed to a sampling bag. This makes it possible to ease product sampling through the process flow, which are pivotal to verify product quality through every stage of the process. Fittings generally involve a change in direction to the main flow which exposes the product to high shear stresses, which is the reason for the deep exploration of the resulting fluid dynamics presented in this chapter. Actual trajectories of particles were gathered from streamlines and shear stress estimations could be performed*. Different flow conditions were investigated for two fittings configurations and comparisons with the tubing scenario were outlined.

5.1 Methods

Two-outlet fittings are generally used to allow product sampling. During normal operation, one of the two outlets is blocked, and the product can thus flow to subsequent equipment. When sampling is needed, however, the product flow is stopped and directed to a sampling bag through the previously blocked outlet. Two simplified geometries representing two possible different structure configurations of the sampling lines were considered. The analyzed geometries are shown in **Figure 5.1** (a), (b), and the implemented structures are shown in **Figure 5.1** (c), (d).

---

* The work described in this chapter has been previously published in "Moino, C., Scutellà, B., Bellini, M., Bourlès, E., Boccardo, G., Pisano, R., 2023. Analysis of the shear stresses in a filling line of parenteral products: The role of fittings. *Processes*, 11, 1797."
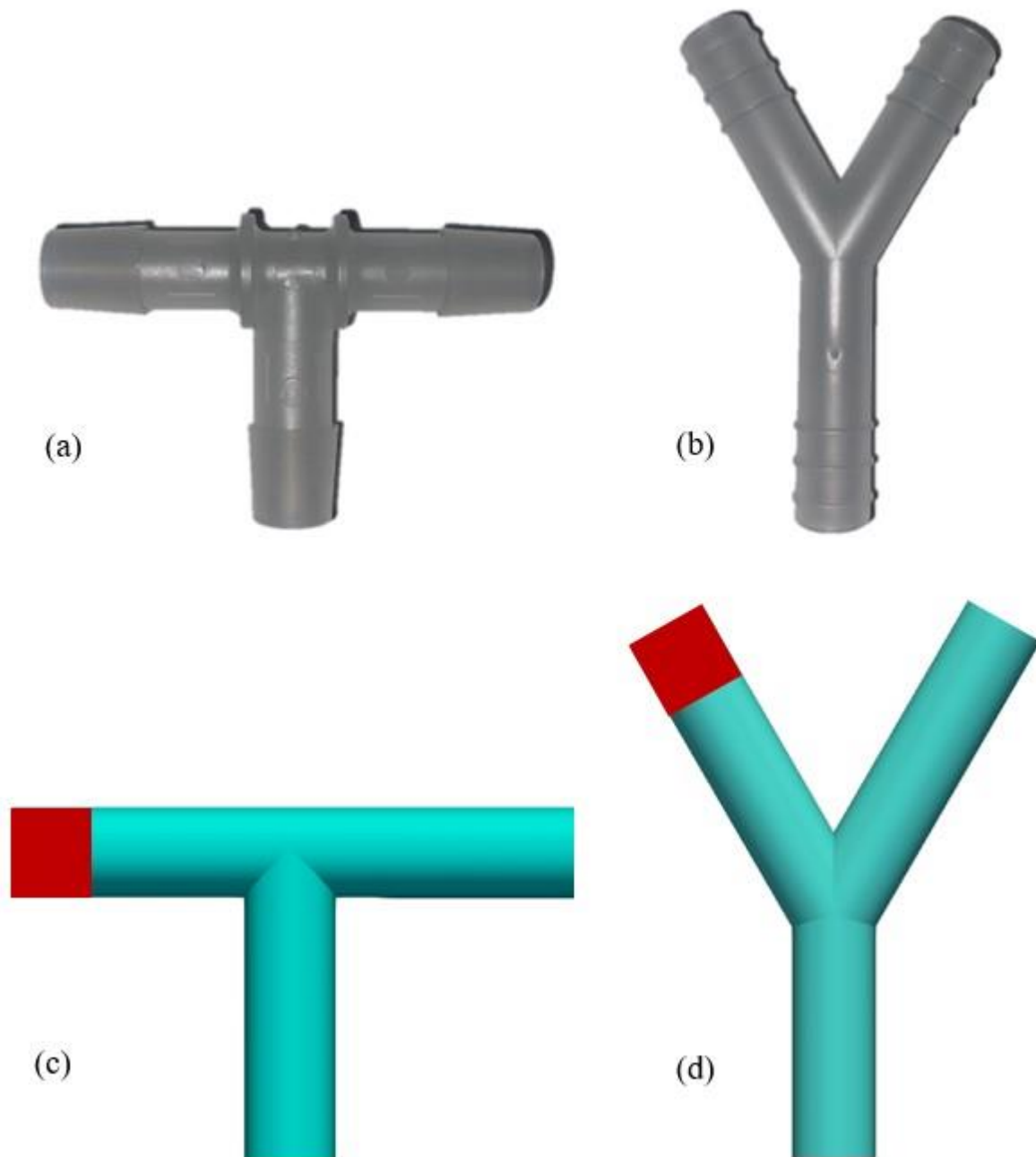
Figure 5.1 Fittings analyzed.

As for the tubing scenario, because of the easier set up and lower necessary computing cost, steady-state simulations were employed for both laminar and turbulent regimes. The meshing procedure made use of the *snappyHexMesh* utility from OpenFOAM; in the case of the more complex Y-fitting, under both fluid dynamic conditions, the design of the background mesh was conducted on the Ansys Fluent mesher (Ansys, Inc., Canonsburg, PA). The length of the arms on T- and Y-fittings with an internal diameter of 9.53 mm was chosen to ensure fully developed flow in both fluid dynamic regimes, and avoid having unphysical description in the system due to proximity of the system boundary conditions (Tu et al., 2018). Velocities of 0.042 and 0.500 m s^{-1} were arbitrarily chosen, among the ranges of possible flowrates for these systems, in order to explore both laminar and turbulent conditions, respectively (Byron

Bird et al., 2002). The domains were discretized by structured grids comprised of hexahedral, prism and polyhedral cells.

The aforementioned $\kappa - \omega \, SST$ turbulence model was implemented while using y^+ insensitive wall functions (implemented in the boundary conditions of the turbulent properties). The chosen turbulence model allows the y^+ insensitive wall treatment; in fact, it contains wall functions that are valid throughout the whole boundary layer. One of the main advantages of this model is that it is very flexible, since it is independent of the y^+ value and, therefore, precise resolution of the grid in the boundary layer is not needed.

Special attention should be paid to the boundary conditions. A uniform value of velocity was specified at the inlet boundary condition, while the no-slip and zero-gradient conditions were imposed at wall and outlet patches, respectively. Regarding pressure, a zero-gradient condition was selected for wall and inlet patches while a uniform value equal to 0 was chosen for the outlet. Beside these conventional boundary conditions for the main patches, the symmetry boundary condition was imposed to the patch related to the clamped exit. This was chosen to mirror the field pattern along such patch.

Using a Semi-Implicit Method for Pressure Linked Equations, the OpenFOAM solver simpleFoam was employed. The Geometric Agglomerated Algebraic Multigrid (GAMG) solver was chosen for pressure, while a smooth solver coupled with the Gauss-Seidel smoother was set for the other variables.

Numerical verification and validation were performed for each geometry and regime condition. This was done by playing on some parameters, including the number of background cells in the initial blockMesh, the number of refinement levels close to the wall and the number of cells between adjacent levels. In particular, a grid independence analysis was conducted, which confirmed that the solution remained invariant when the mesh was tightened. Finally, the outcome of the simulations was compared with the analytical equations presented in **Sections 3.1.1** and **3.1.2**. The steps are summarized in **Figure 5.2** (a) and (b), which show the numerical validation analysis for a T-fitting in laminar flow. The grid independence analysis, reported in **Figure 5.2** (a), was carried out monitoring the pressure drop across the fitting; on the other hand, **Figure 5.2** (b) plots the percent error between the numerical and analytical shear stress in the inlet branch of the fitting, where the fluid dynamic develops as in a straight tubing. It should be noted that this last analysis was not done on the entire fittings because no valid analytical equations were found with these geometries.
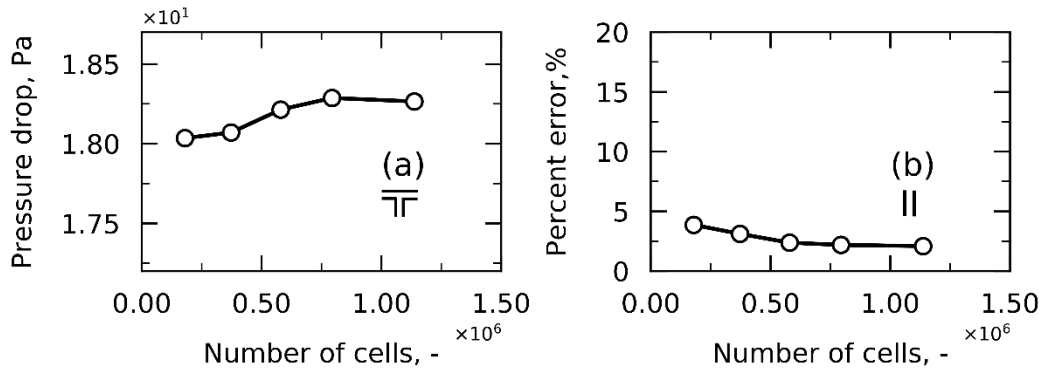
Figure 5.2 Numerical verification and validation analysis for T-fitting under laminar conditions: grid independence analysis (a), percent error between the numerical and the analytical shear stress in the inlet branch of the fitting (where the fluid dynamics develops as in a tubing) is monitored by varying the number of cells (b).

It can be observed from **Figure 5.2** (a) that the grids comprising more than 0.79×10^6 cells led to an almost invariant solution. Increasing the cell number up to the final considered grid led to a small improvement in the solution accuracy, which is not worth the much higher computational demand. A similar trend can be observed in **Figure 5.2** (b). A similar approach was taken for numerical verification and validation for the Y-fitting under laminar conditions (**Figure A2.1** in Appendix A2) and for both fittings under turbulent conditions (**Figure A2.2** and **Figure A2.3**). For the Y-fitting under laminar conditions, a mesh with 0.88×10^6 cells was chosen. Under turbulent conditions, meshes with about 2.9×10^6 and 1.2×10^6 cells were chosen for the T- and Y-fitting, respectively. Furthermore, the mesh quality and topological coherence of the mesh were analyzed using OpenFOAM utilities. This analysis ensured that the mesh adhered to grid quality standards in terms of non-orthogonality (below 75), skewness (below 20 for boundaries and below 4 for internal mesh), and aspect ratio. Some images of the chosen grid for the T-fitting under laminar conditions are displayed in **Figure 5.3** where both the outer mesh and the inlet patch mesh are reported for reference.
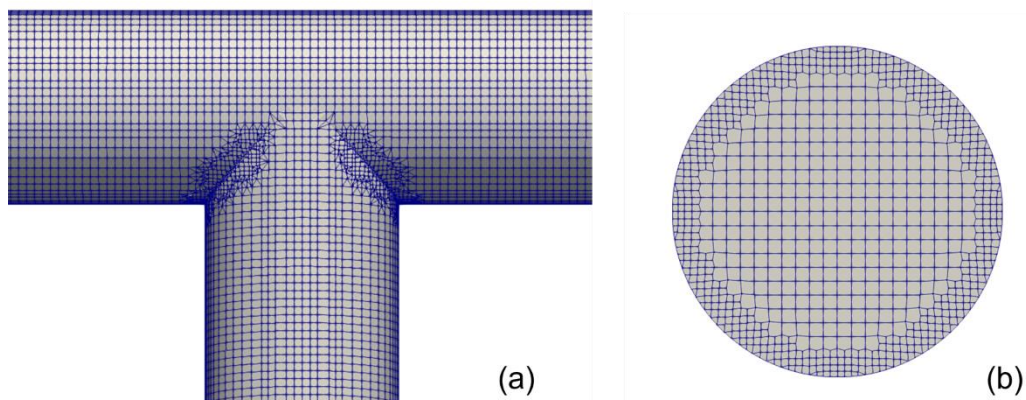

Figure 5.3 Details of the mesh for T-fitting under laminar conditions: outer mesh (a) and inlet patch mesh (b).

A similar mesh was chosen for the Y-fitting under laminar conditions and is shown in **Figure A2.4**. In the case of T- and Y-fittings under turbulent conditions, instead, layers were added close to the wall, and the resulting meshes are displayed in **Figure A2.5** and **Figure A2.6**. Once the optimal grid was selected and the simulation ran, the ParaView (version 56) application (Ayachit, 2018) was used to track the trajectories of tracers through the flow. As previously mentioned in **Chapter 3**, the filter 'Stream tracer with custom source' was used in ParaView. The streamline integration was tuned by choosing a "forward" direction and a maximum streamline length. The latter parameter was chosen high enough so as to follow the complete trajectories of the particles throughout the geometry. The seed point locations were given as input to the integrator, and their release is described in **Section 5.2.1**.

5.2 Results

5.2.1 Velocity and residence time study

In the studied fittings, the fluid does not flow through the entire geometry. Instead, it is made apparent that there is a zone where particles enter and stay for a long time at a low velocity. If we consider the time scales of vial filling, this zone can be considered a "dead zone" (a zone from which trapped particles will not be released before the filling ends) and will be referred to as such in the present article.

These characteristics differ from the tubing geometry, where an integral operation on the domain was sufficient and tracking individual particles and investigating their statistical behavior was not needed. Here, particle tracking through streamlines was necessary and offered fluid dynamics data that integral analyses are unable to provide. **Figure 5.4** shows an instance of fluid dynamics inside the T-fitting (a) and Y-fitting (b) in laminar conditions where 520 particles were followed through their trajectories. It can be observed that a significant number of particles cross the "dead zone", which is (almost) totally separated from the rest of the domain. In particular, over-analysis of 520 particles under laminar (and turbulent) conditions resulted in the finding that around 5% of the entire flowrate crossed the "dead zone". This underlines the importance of analyzing these two-outlet fittings rather than pure flow deviators. Particle tracking inside the T- and Y-fittings under turbulent conditions, instead, is displayed in **Figure A2.7**.
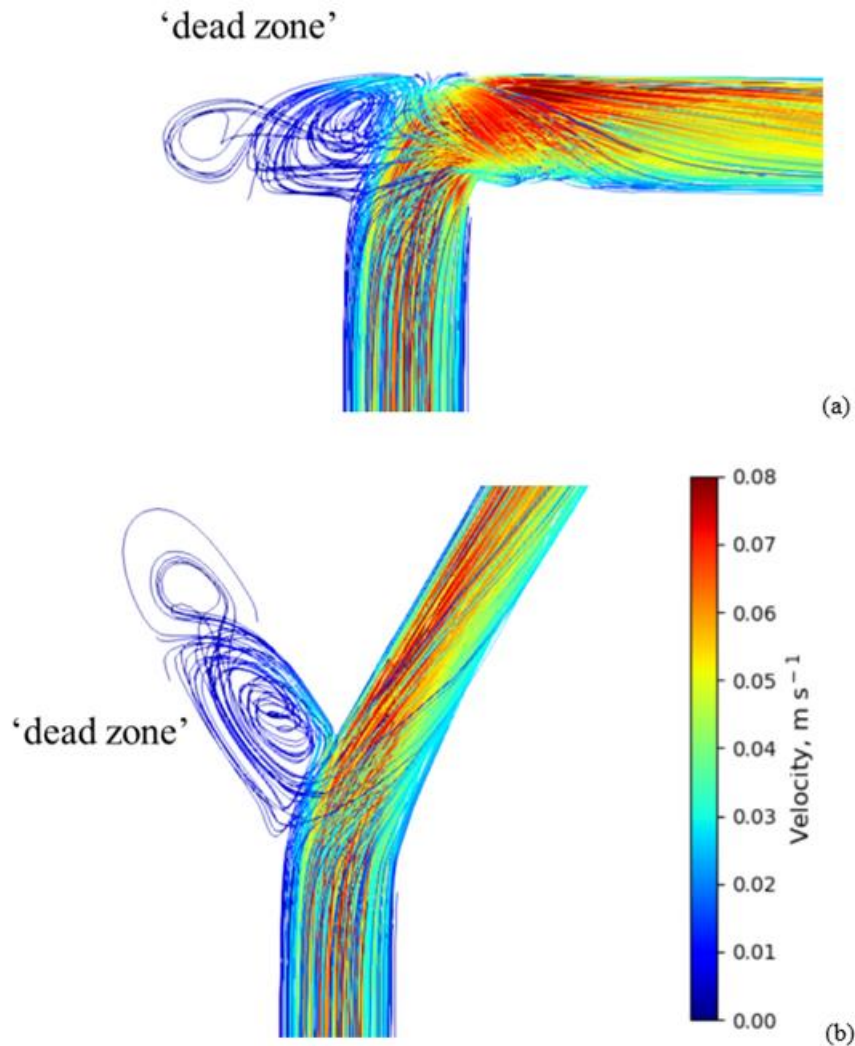
'dead zone'

'dead zone'

(a)

(b)

Figure 5.4 A total of 520 particles are followed through their streamlines, and their trajectories and velocities are displayed for T-fitting (a) and Y-fitting (b) under laminar conditions.

Finding the optimal quantity of particles to release was the subject of an initial inquiry.

Due to postprocessing requirements, the particles were dispersed at random throughout a circle with a diameter equal to 90% of the tubing's diameter, as shown in **Figure 5.5** (a). This decision was supported by the fact that only a small proportion of the formulation flows in the near-wall region, which is characterized by the lowest fluid velocities. **Figure 5.5** (b) displays the residence time of 520 particles released from the inlet of the fitting. It can be observed that, in this particular case (velocity of 0.042 m s^{-1}), the majority of particles take between 1 and 6 s to cross the domain, while some particles take substantially longer—between 6 and 40 s. These high residence time values are caused by particles passing through the dead zone, indicated by the black solid circles in **Figure 5.5** (b). Additionally, particles that deviate from their original direction and come close to the wall experience the no-slip condition, entering the lower velocity boundary layer and are indicated by the dotted circles. For the sake of clarity, particles passing through the dead zone with a residence time lower than 6 s are also identified by the red solid circles in the same figure. The upper limit used for this analysis, i.e., 6 s, was identified using the Tukey test (Tukey, 1977).
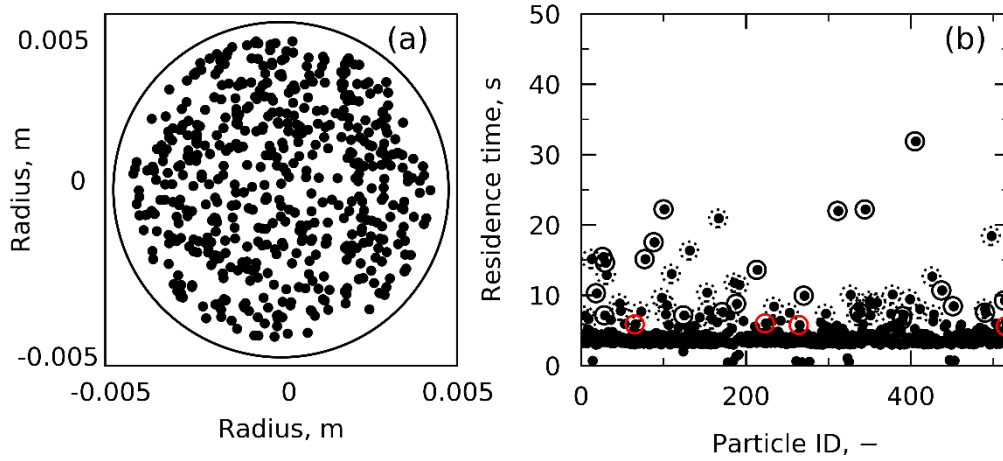
Figure 5.5 (a) A total of 520 seeds were randomly released at the inlet of the connector on a surface with a diameter equal to 90% of the tubing diameter. (b) Particles' residence times. As visible from the x scale, 520 particles were released from the inlet of the connector.

The optimal number of particles to release was obtained by monitoring the average velocity, as illustrated in **Figure 5.6** (a). It was calculated by averaging the velocities of all the streamlines. In turn, the velocity for each streamline i was assessed as follows:

$$u_i = \frac{1}{\tau_i} \int_0^{\tau_i} u_i(t) dt$$

$$(5.1)$$

where t is the time step, $\boldsymbol{\tau_i}$ is the overall particle residence time, and $u_i(t)$ is the velocity at the relevant time step.
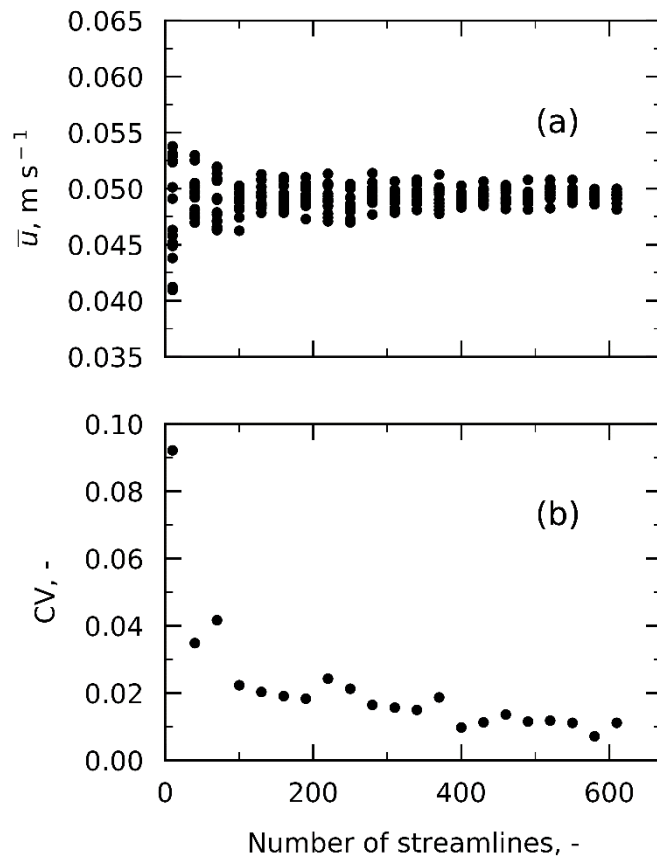
59

Figure 5.6 Average velocity calculated based on streamline information (a). The related coefficients of variation (CV) are reported in (b).

Between 10 and 610 particles were discharged from the fitting inlet. A total of 15 tests with varying (but still random) particle layouts were run at fixed particle numbers to control for statistical variance. For clarity, the coefficients of variation (CV) are shown in **Figure 5.6** (b). As it can be observed, the CV (defined as the ratio between the standard deviation and the average value) stabilized at very low values, under 2%, as the number of particles, and therefore streamlines, rose. Although values over 300 can be thought of as optimal, 520 particles were chosen because the increase in particles did not result in an appreciable increment in computational expense. The average inlet velocity in this test was set at 0.042 m s^{-1}. The average velocity in **Figure 5.6** (a) is slightly higher because particles were released onto a surface that was smaller than the actual tubing surface, thus ignoring some of the slowest particles.

5.2.2 First case study: laminar flow

The flow deviation causes noticeable local velocity gradients, which are visible in **Figure 5.4**, resulting in shear stress. To refer to the shear stress of a filling line operating unit, reference is often made to the maximum shear stress (Bee et al., 2009). However, these values are unrealistic for characterizing the shear stress distribution because they overestimate it (Duerkop et al., 2018b), resulting in incorrectly quantifying the effect of shear stress on product stability.

Consequently, an effort was made to develop approaches to appropriately quantify average shear stress and give a more realistic picture.

Approach 1—Maximum Shear Stress per Streamline

The highest shear stress for each streamline is taken into account in the first conservative approach. For simpler result visualization, probability distributions were employed (Kumar et al., 2020). Frequency histograms, Probability Distribution Function (PDF) and Cumulative Distribution Function (CDF) for the highest shear stress in the T-fitting are shown in **Figure 5.7** (a) and (b), respectively.
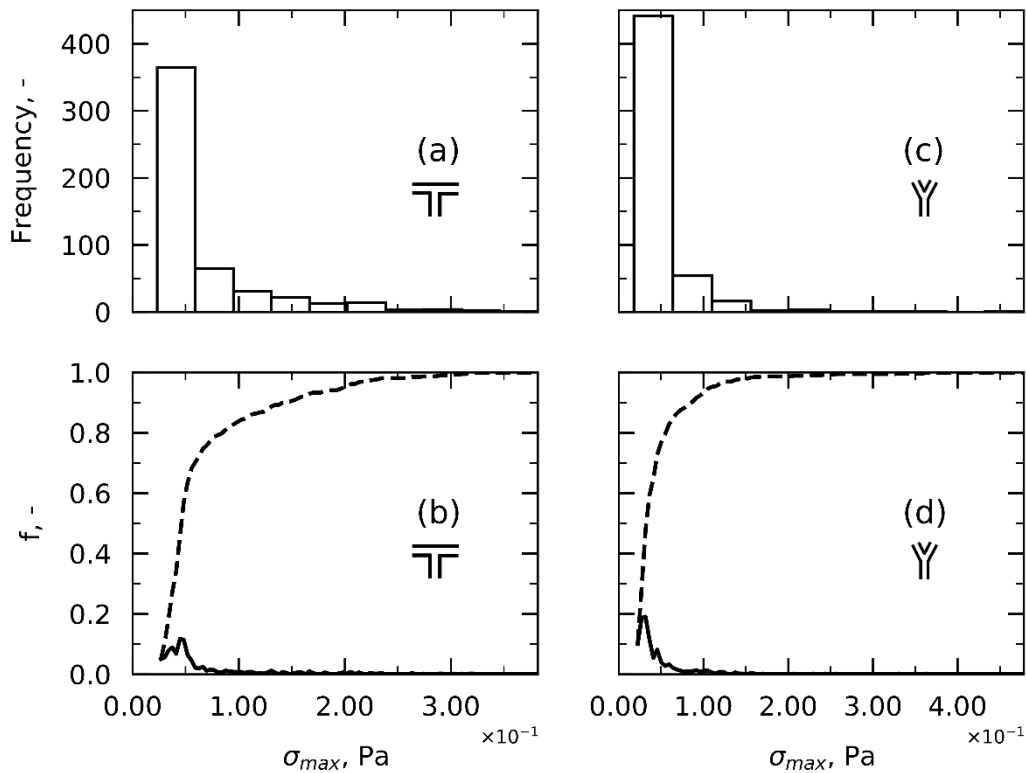
Figure 5.7 Frequency histograms of the maximum shear stress for T- (a) and Y- (c) fittings under laminar conditions. PDF (continuous line) and CDF (dotted line) are also presented for T- (b) and Y- (d) fittings.

Figure 5.7 (c) and (d) shows a similar trend for the Y-fitting. Sturges' rule was used to determine the number of bins in **Figure 5.7** (a), (c) (Scott, 2009), while **Figure 5.7** (b), (d) uses 100 bins, allowing for a clearer representation. This strategy is not only conservative—since it only considers the highest shear stress per particle along its trajectory—but it also does not account for how long a particle experiences a specific shear stress. However, as noted in the introduction, residence time appears to be important. As a result, new definitions were developed.

Approach 2—Damage Factor

A new quantity called damage factor (DF) was introduced, drawing on earlier works (Charm and Wong, 1970a). Following **Equation 5.2**, DF for the streamline i takes into account the local shear rate γ and the relative time of exposure τ for each streamline. By employing this approach, DF becomes dimensionless and gives a quantitative idea of the cumulative damage to the product.

$$DF_i = \int_0^{\tau_i} \gamma_i(t)dt$$

(5.2)

The trapezoidal rule was used to estimate the integral (Atkinson, 1989), using as the resolution of partition the time step of the integrator selected in ParaView. **Figure 5.8** depicts the findings of this approach for T- and Y-fittings under laminar conditions in terms of the probability distribution for easier understanding. It is clear that most streamlines have a low DF, but a few have a significantly larger DF. In order to determine which particles were causing such high DF values, we carried out a further examination. It was found that, despite experiencing small shear stress, particles with a large residence time (introduced in **Section 5.2.1**) and a relatively low shear rate can result in high values of DF. These high DF values, however, are not representative because it is reasonable to assume that particles that experience low shear stress for a long period of time do not contribute as much to damage as particles subjected to high shear stress for short periods.
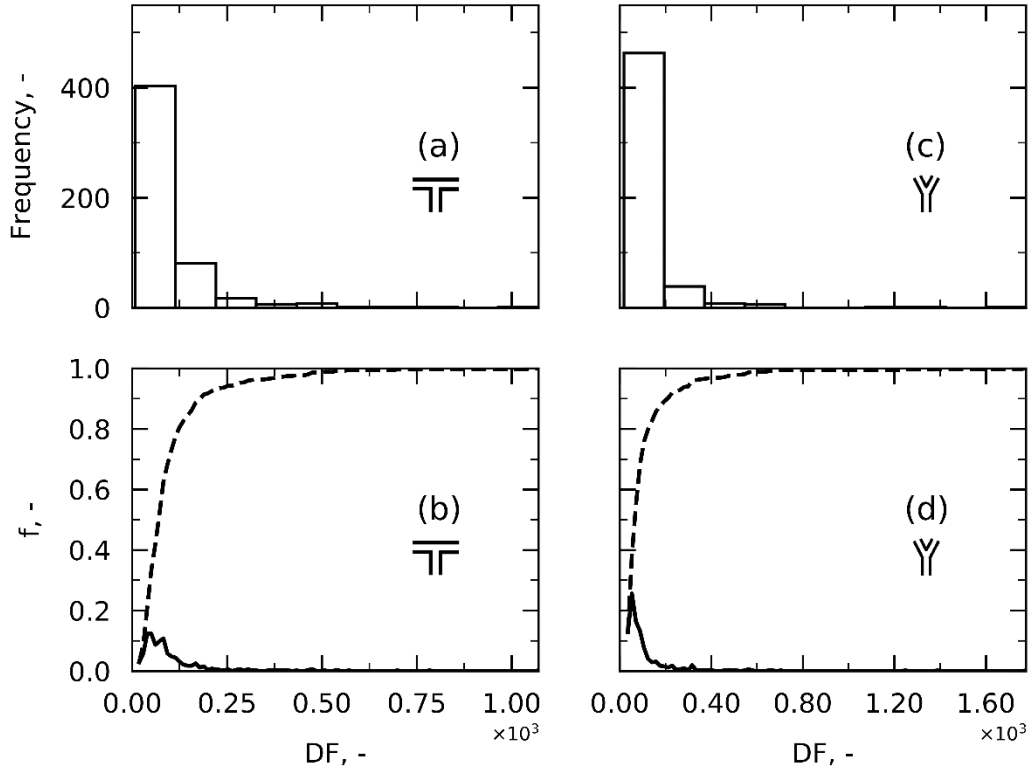
Figure 5.8 Frequency histograms of the DF for T- (a) and Y- (c) fittings under laminar conditions. PDF (continuous line) and CDF (dotted line) are also presented for T- (b) and Y- (d) fittings.

Approach 3—Damage Fitting Factor

It can be assumed that there is a threshold below which it is pointless to "count" the shear stress' contribution to damage. Therefore, it was decided to introduce one such arbitrary threshold. Thus, we have chosen to have a shear account for the accumulation of damage only when its value is greater than the maximum shear rate in fitting-equivalent tubing (γ_t). Damage fitting factor (DFF) is the name of this factor, and the formula is as follows:

$$DFF_i = \int_0^{\tau_i} \Gamma_i(t) \, dt$$

(5.3)

where:

$$\Gamma_i(t) \begin{cases} 0 & if \ \gamma_i(t) \le \gamma_t \\ \gamma_i(t) & if \ \gamma_i(t) > \gamma_t \end{cases}$$

(5.4)

Results for T- and Y-fittings under laminar conditions are reported in **Figure A2.8**. This method allows low-shear stress to be neglected. However, it is still very sensitive to the particles' residence time and domain size since it is a cumulative function and not an average.

Approach 4—Damage Critical Factor

Approach 4 is very similar to Approach 3 but introduces a different threshold. As explained in the Introduction, it was suggested that shear rate only becomes significant when it exceeds a critical value, and many authors attempted to identify this key value.

$$DCF_i = \int_0^{\tau_i} \Gamma_i(t)\, dt$$

(5.5)

where:

$$\Gamma_i(t) \begin{cases} 0 & if\ \gamma_i(t) \leq \gamma_c \\ \gamma_i(t) & if\ \gamma_i(t) > \gamma_c \end{cases}$$

(5.6)

Here, **Equation 5.5** can be used to determine the damage critical factor (DCF) for a specified product, where γ_c is represented by its critical shear rate, if any such threshold is identified. To provide an example, γ_c was chosen to be 30% of the fitting's maximum shear rate.

The results of the application of Approach 4 for T- and Y-fittings under laminar conditions are reported in **Figure A2.9**. The comparison between Approaches 2, 3, and 4 for T- and Y-fittings under laminar conditions is presented in **Table 5.1**. To allow for comparison, average quantities were calculated among all the streamlines.

Table 5.1 Comparison in $\overline{DF}$, $\overline{DFF}$, and $\overline{DCF}$ for T- and Y-fittings under laminar conditions.

Case	v, m s⁻¹	$\overline{DF}$, -	$\overline{DFF}$, -	$\overline{DCF}$, -
T-	0.042	97.30	33.93	2.89
Y-	0.042	105.10	44.84	0.16

When a threshold to the shear rate is introduced ($\overline{DFF}$, $\overline{DCF}$), the cumulative damage decreases within both shapes of fitting. However, it is not possible to make a direct comparison between T- and Y-fittings under the same fluid dynamic regime; that is because these damage factors are closely related to domain size. A higher damage factor is not necessarily due to higher stress but perhaps to a larger domain and thus longer paths to the product. These considerations highlight the need for a definition based on average rather than cumulative functions to facilitate qualitative and quantitative comparisons, which still takes into account shear stress peaks.

Approach 5 – Time-Averaged Shear Stress

The shear stress per streamline is time-averaged across its trajectory, as follows:

$$\sigma_i = \frac{1}{\tau_i} \int_0^{\tau_i} \sigma_i(t)\, dt$$

(5.7)

The trapezoidal rule was then used to estimate the integral, (Atkinson, 1989) using as resolution of partition the time step of the integrator selected in ParaView. The average shear stress is then calculated as follows:

$$\bar{\sigma}_5 = \frac{1}{m} \sum_i \sigma_i$$

(5.8)

where m is the number of streamlines.

The results of this approach are presented in the next paragraph, where a comparison with Approach 6 is outlined.

Approach 6 – Time-Averaged Shear Stress weighted on flowrates

In line with the results reported in our earlier study an even more realistic measure of the average shear stress can be obtained by weighting the local shear stresses on the relative flowrates. Since particles are released randomly from the fitting inlet, this weighting operation is equivalent to sending particles in a proportional amount to the actual flowrate. The optimal number of particles to release was assessed by monitoring the average velocity through the fitting. Hence, since the chosen number is guaranteed to describe the whole fluid dynamics within the fitting, the area of influence of the individual streamlines (A_i) was given by the ratio of the cross-sectional area to the number of streamlines. Hence, Approach 6 was developed as follows:

$$\bar{\sigma}_6 = \sum_i \left(\frac{1}{\tau_i} \int_0^{\tau_i} \sigma_i(t)\, dt \right) * \frac{w_i}{w_{tot}}$$

(5.9)

where the local weights corresponded to the relative flowrates and were evaluated as:

$$w_i = A_i \frac{1}{\tau_i} \int_0^{\tau_i} u_i(t)\, dt$$

(5.10)

with u being the velocity at the relevant time step and i the streamline index.

65

Figure 5.9 presents the comparison between Approaches 5 and 6 under laminar conditions for T- and Y-fittings.
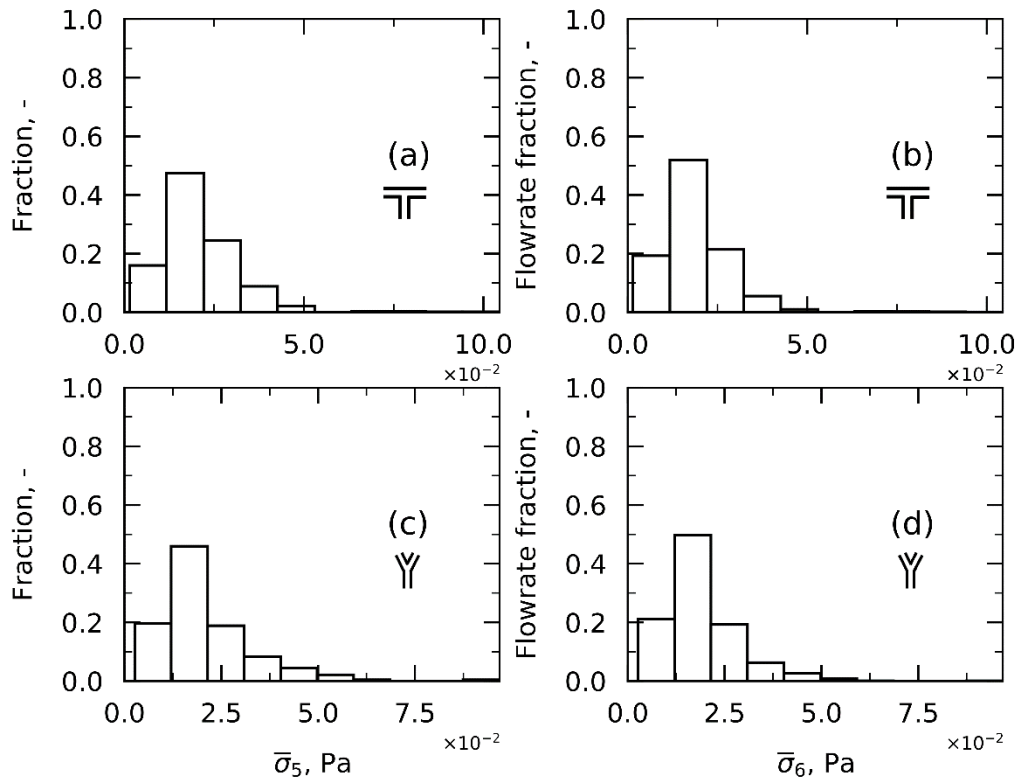

Figure 5.9 Average shear stress according to Approach 5 (a) and Approach 6 (b) is monitored by varying the number of streamlines and the number of tests per streamline for T-fitting under laminar conditions. Figures 8 (c) and (d) refer to Y-fitting.

The main difference apparent in using the two approaches can be observed by looking at the near-zero shear bars for T-fitting in **Figure 5.9** (a) and (b) (or Y-fitting in **Figure 5.9** (c) and (d)). When Approach 6 is used, these bars are shifted towards higher values on the y-axis which means that their weight is worth more. This is because Approach 6 allows the shear contributions to be considered in a proportional fashion to how much product actually passes through the fitting at the various locations, *i.e.*, the local volumetric flowrate.

5.2.3 Second case study: turbulent flow

Similar investigations to those reported under laminar regime were conducted for T- and Y-fittings under turbulent conditions. The mathematical details for the proposed equations are already presented in **Section 3.1.2**. Here, the relevant results are shown and the comparison with respect to the laminar flow are drawn. Accurate analysis on the mesh layout was conducted in the framework of the $\kappa - \omega$ *SST* turbulent model. The turbulent properties in the inlet branch

of the fitting, where the fluid dynamics develop as in a straight tubing, varied as displayed in **Figure 5.10**.
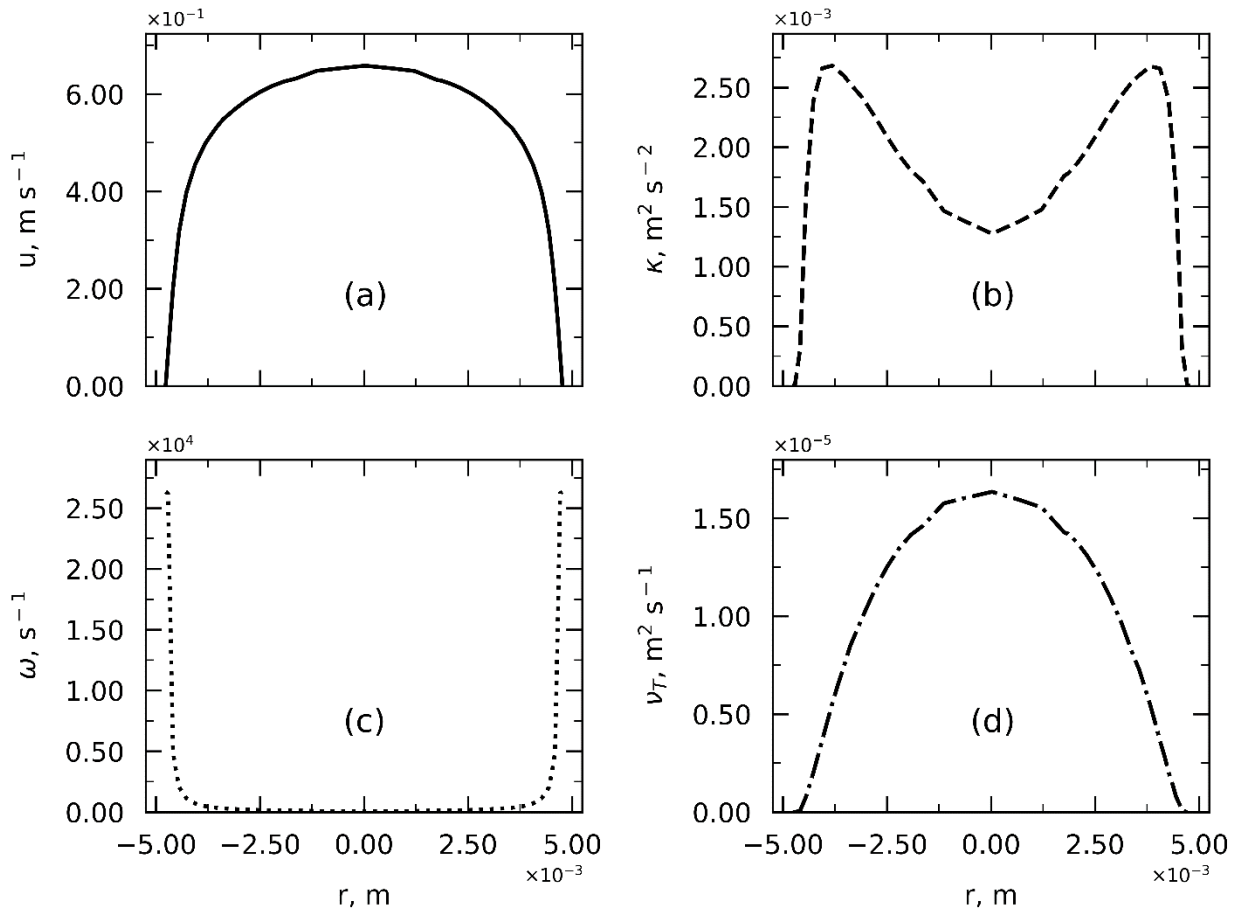

Figure 5.10 Velocity profile in the cross-section of the straight part of the connector is shown in panel (a). Trends of turbulent properties κ, ω and ν_T are presented in panels (b), (c) and (d), respectively.

By monitoring the local properties within the fittings, peaks in shear stress were found as a result of the abrupt change of direction of the flow. The aforementioned Approaches 1 to 4 were used to describe the distribution of shear stress and the results are presented in **Figure A2.10**, **Figure A2.11**, **Figure A2.12**, **Figure A2.13** and **Table A2.1**. In a similar fashion to what is reported previously, Approach 1 appeared too conservative while Approaches 2, 3, and 4 did not allow precise comparison as too dependent on domain size. Again, Approaches 5 and 6 proved suitable to describe the relationship between shear stress and residence time. Their comparison is shown in **Figure 5.11**.
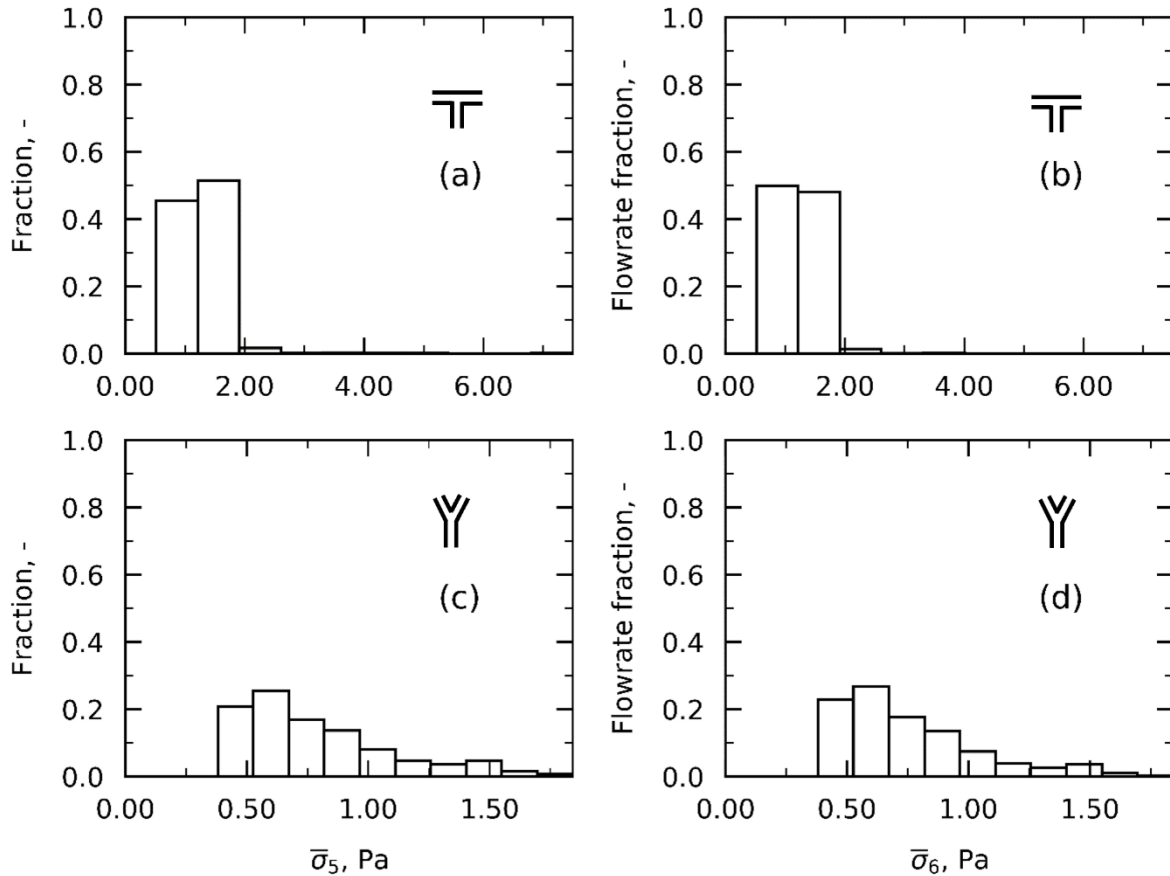
Figure 5.11 Average shear stress according to Approach 5 (a) and Approach 6 (b) is monitored for T-fitting under turbulent conditions. Panels (c) and (d) refer to Y-fitting.

Similar considerations for the comparison between Approaches 5 and 6 can be drawn for turbulent flow. By weighting the local shear stresses on the volumetric flowrate fraction, the average shear stress decreases because the higher shear stresses are experienced by a small portion of the entire product and vice versa, which can be noted later in **Table 5.2**. As for laminar conditions, Approach 6 can provide a more realistic picture of the shear stress distribution.

5.2.4 Comparison with shear stress in straight tubing

This chapter presents new approaches for numerically evaluating the average shear stress across different fittings. Together with our previous article on tubing, they provide a new way to quantify the distribution of shear stress (or rates) in a filling line under given operating conditions. However, they differ from the way the models were designed; in the tubing case, under the steady state assumptions, velocity and shear stress profiles did not change along the length of the tubing and, therefore, integral operations over a slice of the tubing were sufficient. In a fitting, however, the deviation of the flow direction caused the particle to differ from their stationary trajectories; this is the reason why the shear was evaluated along the particle's trajectories, and the relevant variables detected.

For a clearer representation, **Table 5.2** summarizes the relevant results. Using the models developed in the previous article and reported in **Chapter 4**, the average shear stress weighted on the local flowrates ($\bar{\sigma}_{tub}$) was calculated; then, it was compared with the value calculated using Approaches 5 and 6 for fitting, $\bar{\sigma}_{5,fit}$ and $\bar{\sigma}_{6,fit}$, respectively. A new quantity ($\Delta_{tub,fit}$) was identified and calculated as follows:

$$\Delta_{tub,fit} = \frac{\bar{\sigma}_{tub} - \bar{\sigma}_{6,fit}}{\bar{\sigma}_{tub}}$$

(5.11)

It can be observed that in the T-fitting under laminar conditions the difference $\Delta_{tub,fit}$ in the average shear stress (between $\bar{\sigma}_{tub}$, $\bar{\sigma}_{6,fit}$) is rather small. On the other hand, $\Delta_{tub,fit}$ is much higher in the T-fitting under turbulent conditions. As for the Y-fitting, under both laminar and turbulent conditions, $\Delta_{tub,fit}$ is smaller or equivalent to the T-fitting and may be explained by the fact that the change of flow direction is not as sharp.

Table 5.2 Comparison in the shear stress between fitting and tubing under laminar and turbulent conditions).

-	Regime	$\bar{u}$, m s^{-1}	$\bar{\sigma}_{tub}$, Pa	$\bar{\sigma}_{5,fit}$, Pa	$\bar{\sigma}_{6,fit}$, Pa	$\Delta_{tub,fit}$
T-	Lam	0.042	1.88×10^{-2}	2.10×10^{-2}	1.92×10^{-2}	2%
Y-	Lam	0.042	1.88×10^{-2}	2.08×10^{-2}	1.89×10^{-2}	1%
T-	Turb	0.500	7.69×10^{-1}	12.3×10^{-1}	12.1×10^{-1}	57%
Y-	Turb	0.500	7.69×10^{-1}	8.13×10^{-1}	7.84×10^{-1}	2%

The models presented show that in a filling line consisting of tubing and fittings, the fittings represent the largest source of shear stress. Under turbulent flow conditions, in particular, the difference between the average shear stresses generated in the T-fittings and tubing becomes even more significant, which highlights the relevance of the present work. Nonetheless, for the other fitting shape analyzed, *i.e.*, Y-fitting, the discrepancy is not as significant. Finally, in a filling line comprised of a defined number of fittings, Approach 6 could be implemented to quantify in a realistic way the average shear stress experienced by the product when flowing through the fitting.

5.3 Conclusions

In the present work, CFD simulations were employed to investigate the fluid dynamics within T- and Y-fittings under both laminar and turbulent conditions. The potential streamlines of particles were tracked to gain more insights into the fluid path and to detect local properties. Several relations were then proposed to identify the shear stress distribution; particularly, one was identified (Approach 6) which turned out to be the most suitable for our purposes, which

takes into account the local shear stresses along the particle's trajectory and the relative flowrates. This helps to provide a more realistic picture of the shear stress distribution since it is equivalent to considering particles in a proportional way to their actual amount. In a broader perspective, the same workflow and approach for evaluating the shear stress distribution could be used on fittings or connectors of different shapes but also other operating units.

The future steps of this study could involve (i) extending the analysis on shear stress to the other components present in a filling line for parenteral protein drug products and (ii) performing experimental tests to assess the impact of such shear stress on product stability.

Chapter 6

The role of sterilizing filters

Filtration plays a pivotal role in ensuring the absence of microbiological or particle contamination in the drug product. To this end, a pressure-driven technique process pushes the product through a semi-permeable membrane in an effort to separate the contaminants from the solution (Jornitz, 2020) and verify that the product meet the sterility criterion*. As mentioned in **Chapter 2**, in accordance with the United States Food and Drug Administration and the United States Pharmacopoeia guidelines, sterilizing filters should be product compatible (Kong, 2006) and made of non-fiber releasing materials with a nominal rating of 0.2 μm and 0.22 μm respectively (Meltzer and Jornitz, 2003; Ramstorp, 2003). Such membranes can be placed in different housings, depending on the need. Typically, studies for initial screening and preliminary filter sizing are performed using flat membrane discs (Giglia and Yavorsky, 2007). At manufacturing scale, on the other hand, capsule (Dixit, 2008) or cartridge (Kumar et al., 2015) filters with membrane pleating are generally employed; the pleating allows a larger area of the filter medium to be packed in such a way to increase performance in terms of fluid flowrate and total throughput, meaning the amount of fluid which can be processed before the filtration is stopped (Brown et al., 2009; Dippel et al., 2021). For the sake of clarity, a schematic of these filters is given in **Figure 6.1**. Such membranes have a characteristic thickness of hundreds of μm and a length on the order of cm.

---

* The work described in this chapter has been previously published in "Moino, C., Agostini E., Albano, A., Bellini, M., Bourlès, Scutellà, B., E., Boccardo, G., Pisano, R., 2024. Analysis of the shear stresses in a filling line of parenteral products: The role of sterilizing filters. *Separation and Purification Technology*, 344, 127248"
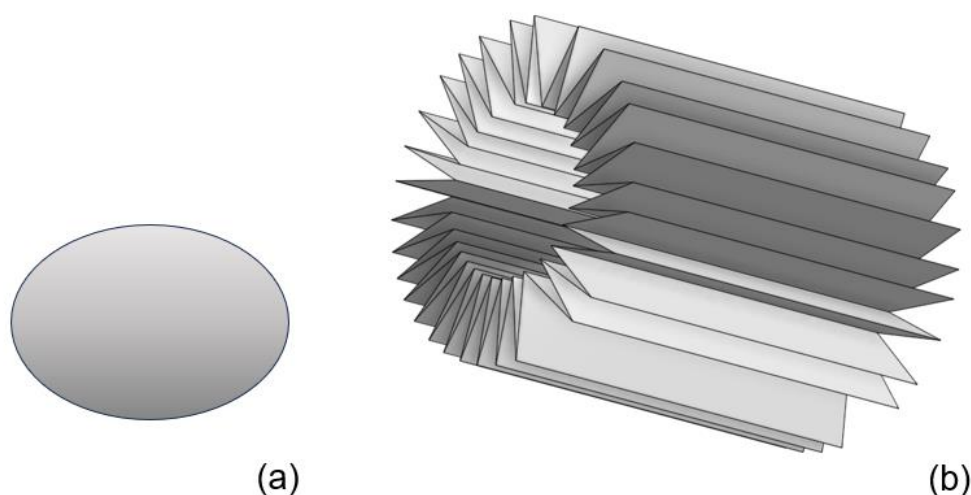
Figure 6.1 Schematic of the housing (a) and membrane (b) for a Durapore disc and cartridge, respectively.

Scale-up is necessary to pass from bench-scale to manufacturing-scale and vice versa for scale-down (Kumar et al., 2015). Linear scale-up (or scale-down) assumes that the filtration area increases proportionally to the volume of the solution to be processed; however, a more thorough understanding of scale-up from discs to pleated filters has become necessary and is generally referred to as Safety Factor (SF) (Du et al., 2022). It considers both the Effective Filtration Area (EFA) and the filtration capacity (C), i.e., the cumulative filtrate volume, defined as the volume per unit area processed, as follows:

$$SF = \frac{\left(\frac{EFA}{C}\right)_{comm}}{\left(\frac{EFA}{C}\right)_{lab}}$$

(6.1)

where $comm$ and lab stand for commercial and laboratory scale, respectively.

This factor is introduced to minimize the risk of underestimating the filter area and compensate the variability usually connected with upscaling processes, which include differences in flow geometries, extra-membrane flow resistances, and fouling phenomena (Giglia et al., 2010). There is a wide range of potential SF and a thorough list is reported in Haindl et al. (Haindl et al., 2020) who found values from 0.75 to 2.5 in their review of the literature, although calculations performed on different filters gave them a much higher SF (7.17).

Membrane characterization is fundamental to gain insights into the porous structure and get medium properties, such as porosity, mean pore size and pore size distribution. In addition, it can be used to inform computer simulations of digital structure reconstruction in an effort to obtain a realistic representation of the porous media. This characterization can be performed

through several techniques, including Scanning Electron Microscopy (SEM), Tomography, and Confocal-Laser-Scanning Microscopy (CLSM).

In particular, SEM is a magnification tool which makes use of focused beams of electrons to obtain information on the porous structure. One of the missing features of SEM is that it only provides morphological information thus making it invaluable in getting 3D information. Similarly, Transmission Electron Microscopy (TEM) can provide high-resolution views of objects but is limited to 2D images and cannot identify 3D morphology of samples. Another valuable technique is the nano/micro-Computed Tomography (CT) which does not need any invasive procedure prior to imaging and allows 3D characterization of the membrane (Vásárhelyi et al., 2020). There are different types of CT scanners that allow for different sample size and resolution, thus providing multiscale opportunities with CT. The typical resolution of micro-CT and nano-CT scanners, for instance, is around 1-100 μm and as low as 0.5 μm, respectively (du Plessis et al., 2017). Similarly, CLSM can be employed for this purpose. After the 2D images of the 3D membrane are obtained, they are used in combination with computer-based image analysis to derive a complete 3D representation of the membrane structure, (Ley et al., 2018) which can be further used to perform Computational Fluid Dynamics (CFD) analysis. In a former work, Affandy (Affandy, 2013) reports a case of 2D reconstruction of sterile filters passing through TEM images. For 3D reconstruction, on the other hand, the analyses went up to dimensions of 8 μm. As sufficiently high-resolution 3D images of the micro-structure of real porous membranes are difficult to obtain by tomographic methods, detailed studies are more and more based on 3D digitalized models, obtained by various stochastic reconstruction techniques (Agostini et al., 2022; Capozzi et al., 2018; Talukdar et al., 2002).

CFD is being utilized more and more in pharmaceutical applications, enabling process monitoring and optimization without the requirement for products (Pordal et al., 2002). In such a realm, two approaches are generally used to deal with a porous medium, named 'microscale' and 'macroscale' approaches. The first strategy takes into account the actual pore size and morphology inside the membrane or the porous medium in general, which contributes to a complex fluid dynamics behavior of the fluid (Boccardo et al., 2014; Marcato et al., 2023). The macroscale approach, on the other hand, is an averaged representation of the pore-scale process and is a computationally efficient alternative to microscale model (Battiato et al., 2019; Whitaker, 2013); however, it is not suitable to detect local fields through the pores, i.e., shear stresses. For this reason, a microscale framework was chosen for the present analysis.

Here, a published workflow (Agostini, 2023) has been followed for the design of a computational model that replicates the real membrane in terms of pore size distribution, porosity, and permeability. Furthermore, shear stress exposure to the product is estimated considering the shear history of mass-less tracers. Different flow conditions and membrane *EFA* are tested and a relation between the inlet velocity and the resulting shear stress found. To the best of our knowledge, this analysis is brand-new compared to the most shear stress estimations in filtration units, which generally rely on mathematical calculations (Nema and Ludwig, 2010).

6.1 Methods

6.1.1 Experimental set up

Experimental work was conducted in order to assess the permeability of a typical sterilizing membrane used for filling purposes. The Durapore membrane ("Millipore Durapore Membrane Filter, 0.22 μm," n.d.) was adopted, being a membrane with homogeneous average pore size, without upstream / downstream side, like other membrane in Polyether Sulfone (PES) for instance (Fallahianbijan et al., 2021). It is a hydrophilic Polyvinylidene Fluoride (PVDF) membrane used for applications requiring the highest degree of sterility assurance. Many different housing configurations are available for such membrane, including cartridges, capsules, disc membrane (Millipore, n.d.). This last membrane has a porosity (ε) of 70%, a depth of 125 μm and a diameter of 47 mm. SEM was used to assess the surface and cross-sectional morphologies of the sterilizing membrane. For cross-section images, the samples were cut in liquid nitrogen using a sharp knife. This analysis provided an idea of the morphology of the structure and proved the uniformity of the pore size distribution. An example of cross-section image is shown in **Figure 6.2**, while **Figure 6.3** shows the experimental set up used in this study for the estimation of the membrane permeability; a Watson Marlow peristaltic pump was used to drive water across the disc (with Durapore membrane) at different flowrates.
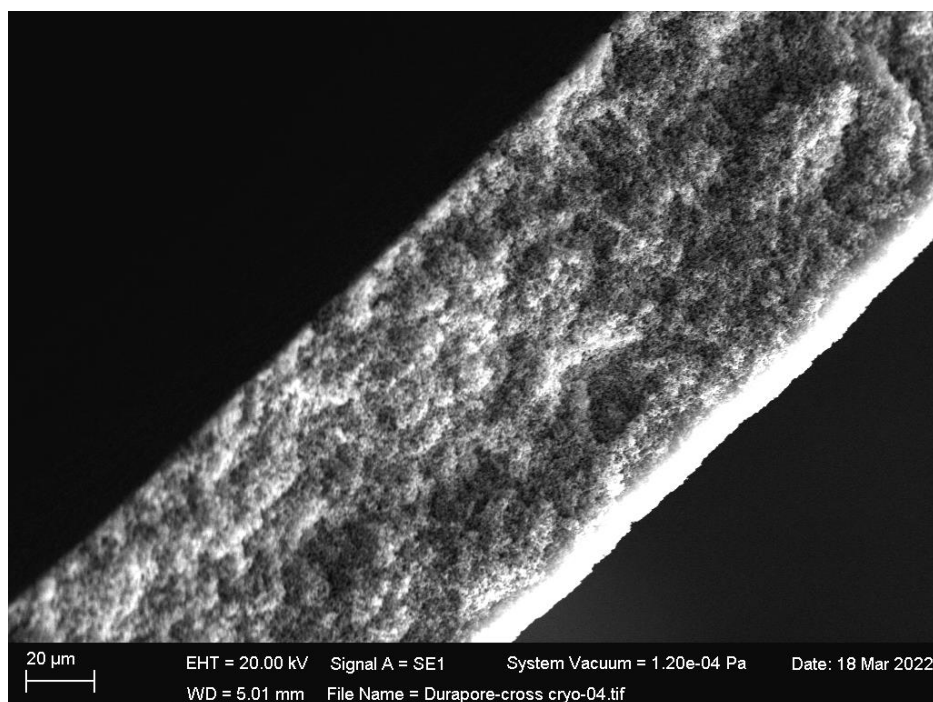

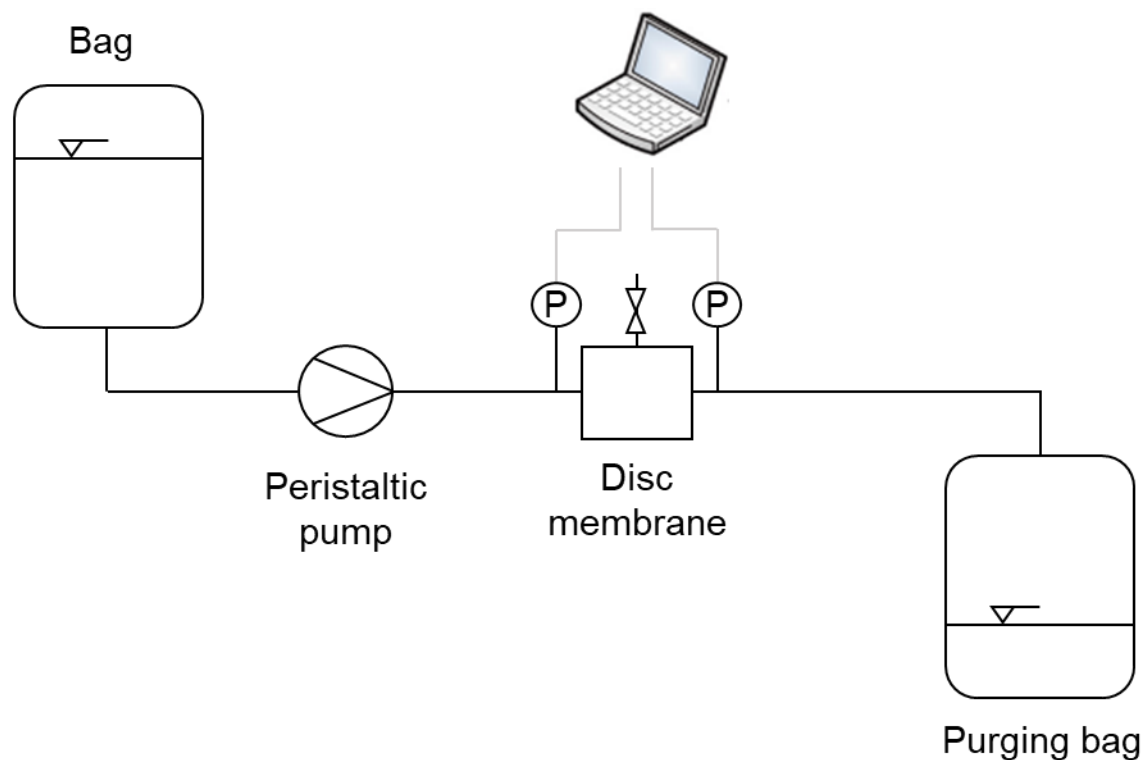**Figure 6.2** SEM cross section of the Durapore membrane.

Figure 6.3 Experimental set up that has been used for the estimation of the pressure drop across the membrane given a certain flowrate and, thus, its permeability.

Pressure sensors (P) were used to detect the pressure drop across a membrane filter when water was flowing through the circuit at different flowrates. The relationship between the inlet flowrate and the resulting pressure drop was found out to be linear, i.e., laminar condition that is (Xiao et al., 2017), and the trend is displayed in **Figure 6.4**. Three trials for each flowrate were run on clean membrane to account for experimental variance and the relevant coefficients of variation (CV) are also reported. For clarity, a higher CV can be observed for the 20 mL min^{-1} flowrate, which could be due to an experimental uncertainty in one of the three samples and the limited number of experimental data sets. Nonetheless, although nigher than the other flowrates investigated, the CV at 20 mL min^{-1} is still small and the overall linear trend in the pressure drop is preserved. Therefore, the pressure drop with the lowest CV was then selected, i.e. that at 40 mL min^{-1} and it was used to calculate the membrane permeability (k) using the previously reported **Equation 3.5**.
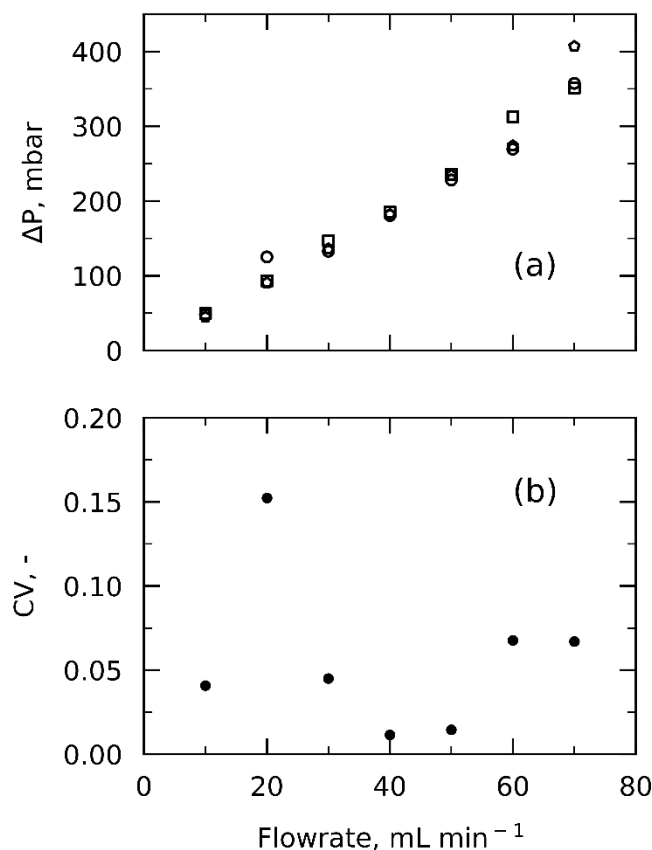
Figure 6.4 Pressure drop vs flowrate for three different data sets through the Durapore membrane in (a). Each data set is represented by a geometric figure (circle, square, pentagon). Coefficients of variation CV are reported in (b).

The estimated permeability was 2.63×10^{-15} m^2, which is in line with previous data (Na et al., 2022). It must be noted that k assessed with such experiments considers both the resistance provided by the filter's housing and the membrane pores. Nonetheless, as suggested elsewhere (Velali et al., 2020), the filter's housing resistance was assumed to be negligible because the pores undoubtedly make up the major contribution.

6.1.2 Numerical set up

In this work, a computational replica was achieved using the code developed previously by a doctorate student from Politecnico di Torino and available in (Agostini, 2023), which makes use of the software plugIm! (https://www.plugim.fr/). For the computational analysis of the fluid flow, on the other hand, the finite volume method-based open-source code OpenFOAM 9 (https://github.com/OpenFOAM/OpenFOAM-9) was used. The simulations were carried out on an HP workstation with eight logical processors and 16 GB of RAM. Python 3.8 was used for the post-processing of the simulations. For the sake of clarity, the details for the membrane and grid generation are reported in two separate sections.

Membrane generation

The workflow used for the development of the computational replica (Agostini, 2023) is composed of three distinct processes, including sphere aggregation, Voronoi tessellation, and concluding morphological operations. The number of spheres for the aggregation with the relative diameter (d_c), the repulsion factor (R), the size of the spheres and cylinders for the Voronoi tessellation (R_{node}, R_{strut}), and the resolution of the box were some of the parameters that were tuned.

Some details of the membrane are represented in **Figure 6.5**, which zooms on the representative cell.
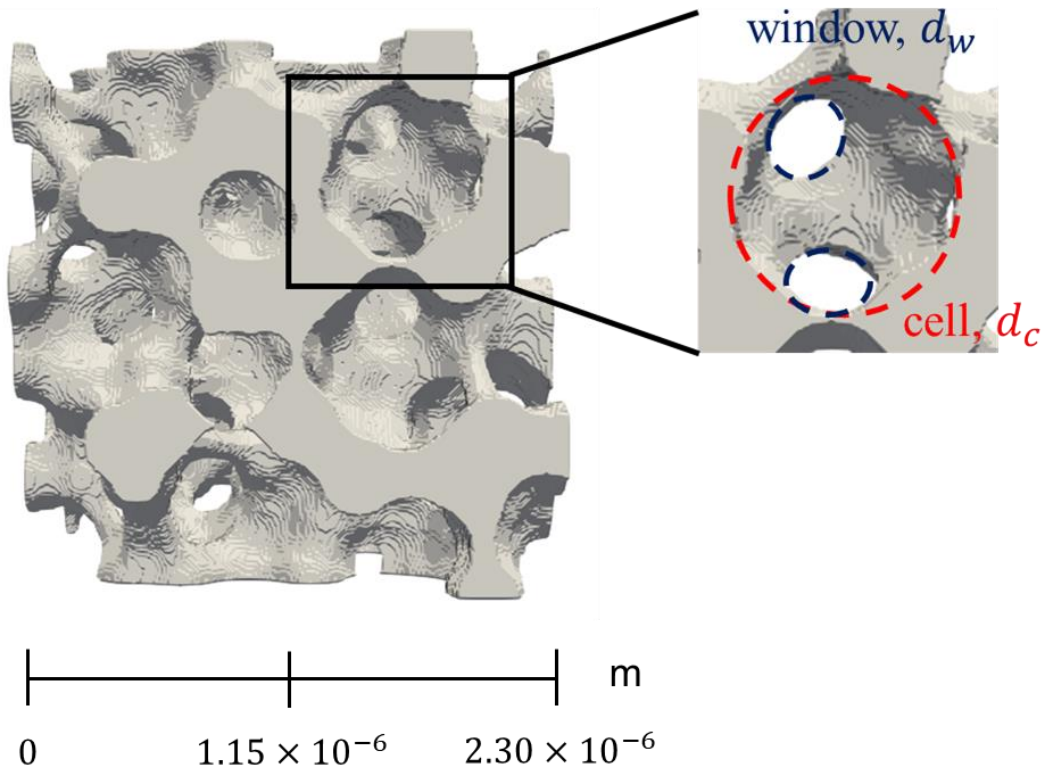
Figure 6.5 Cell unit of the membrane showing its components.

As a starting point, it was assumed that the given pore size equals the window diameter (d_w), which delimits the area where the fluid passes through. The relation between cells diameter and window diameter was found in (Inayat et al., 2012):

$$d_w = \frac{d_c}{2.3}$$

(6.2)

and it was therefore used to assess d_c for the initial sphere aggregation.

Based on (Agostini, 2023), the dimension of the box was chosen equal to five times the cell diameter; this value was found high enough so as to ensure the chosen computational domain is a representative elementary volume, which is defined as a volume surrounding a

point in which in all averaged attributes are independent on the size of the volume (Bachmat and Bear, 1986).

The structure was developed in order to meet the actual ε (provided by manufacturer) and experimental k. An iterative workflow was used until the desired ε and k were both achieved which is shown in **Figure 6.6**.
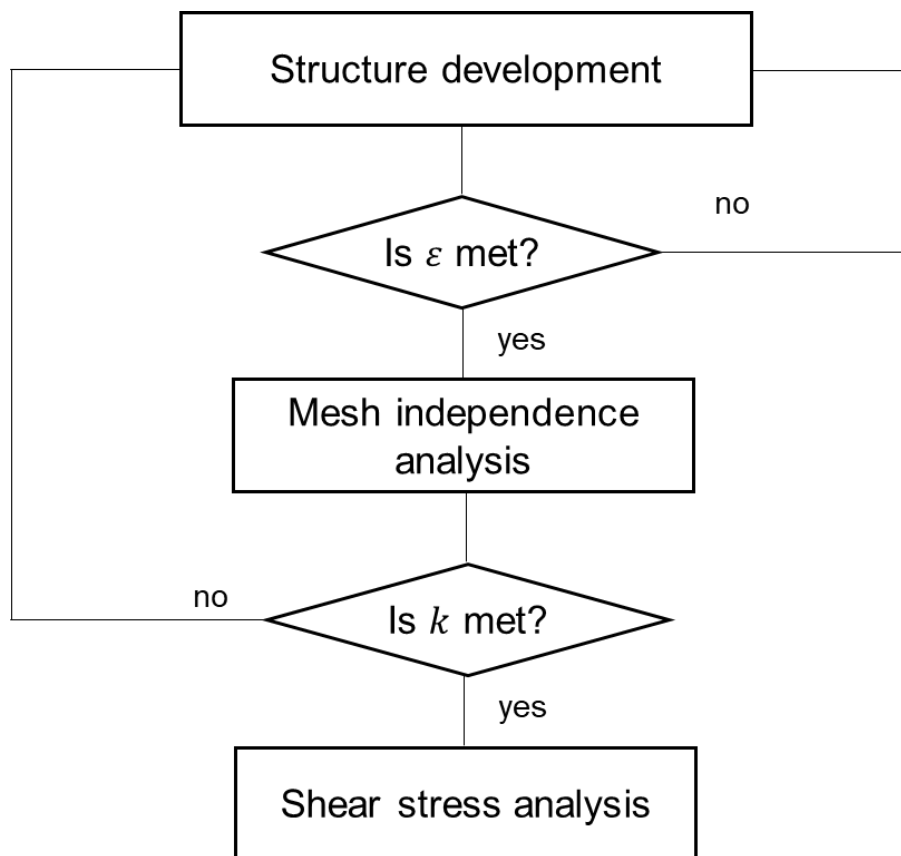

Figure 6.6 Numerical set up.

For the sake of clarity, **Table 6.1** reports the parameters that yielded the desired values for ε and k.

Table 6.1 Parameters used in structure development.

Parameter	Meaning	Value
NB	Initial number of spheres	380
Alpha	Compactness parameter	0.55
Beta	Compactness parameter	0.75
Repul	Repulsion	20
R	Spheres diameter	25
W	Box size in integers	250
R_node	Spheres diameter for the tessellation	17
R_strut	Cylinders diameter for the tessellation	6
Operation	Morphological operation	Closing
Iter	Number of iterations for the tessellation	1
tv	Size of the chosen morphological operation	19
vx_res	Voxel resolution	9.2×10^{-9}

Further analysis on the membrane were carried out, using the poreSpy module available in python, which is a toolkit for microstructure investigation of porous media (Gostick et al., 2019). The resulting pore size distribution is shown in **Figure 6.7**, and it is consistent with experimental data from the literature (Na et al., 2022).
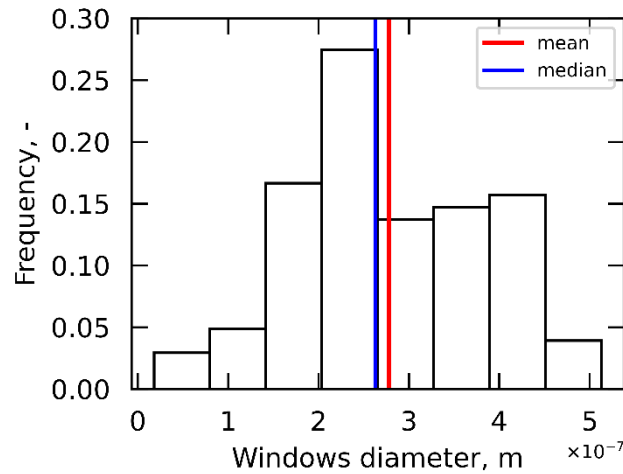

Figure 6.7 Pore size distribution. The mean and median values (2.8×10^{-7} and 2.6×10^{-7} m, respectively are also shown.

Grid generation

Pre-mixing and post development regions are added to ensure development of the flow prior to and past the actual membrane, as shown in **Figure 6.8** where the computational domain is displayed.
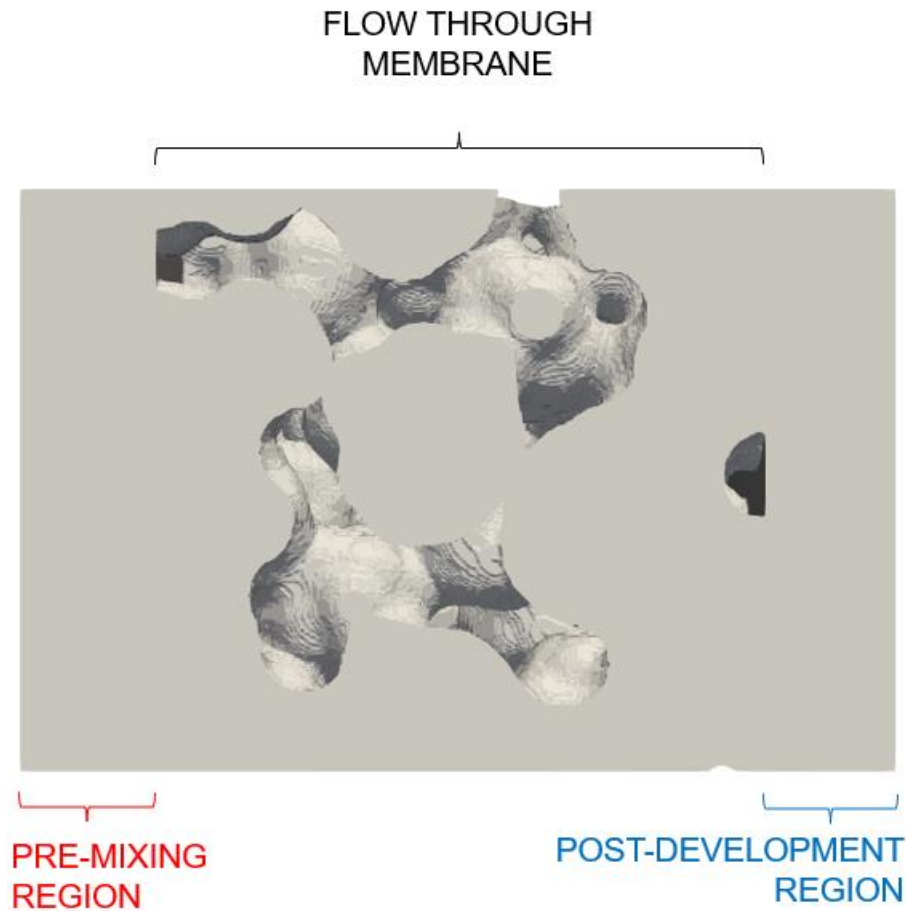
FLOW THROUGH
MEMBRANE

PRE-MIXING
REGION

POST-DEVELOPMENT
REGION

Figure 6.8 Computational domain. Pre-mixing and post-development regions are shown.

Special emphasis should be given to the boundary conditions. A uniform value of velocity was specified at the inlet boundary condition, while the no-slip and zero-gradient conditions were imposed at wall and outlet patches, respectively. Regarding pressure, a zero-gradient condition was selected for wall and inlet patches while a uniform value equal to 0 was chosen for the outlet. Beside these conventional boundary conditions for the main patches, the symmetry boundary condition was imposed to all the sides of the computational domain to mirror the field pattern along them.

A Newtonian incompressible fluid with water-like properties (Fischer et al., 2009) was considered. Steady-state conditions were assumed and the solver *simpleFoam* was used to perform the fluid flow simulations. Based on the initial experimental investigation, laminar regime was considered, where Reynolds number (Re) was evaluated as follows:

$$Re = \frac{\rho u_{pore} D_{pore}}{\mu}$$

(6.3)

where u_{pore} is the pore-scale velocity and D_{pore} is the mean pore diameter of the membrane, defined as the diameter of a sphere having the same volume as the mean pore. Darcy's velocity

(or surface velocity) in the porous medium (V_{ms}) was chosen from standard commercial filtration values using the following scaling equation:

$$\left(\frac{Q}{EFA}\right)_c = \left(\frac{Q}{EFA}\right)_{ms}$$

(6.4)

where EFA is the Effective Filtration Area of the filter given in m^2. For the commercial scale, capsules with EFA 864 and 6000 cm^2 respectively were considered and several operating conditions were tested (Q = 2500 mL min^{-1}, 1700 mL min^{-1}).

The membrane grid was developed by using two OpenFOAM utilities, named *blockMesh* and *snappyHexMesh*. The former is used to build a background structured hexahedral mesh, which is then used as a starting point to build a body-fitted grid via snappyHexMesh. The final grids were mainly comprised of hexahedral cells in such a way to ensure a good numerical performance of the solver. The grids were further refined close to the solid walls of the pores, thus resulting in cells of decreasing dimension moving from the pores walls to the bulk of the fluid.

A grid independence analysis was conducted in order to find the optimal mesh, resulting from a trade-off between computational cost and solution's accuracy. This was done by tuning two main parameters: the number of background cells in the initial background mesh and the level of refinement Ref performed by *snappyHexMesh* on the cells close to the solid pore surface. The values of the refinement level taken into account were $Ref = \{0, 1, 2\}$. The grid independence study was conducted by monitoring the pressure drop across the membrane, and the results are visible in **Figure 6.9**, where the relative error to the most computationally expensive grid are also shown for comparison.
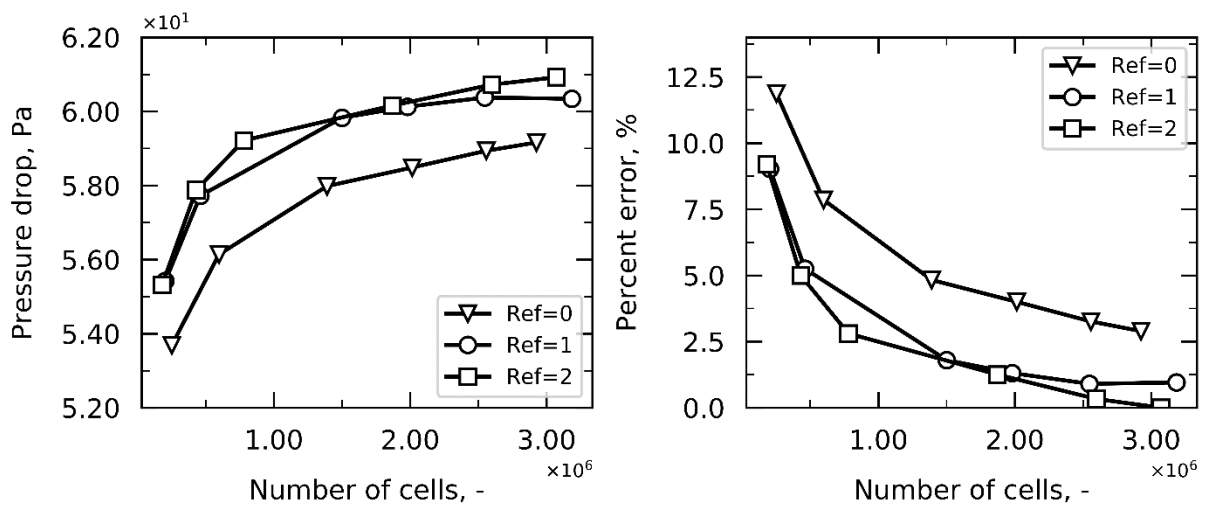

Figure 6.9 Grid independence analysis.

It can be noted that $Ref = \{0\}$ does not lead to an accurate solution. Therefore, a more computationally expensive mesh should be used. On the other hand, grids corresponding to $Ref = \{1, 2\}$ and a number of cells higher than 2×10^6 seem to result in more accurate and converging solution. For the subsequent analysis, the mesh with $Ref = \{2\}$ and around 1.9×10^6 cells was used. This led to a k of 2.55×10^{-15} m^2, with a small percent relative error with respect to the experimental value reported in **Section 6.1.1**, i.e., 3%.

Having as objective the evaluation of viscous stresses, an investigation of the microscale of the membrane became necessary. As mentioned, macroscale models solve equations for macroscopic, and thus averaged, quantities. Therefore, when a closer look at local quantities at the scale of the pores is needed, microscale investigations like the present one need to be performed.

6.2 Results

6.2.1 Streamlines and shear stress analysis

Following **Chapter 3**, innovative strategies were used to track biological particles of fluid through their trajectories and detect their relevant fields. This made it possible to develop shear stress statistics which accounted for the actual shear stress history of each individual particle. More specifically, as described in **Section 3.3**, the utility 'Stream tracer with custom source' available in ParaView (Ayachit, 2018) was utilized, whose seeds points were randomly given as an input in the pre-mixing region. To provide an example, **Figure 6.10** shows the streamlines for 200 seeds.
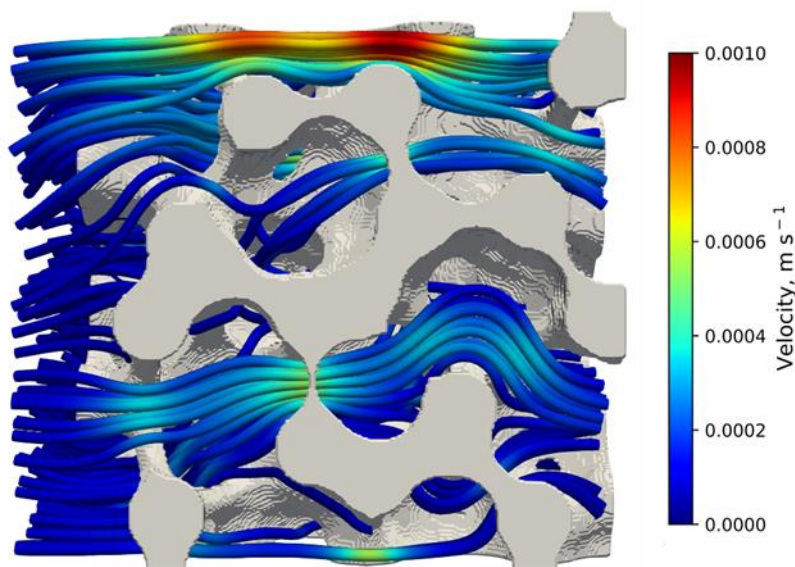

Figure 6.10 200 streamlines are followed through the porous medium and the local velocities are displayed.

Local fields across each streamline were then acquired through post-processing python scripts. A typical pore-scale velocity path is displayed in (a); local velocity and shear trends for such streamline can be observed in **Figure 6.11** (b).
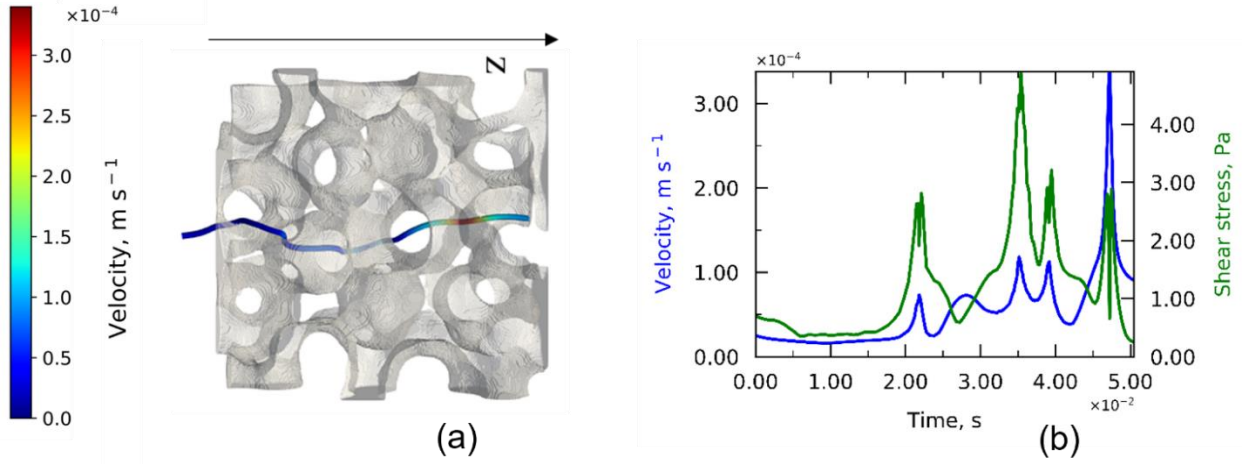

Figure 6.11 Streamline for an hypothetical particle released in the pre-mixing region (a), with Z being the flow direction. Velocity (in blue) and shear stress (green) are displayed (b).

It can be noted from **Figure 6.11** that local fields greatly vary through the geometry because of the complexity (and tortuosity) of the membrane structure; therefore, as cumulative definitions appeared too sensitive to domain size and hardly applicable, an average shear stress per streamline is calculated, as reported in **Equation 6.5**. The trapezoidal rule was used to estimate the integral and implemented through the 'trapz' function available in the numpy module in python. The averaged shear stress σ_i per streamline was therefore evaluated by time-averaging the shear stress along the streamline and using the relative flowrate w_i as weight.

$$\sigma_i = \sum_i \left(\frac{1}{\tau_i} \int_0^{\tau_i} \sigma_i(t)\, dt \right) * \frac{w_i}{w_{tot}}$$

(6.5)

$$w_i = A_i \frac{1}{\tau_i} \int_0^{\tau_i} u_i(t)\, dt$$

(6.6)

with $u_i(t)$ being the velocity at the relevant time step, i the streamline index. For the sake of clarity, the time-averaged shear stress introduced in **Equation 6.5** will be referred to as σ_{ta}.

The average shear stress $\bar{\sigma}$ is then simply assessed as follows:

$$\bar{\sigma} = \frac{1}{m} \sum_i \sigma_i$$

$$(6.7)$$

where m is the number of streamlines.

This weighing operation helped to consider streamline contributions to shear stress in a manner proportional to the actual flowrate through that specific point in the membrane. An analysis was first conducted in order to find the minimum number of particles to release in order to fully describe the whole fluid dynamics within the membrane. A varying number of seeds was then released in the pre-mixing region and $\bar{\sigma}$ was monitored, as displayed in **Figure 6.12.** 20 trials with varying seeds' location were run for each number of seeds (top plot), and the related CV is reported (bottom plot).
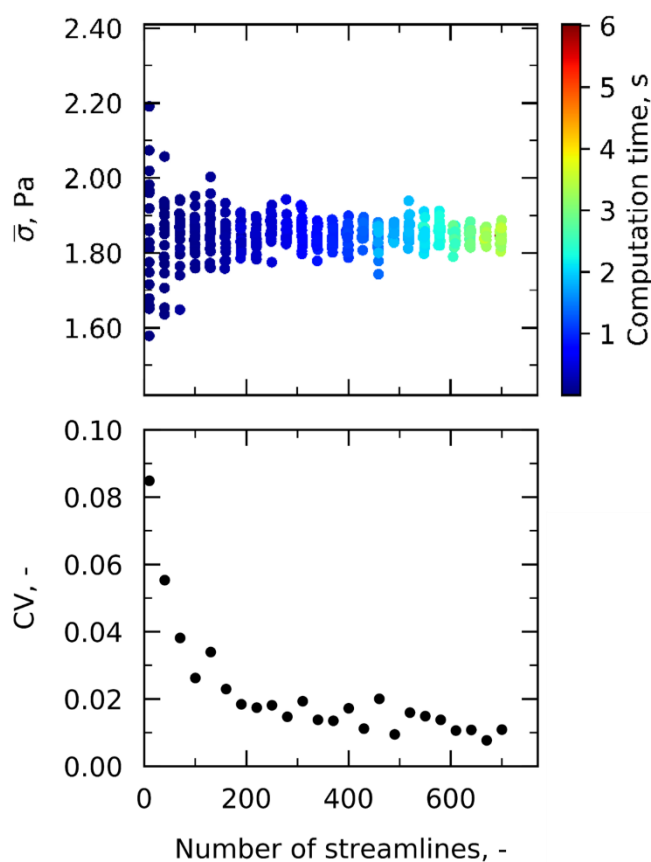

Figure 6.12 Average shear stress $\bar{\sigma}$ is displayed while varying the number of streamlines and the number of trials to ease the visualization of the analysis in the top plot. Each point in the data set is colored based on its computational time (see color scale). The relevant coefficient of variation CV are reported in the bottom plot.

The higher the number of seeds was, the lower the uncertainty span in $\bar{\sigma}$ was. From 200 seeds onwards, CV was bounded between 0 and 0.025 and, therefore, the number of seeds can be claimed sufficient to describe the fluid dynamics within the membrane. 460 streamlines were finally chosen as the increase in the seeds number did not lead to a significant increase in the computational expense. This can be observed in **Figure 6.12**, where the time to compute each point is displayed; as expected, the computation time varies linearly with increasing

number of streamlines but is still way lower than the overall simulation time (which is in the order of hours instead).

Figure 6.13 shows the distribution of the time-averaged average shear stress in the case of 460 seeds. It can be noticed that the higher shear stresses were experienced by a small portion of the solution because the majority was subjected to much lower shear stresses.
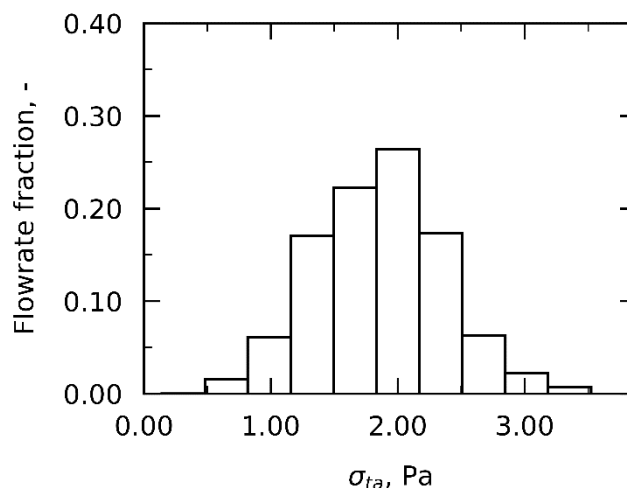

Figure 6.13 Time-averaged shear stress (σ_{ta}) distribution for the analyzed filtration unit is displayed using the flowrate fraction (w_i) normalized over w_{tot} as weight.

6.2. Industrial considerations

The previously reported analysis was then repeated for other velocities and other filtration unit's EFA, representative of potential manufacturing units, in order to investigate the relation between the inlet velocity and the resulting shear. To allow for comparison with literature data, the shear rate γ is estimated, which is simply σ/μ being incompressible fluid. The relevant results are reported in **Table 6.2** where the relevant $\bar{\gamma}$ for each Q_c is reported for comparison. Since the flow through the pores is in laminar conditions, a linear relationship is found between the inlet velocity and the resulting shear rate and is represented by α. For the three runs, the percent difference in α is below 5%.

Table 6.2 Results of the analysis for different commercial flowrates.

Q_{comm} mL min^{-1}	EFA_{comm} cm^2	V_{ms} m s^{-1}	Regime	$\bar{\gamma}$ 1/s	$\bar{\gamma}_{theo}$ 1/s	α
2500	6000	6.94×10^{-5}	Lam	1.85×10^3	2.40×10^3	26.7×10^6
1700	864	3.15×10^{-4}	Lam	8.37×10^3	1.09×10^4	26.6×10^6
2500	864	4.63×10^{-4}	Lam	1.29×10^4	1.60×10^4	27.7×10^6

A comparison with literature data was finally drawn. Some mention shear rate γ around 10,000 s^{-1} (Bee et al., 2009; Zanowiak, 2000), which is in line with our estimates for the last operating conditions considered in **Table 6.2**. These values are generally calculated with averaged and simplified approaches, assuming that the pore is a cylindrical tube with mean diameter D_{pore}:

$$\bar{\gamma} = \frac{16u_{pore}}{3D_{pore}}$$

(6.8)

where u_{pore} is calculated based on the membrane porosity ε:

$$u_{pore} = \frac{V}{\varepsilon}$$

(6.9)

Additionally, the workflow proposed in this manuscript allows for post-processing analysis to derive temporal and distribution information, which traditional equations (**Equations 6.8 and 6.9**) do not permit.

As expected (Bee et al., 2009), shear rates (and stresses) resulting from sterilizing filtration units are much higher than those resulting from other filling line operations, such as flow through tubing and fittings, whose investigation was the focus of other works from our research group. To provide some examples from these studies, shear rates of around 8×10^2 s^{-1} were found for flow in smooth tubing under turbulent conditions (flowrates around 2140 mL min^{-1} in 9.53-mm-tubing); similar values of shear rates were found for Y-fittings under the same operating conditions while higher for T-fittings (i.e., 1.2×10^3 s^{-1}). Under laminar conditions (flowrates around 180 mL min^{-1}), on the other hand, much lower shear rates were monitored (2×10^1 s^{-1}).

A final remark can be given regarding scaling approaches, which, as mentioned in the Introduction are critical to ensure representativeness between laboratory and commercial scales without over- or underestimating the system. As previously stated, they use appropriate scaling factors that account for differences in flow resistance, fouling phenomena, and flow geometries. Without exploring such macroscopic differences, however, the present work offers a formula for ensuring, at the microscopic level, that the product is exposed to the same shear stress in the laboratory compared to the commercial scale. For this particular filtration unit, being the flow laminar through the pores, the application of **Equation 6.10** can guarantee that the local shear stresses at the microscale level are preserved if the same membrane type is used in the laboratory scale unit. Indeed, the ratio between the two quantities might differ from unity if other factors besides shear stresses are considered.

$$\left(\frac{Q}{EFA}\right)_c = \left(\frac{Q}{EFA}\right)_l$$

$$(6.10)$$

6.3 Conclusion

In the present work, CFD simulations were employed to investigate the fluid dynamics within a typical sterile filtration unit. A computational replica was obtained through stochastic membrane reconstruction to meet porosity, pore size distribution, and permeability of the real filter. Shear stress analyses were conducted and the average shear exposures of the product at different operating conditions were estimated. These values were compared with those derived from traditional simplified equations; not only are the values consistent, but the present workflow allows post-processing analyses (on residence times, shear stress distributions) that traditional equations do not provide. Also, as expected, when comparing these shear stresses with those from other components of the filling line, i.e., tubing, fittings, they appeared much higher. Considerations were also drawn on the scale-down operation for the pharmaceutical industry.

The methodology we proposed can be used to explore other areas. For instance, one could evaluate particle impingement in pores during long-term processes, where aggregation phenomena are prominent, or focus on regions of high shear stress. The work could further be extended to membranes with non-uniform pore distributions or pleated membrane deformation could be studied to make the analysis even more meaningful. This research lays the foundation for future development prospects. The impact of monitored shear stress on product stability and separation efficiency could be investigated.

Chapter 7

The role of peristaltic pumping

As introduced in **Chapter 2**, different pumps can be used to move pharmaceuticals, including rotary-piston pumps, time-pressure systems, and peristaltic pumps (Karassik et al., 2001). In particular, the peristaltic (or roller) pump has a broad use in the pharmaceutical industry as it avoids contamination of the fluid by the pump (Bach et al., 2015; Klespitz and Kovács, 2014). It is a positive displacement pump that moves the product through a hose by compression and decompression (Ostadfar, 2016). Peristaltic pumps generate a pulsatile flow, whose period depends on the rollers' number and their relative speed (Zhou et al., 2014). A complete occlusion of the tubing is generally guaranteed to avoid backflow phenomena (Zhou et al., 2021). The scheme of a typical two-roller peristaltic pump is shown in **Figure 7.1**.
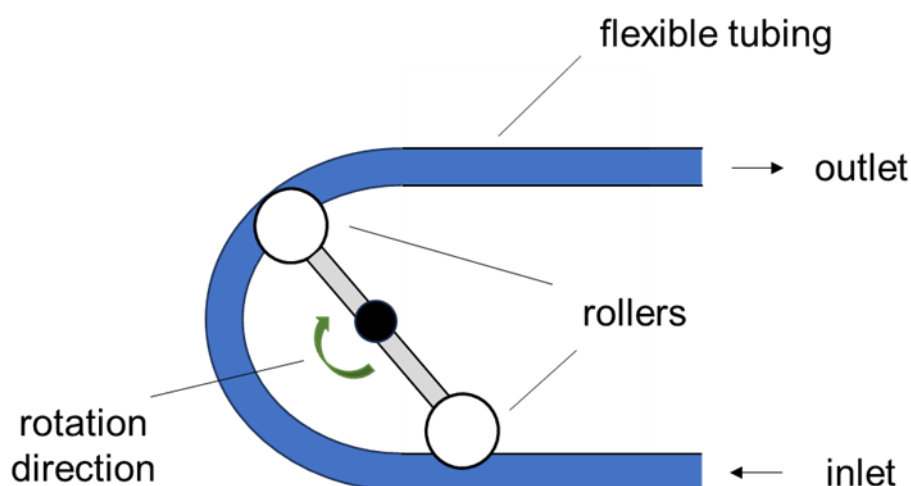

Figure 7.1 Schematic of a two-roller peristaltic pump.

Several Computational Fluid Dynamics (CFD) approaches are widely documented in the literature to study the fluid dynamics in a peristaltic pump (Gao et al., 2023; Manopoulos et al., 2020; Palmada et al., 2022).

---

* The work described in this chapter has been submitted to *Pharmaceutical Development and Technology* in "Moino, C., Albano, A., Scutellà, B., Boccardo, G., Pisano, R., 2024. Shear stresses in a filling line of parenteral products. The role of peristaltic pumping."

First, multiple steady state simulations (for different roller positions) for a peristaltic pump would allow for an easier setup and faster computing time but would not solve the actual fluid dynamics. Indeed, as the rollers move over time and generate a time-varying flow, stationary simulations do not provide the best representation of the system. A moving frame of reference and fixed frame of reference found instead quite significant development for similar applications (Al-habahbeh, 2013; Alokaily, 2017). In the moving frame of reference, the computational domain is fixed, and the coordinate system moves with the roller; therefore, the roller is fixed, and the wall moves with a velocity equal to the negative of the roller speed. Nonetheless, this method was found inadequate for the present case as it would lead, among others, to unrealistic behavior of radial velocity, i.e., maximum at the wall and not at the tubing center. On the other hand, in the fixed frame of reference, the peristaltic movement is represented by a dynamic mesh that mimics the roller motion, thus leading to a more physical representation of the system. Such an approach was used in the present study, and extensive details about the setup will be given later in the chapter. An even more meaningful representation may be achieved by considering the actual tubing deformation (Manopoulos et al., 2020; Palmada et al., 2022) but it is not the focus of the present work.

In this chapter, CFD analysis (Versteeg and Malalasekera, 2007) was employed to explore the fluid dynamics within a double roller peristaltic pump. One-way Lagrangian Particle Tracking (LPT) was adopted to track Lagrangian biological particle paths within the fluid, and shear stress statistics were carried out accounting for the time-varying shear history of each particle.

7.1 Numerical set up

The numerical approach followed is summarized in **Figure 7.2**, where the set-up, pre-processing, simulation and post-processing stages can be observed. For clarity, these steps will be discussed below in separate sections.
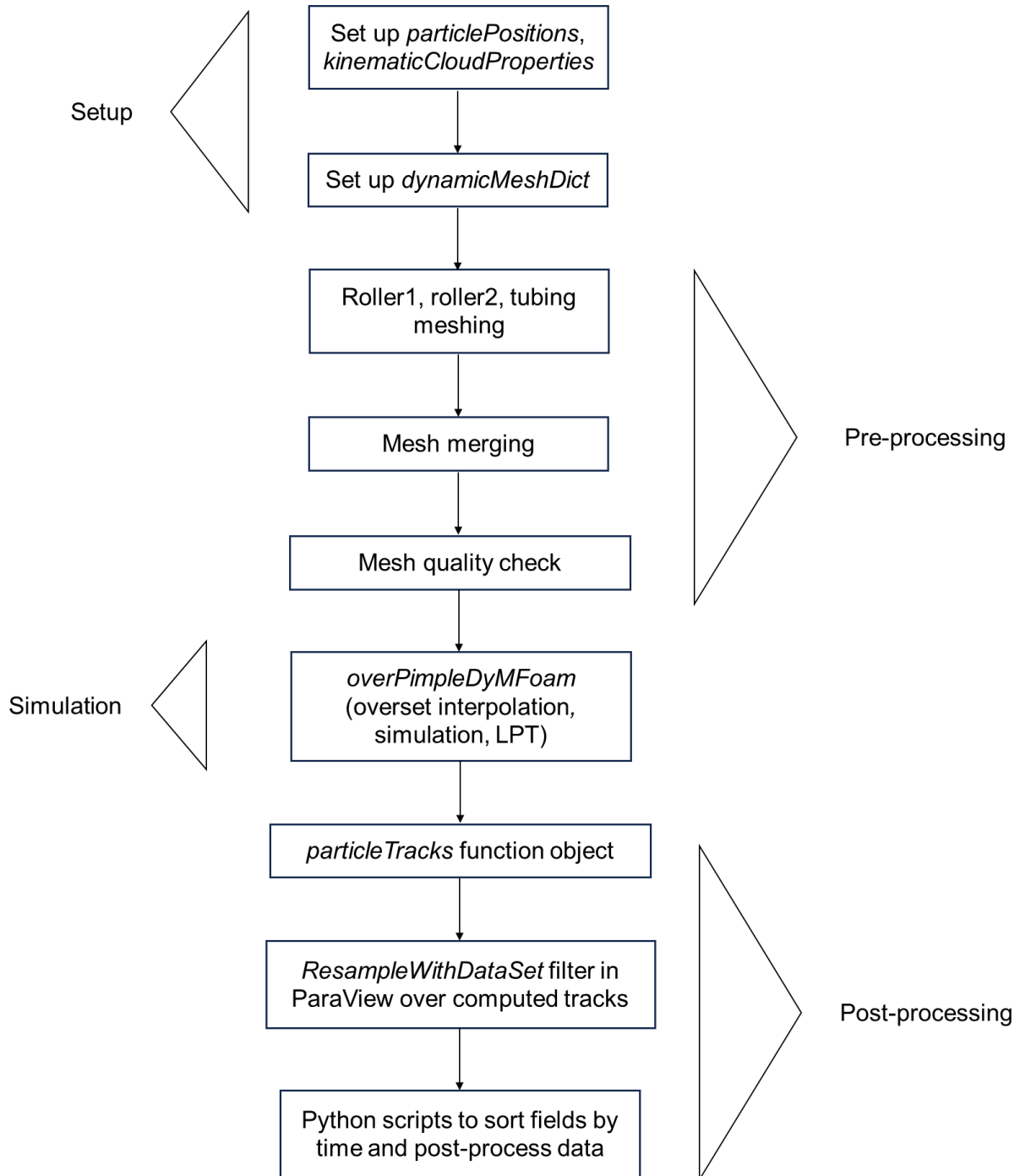
Figure 7.2 Workflow developed for fluid dynamic investigation of a peristaltic pump and associated particle tracking.

7.1.2 Setup and pre-processing

In the current study, we used CFD simulations to numerically investigate the shear stress distribution for a fluid passing through a 2D peristaltic pump. An incompressible and Newtonian fluid with water-like properties was considered. Among the framework of dynamic meshes, an overset setup (Guerrero, 2021; Mignozzi, 2022) was chosen that allows the rollers to move while the background mesh, i.e., tubing, remains fixed. In particular, the

multiSolidBodyMotionSolver was chosen, and the roller motion was defined as a rotation with angular velocity specified in rpm, origin and axis of rotation. The *blockMesh* utility available in OpenFOAM was employed for the meshing procedure, and a hexahedral structure was developed (96,000 cells). This choice resulted in a very uniform mesh, which was compatible with the overset framework. Finally, the mesh quality and topological coherence were analyzed using OpenFOAM utilities (*checkMesh*) (Guerrero, 2013). This analysis ensured that the mesh adhered to grid quality standards in terms of non-orthogonality (below 75), skewness (below 20 for boundaries and below 4 for internal mesh), and aspect ratio.

The tubing has a diameter of 9.53 mm while the roller has a diameter of 35.2 mm. The distance between the axis of the rollers is 111.2 mm. As the roller completely shrinks the tubing, a geometry with a percent opening of 1.4% was created, defined as the ratio between the opening and the total tubing diameter. This value was chosen arbitrarily small enough to be representative of the complete squeezing but also to allow some cells to be designed for numerical requirements. For the sake of clarity, the simulated geometry referred to the fluid only, and no tubing properties (and therefore deformations) were accounted for in the set-up. **Figure 7.3** shows the analyzed geometry, including boundaries and cell grids, while its size is summarized in **Table 7.1**.
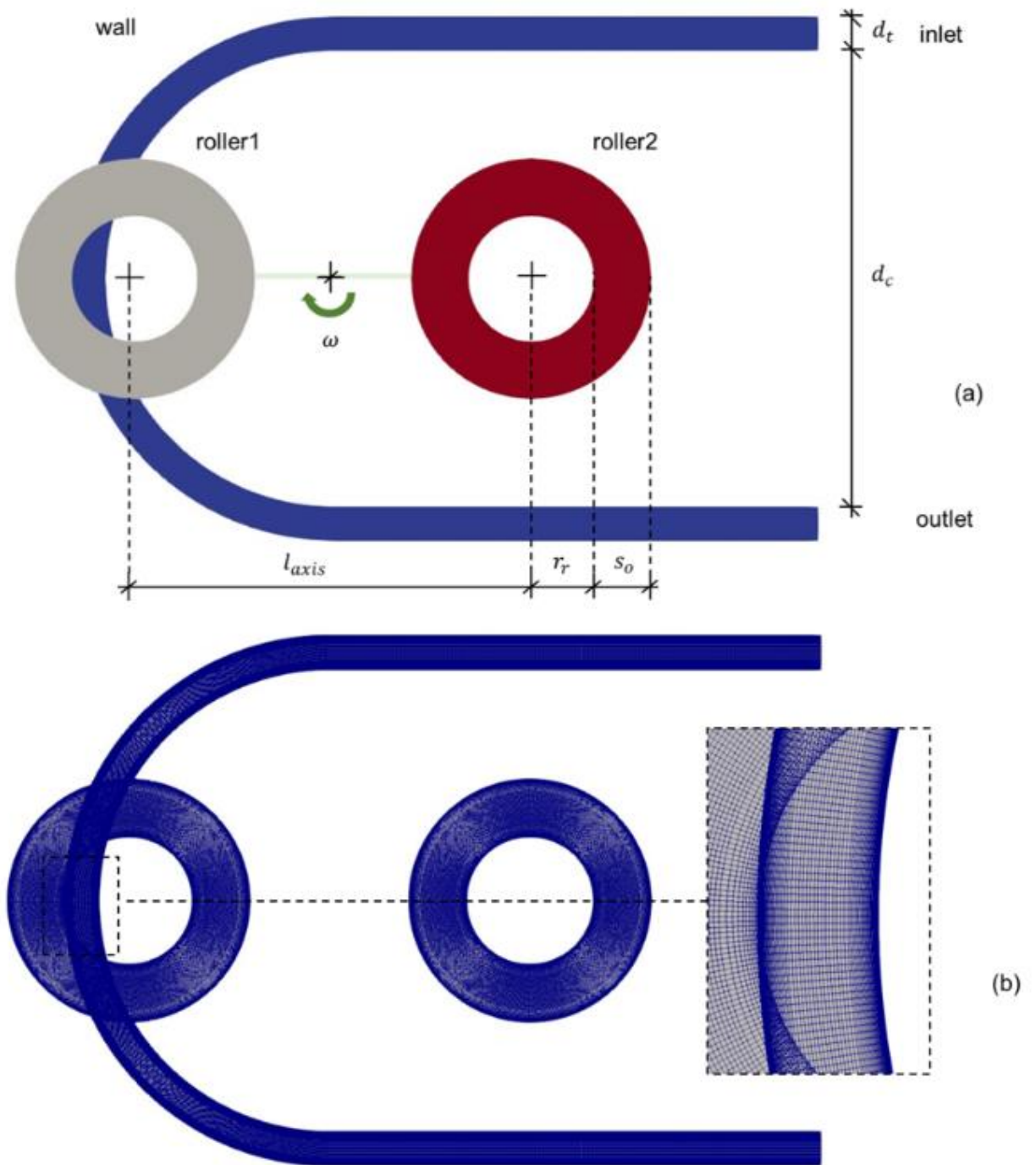
Figure 7.3 Schematic of the geometry analyzed, including boundaries (a) and mesh (b).

Table 7.1 Geometrical parameters of the pumping system.

	ω	d_c	d_t	l_{axis}	r_r	s_o
Size	20	0.1276	0.00953	0.1112	0.0176	0.016
Unit	rpm	m	m	m	m	m

The finite volume method-based open-source code OpenFOAM 1806 was used for the analysis as overset solvers are only available in the OpenFOAM version supported by ESI-OpenCFD (Guerrero, 2021). The hardware used to run the simulations is an HP workstation with eight logical processors and 16 GB of RAM. Python 3.8 was used for the post-processing of the simulations.

The CFD solution of the system requires interpolation between the overlapped regions of the meshes (Tisovska, 2019). For this reason, care was taken to the overset interpolation method and *inverseDistance* was chosen. In particular, for every time step, each cell of the background mesh and overset mesh is marked as one of the following types:

- Calculated: for such cells, the equations are solved.
- Interpolated: for such cells, the values are computed by interpolation from the nearest elements of the second domain (background elements for the overset elements, and vice versa).
- Holes: for such cells, no solution is computed.

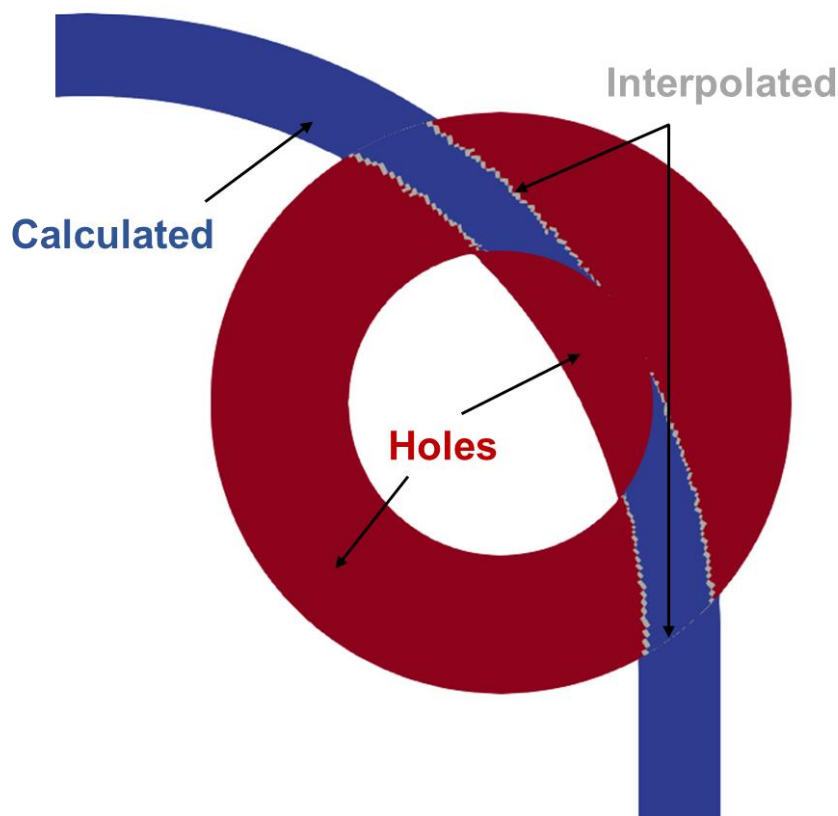An example of such interpolation is shown in **Figure 7.4**.

Figure 7.4 Instance of interpolation at time step 7.005 s.

As the patches roller1 and roller2 were moving, a moving wall boundary condition was chosen, and the same is true for the internal wall. At the external wall, on the other hand, the

no-slip condition was imposed. At the inlet and outlet patches, the total pressure was set equal to zero, to reflect the fact that the system is closed; indeed, the inlet and outlet are connected via a large fluid reservoir at constant pressure. The total pressure is therefore computed as:

$$p_0 = p + \frac{1}{2}\rho|u|^2$$

(7.1)

where p is the static pressure while $\frac{1}{2}\rho|u|^2$ expresses the dynamic pressure. The zero total pressure boundary condition adjusts the pressure p according to the changes in the velocity u, which, in turn, are driven by the rollers' motion. Then, a zero-gradient condition for pressure was applied to the wall. Fluxes at inlet and outlet boundary cell nodes were employed to calculate velocity values at the corresponding boundaries. More specifically, if fluid leaves the domain, a zero gradient condition is assigned: $\frac{\partial u_i}{\partial x_i} = 0$; vice versa, if the fluid enters the domain, the velocity is estimated from the node velocity component in the patch-normal direction.

The angular velocity of the rollers was chosen equal to 20 rpm in order to ensure a fully laminar regime (Byron Bird et al., 2002).

7.1.3 Simulation and post-processing

Four rotations of the rollers were simulated in order to focus on the last rotations and thus remove the transient effects of initial conditions. Flow solution required a computation time of 28 h per 12 s of simulation using 8 CPU cores. A fixed time step equal to 0.0005 s was chosen, which is the time taken for the roller to travel 0.06°. Instead, solutions were saved every 10 time steps (0.6°), in line with previous studies (Mulholland et al., 2005).

OverPimpleDyMFoam solver was used to solve the equations of motion, being a transient solver for incompressible fluids handling dynamic meshes. In combination with the solver, a one-way LPT was implemented to track individual particles and assess local fields through their pathlines in the given time-varying flow field carrier (Johnson and Hansen, 2005). The use of the conventional static tracers, in fact, although it found extensive use in other (and simpler) applications, was unable to detect the actual behaviors of particles. Particle tracking was therefore conducted via the function object *icoUncoupledKinematicCloud* available in OpenFOAM 1806. Gravity and coupling fluid-particle were turned off, and only drag was considered. A *manualInjection* was chosen as the injection model and size distribution (2×10^{-7}m) and Start of Injection (7 s) were defined. The random positions of the 100 particles were calculated via a Python script on a diameter of the tubing in the inlet region and saved in the 'particlePositions' file in the *constant* directory. No dispersion phenomena were considered whilst a *standardWallInteraction* model was chosen as for patch interaction model. In particular, particles interacting with a wall were not expected to disappear or stick to the patch but rather bounce, and therefore, the option *rebound* was selected, which predicts the new particle trajectory based on surface material and impinging particles. For the sake of

clarity, other and simpler approaches could have been used to track massless particles, i.e., through *particleTracer* and *temporalParticlesToPathlines* filters available in ParaView, but the inability to define the behavior of particles when in contact with a surface (rebound, stick, escape) made it unsuitable for the current case.

The function object *foamToVTK* was then run in the framework of OpenFOAM 1912 to convert data from its native format to the Visualization Toolkit format, and therefore allow visualization in ParaView. Once the particle positions were available for each time step, the function object *particleTracks* was run in OpenFOAM 2112, which generated a file of particle tracks from the computed kinematic cloud. Then, the filter *Resample With Dataset* available in ParaView was employed to sample the data on Input (computed flow field) on the Source (particle tracks). Such data was exported in .csv format for each investigated time step. This approach was pivotal to capture the individual particle's actual fields as the time evolved, since the carrier flow field changed over time. A Python script was written to extract particle fields at each time step at the relevant positions within the extracted arrays. By doing so, time-varying flow fields for all the particles through their pathlines were collected. The trapezoidal rule was then employed to evaluate a time-averaged shear stress σ_{ta} across the pathline i:

$$\sigma_{ta,i} = \frac{1}{\tau_i} \int_o^{\tau_i} \sigma_i(t) dt$$

(7.2)

where t is the time step and τ is the overall particle residence time.

Similarly, the time-averaged velocity was assessed for each pathline. This was used to calculate the average shear stress by weighing each pathline's time-averaged shear stress on its time-averaged velocity. Drawing on earlier works from our research group, **Equations 7.3** and **7.4** were used.

$$\bar{\sigma}_i = \sum_i \left(\left(\frac{1}{\tau_i} \int_o^{\tau_i} \sigma_i(t) dt \right) \cdot \frac{w_i}{w_{tot}} \right)$$

(7.3)

where w_i is the local weight and is calculated as follows:

$$w_i = A_i \frac{1}{\tau_i} \int_0^{\tau_i} u_i(t) \, dt$$

(7.4)

with $u_i(t)$ being the velocity at the relevant time step, i the streamline index and A the pathline area of influence.

The final average shear stress is then simply calculated as:

$$\bar{\sigma} = \frac{1}{m}\sum_i \bar{\sigma}_i$$

(7.5)

All the mentioned function object utilities were already present in the framework of OpenFOAM 1806. For the shear rate analysis, instead, a new function object was written in C++ and further compiled (Sankar Raju. N, 2017). More information on the shear rate is provided in Appendix A3.

7.2 Results

7.2.1 Velocity analysis

The outlet average velocity was the subject of the initial investigation. Under the given settings, the 2D average velocity in the outlet patch was monitored with time. In particular, it was calculated in ParaView as the integral over the cells of the 2D cross-section. This resulted in a periodic trend, as visible in **Figure 7.5**, which is consistent with previously reported studies (Manopoulos et al., 2020). After an initial transient time (due to initial conditions and therefore excluded from this discussion), the periodic pattern is repeated every 180°. When the roller starts detaching from the tubing (at around 300°), the velocity (and thus mass flowrate) begins to drop, reaching a minimum value of around 0. As can be noted, the velocity never goes negative and, therefore, no backflow phenomenon occurs, which highlights the importance of the complete tubing occlusion.
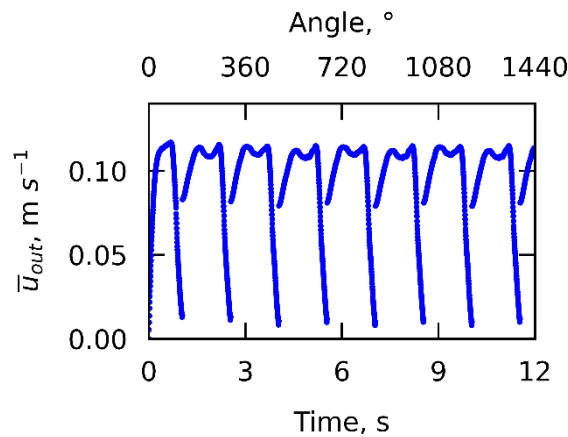

Figure 7.5 Average velocity at the outlet.

The average value of the flowrate can be estimated by integrating the velocity over time, using the trapezoidal function, as previously mentioned in **Section 3.2**. A value of 0.095 m s^{-1} was found considering one complete rollers' rotation (840°-1200°). To check whether the

velocity was realistic, it was compared with a value collected from the literature for a system with a relatively similar set up (Gao et al., 2023) and a positive match was found.

7.2.2 Lagrangian particles' analysis

A peristaltic pump represents a complex system whose modeling and subsequent trajectories analysis are not trivial. Not only the mesh changes with time, but that originates a time-varying carrier flow field, which makes the investigation through steady-state streamlines nonphysical nor informative. For such reasons, a new workflow was developed as described in detail in previous **Section 7.1**.

A Python script was written to plot the actual fields of the particles as a result of the time-varying flow carrier. **Figure 7.6** shows the shear stress evolution for a particle at three time steps, and the position of the rollers is also visible. For the sake of clarity, particles were instantaneously released at 7 s (refer to **Figure 7.5**), so that the flow field was well-developed; rollers move counterclockwise. A non-constant shear stress profile can be observed, resulting from the pulsatile nature of the flow.
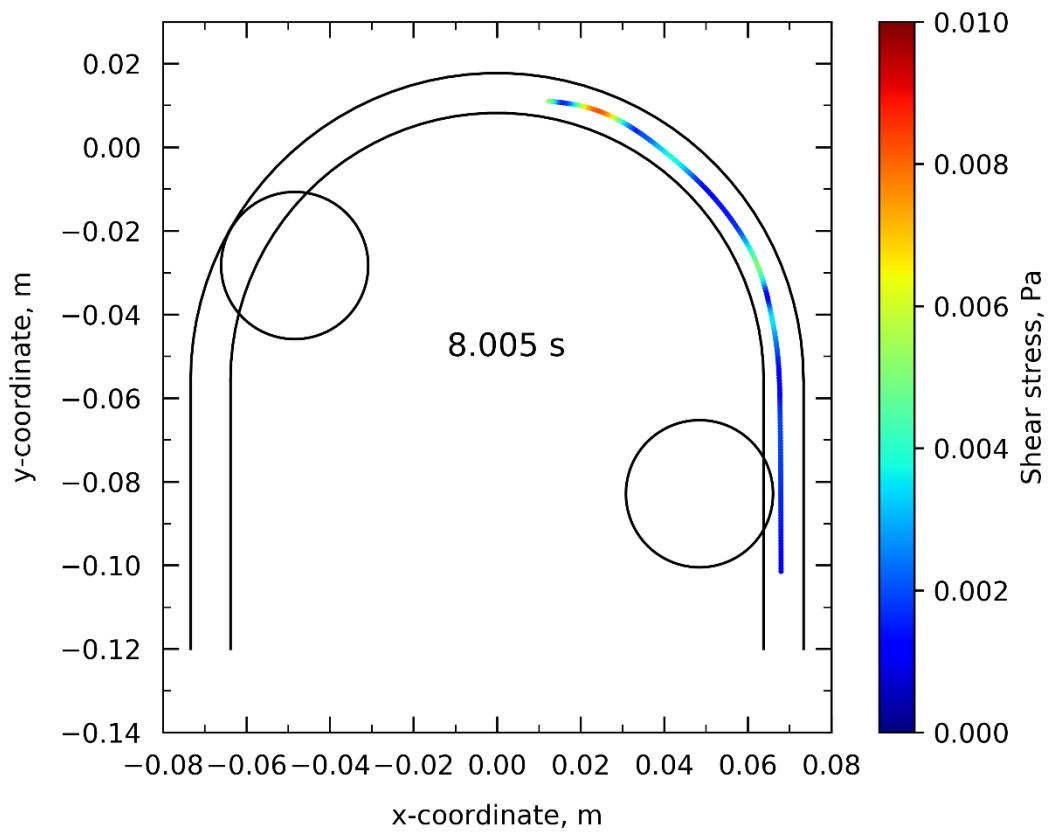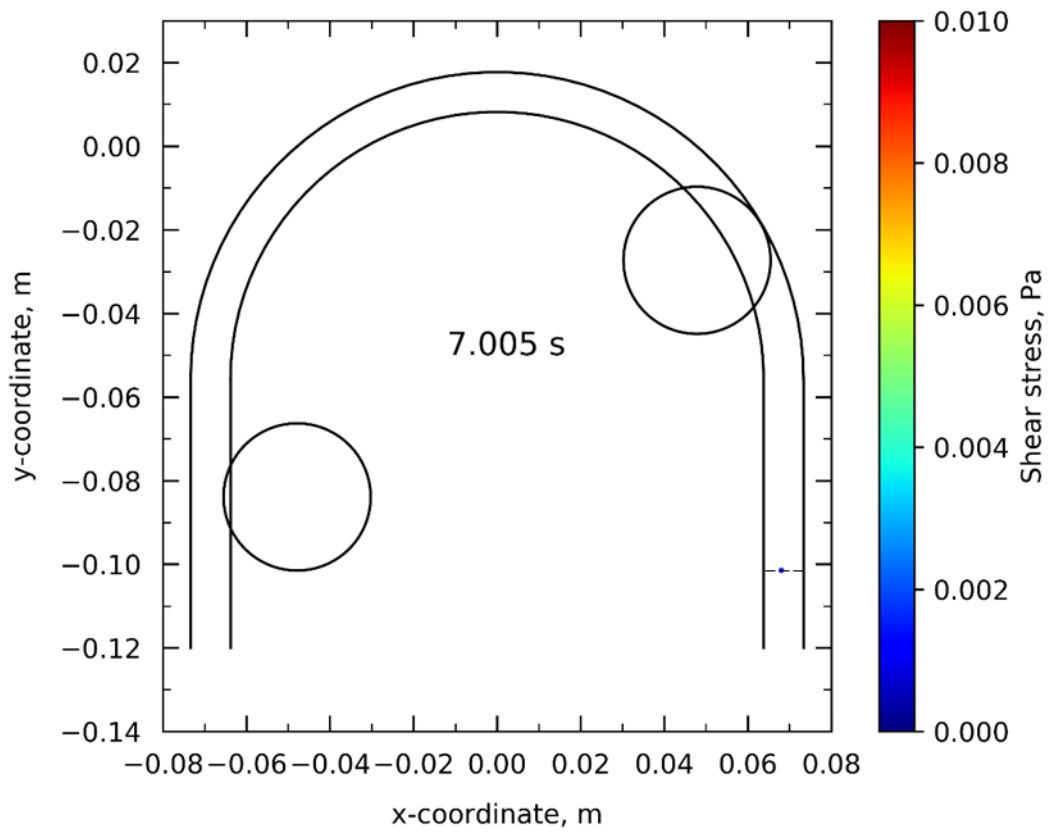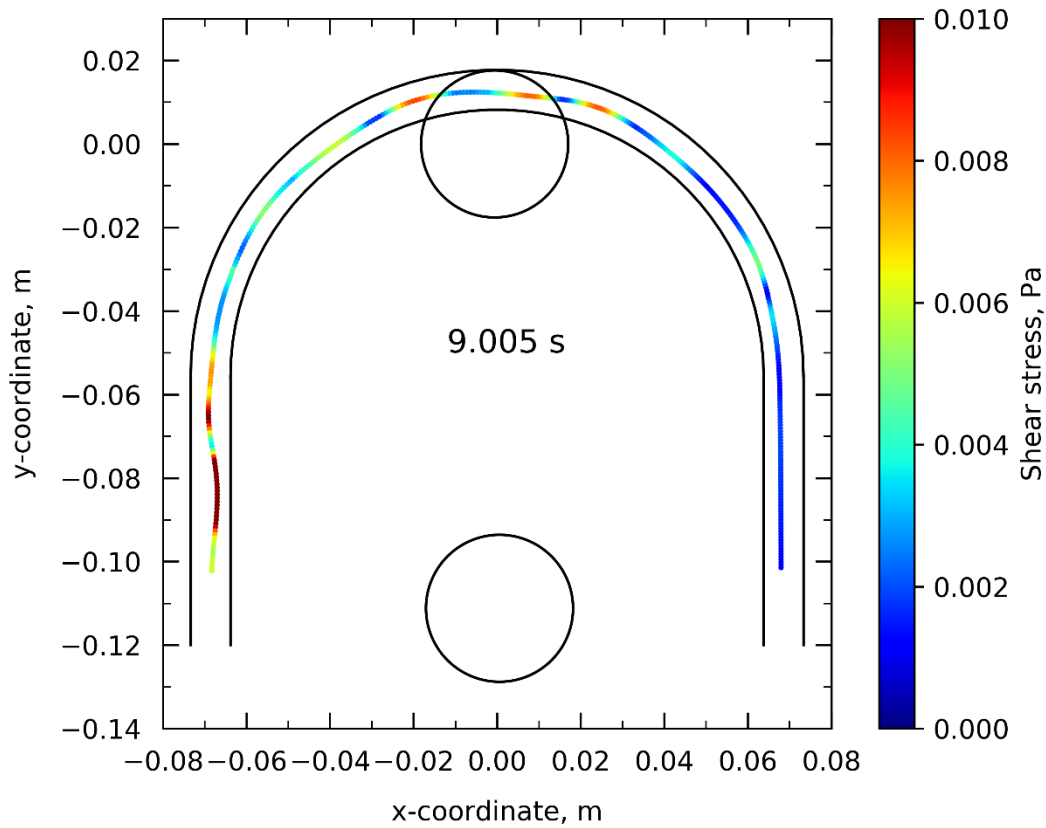
Figure 7.6 Particle pathline (and relevant temporal shear stress evolution) at different time steps. The dashed line in the figure at 7.005 s corresponds to the diameter where particles are released.

It should be noted that a nonphysical behavior was noticed for some of the slower particles. When the roller approached them, they ended up near the roller because of their low speed. However, instead of being pushed, they would end up behind the roller and remain still there. Then, once the roller passes over them, they would resume their trajectory. The cell type assignment, in fact, as shown in **Figure 7.4**, is not perfect as it is strictly dependent on mesh refinement. During the interpolation, some cells close to the wall are erroneously marked as 'holes'; therefore, when a particle enters such a cell, no equation is computed and the roller consequently overtakes the particle. Various meshing techniques were tested aiming at increasing the mesh resolution and hence decreasing the interpolation error. The proposed mesh is a compromise between solution accuracy against computation time.

To overcome the unrealistic behavior resulting from the interpolation, the contribution of particles once they went over the roller was neglected, because it is impact a small sample of the overall particles across the last part of their trajectory.

For the investigations provided in the next paragraph, a defined Region of Interest (ROI) was selected. This ROI included any part where roller motion affected fluid flow (in all time steps considered).

100

Shear stress distribution

As a starting point, the time-varying shear stress histories along four (random) particle pathlines is examined in **Figure 7.7** as a function of the distance traveled by the particle. Given their initial release position, an explanation of their behavior is hereafter addressed. The first particle (upper left panel) started from around the center of the tubing; it experiences low shear stresses, but it travels along the tubing very fast; for this reason, after a little more than 2.5 s it exits the ROI. On the other hand, the second particle under investigation (upper right panel) started from the near-wall region. It travels slowly through the tubing but experiences higher shear stresses than the first particle (since it is closer to the wall where the velocity gradients are the steepest); however, it ends up in the 'holes' region mentioned above and therefore, its traveled distance is not followed from that point onwards. Finally, the third and fourth particles behave quite similarly (lower left and right panels, respectively). They are released around the mid-point of the outer half-diameter of the tubing. They are exposed to higher local shear stresses than the first particle (upper left panel) since they are closer to the wall and do not travel as fast (they get out of the ROI after less than 3 s).
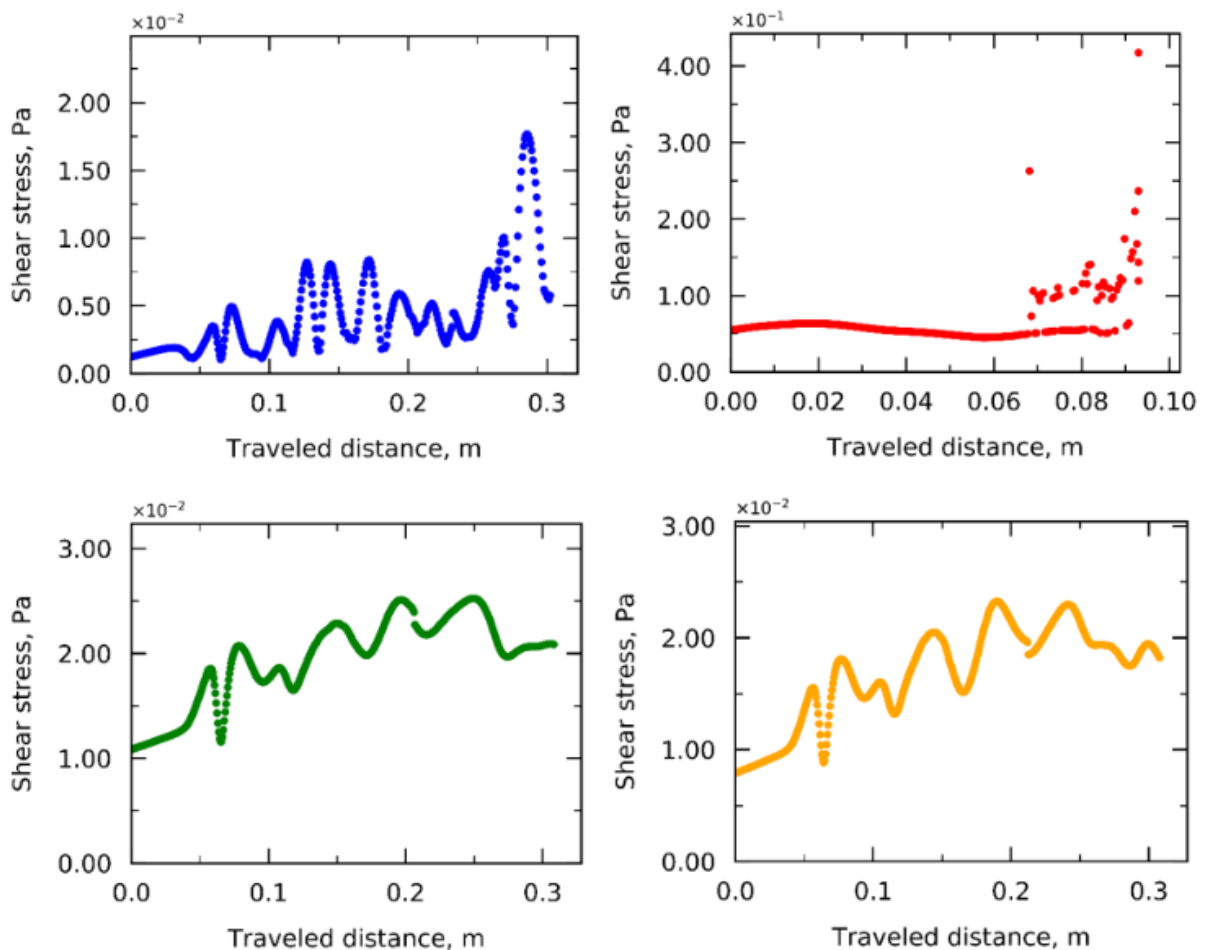

Figure 7.7 Shear stress histories across four (random) pathlines. The scales along the x- and y-axes of the four plots are different because they are peculiar to the individual particle they depict.

For clarity, the pathlines of the presented particles are hereafter displayed.
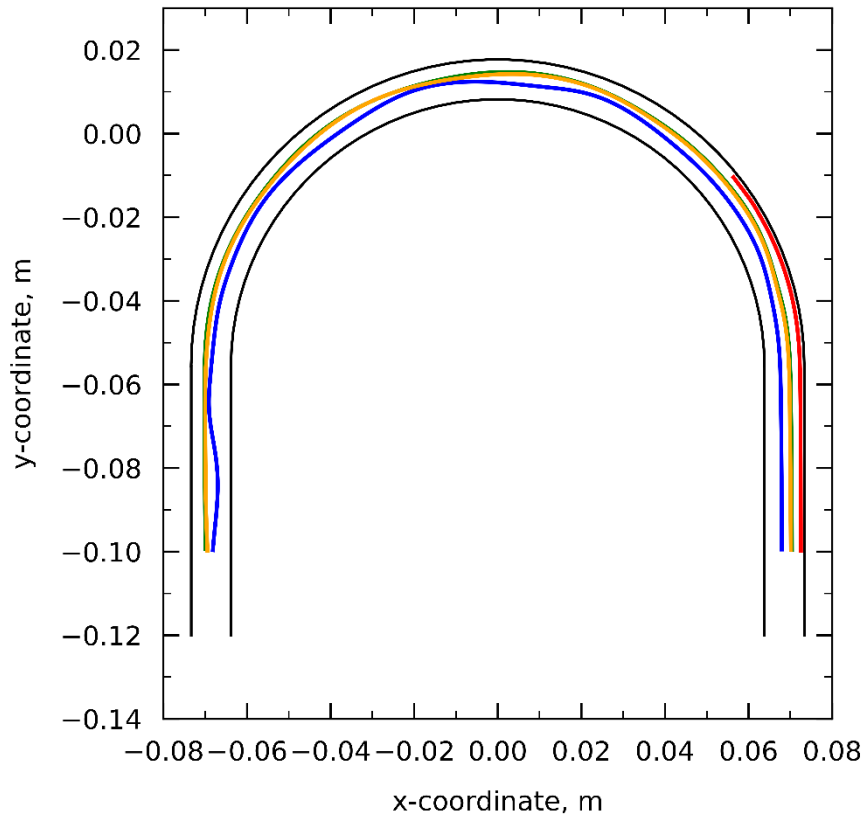

Figure 7.8 Pathlines of the particles whose shear stress distribution is shown (in the same color) in **Figure 7.7**.

Nonetheless, a more representative picture of the shear history is estimated by using an averaging operation. For such reason, using the equations previously described, the average shear stress was calculated, and a representation in terms of frequency histogram is provided in **Figure 7.9**, in which the number of bins was chosen following Sturges' rule (Scott, 2009).
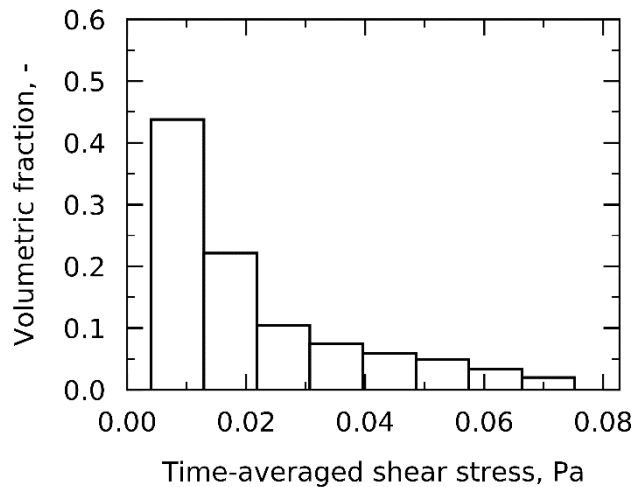

Figure 7.9 Time-averaged shear stress weighed on volumetric flowrate fraction.

Under the investigated conditions, the product is exposed to moderate shear stresses, also given the relatively low velocity considered. The present research combines a promising workflow for biological particle tracking in peristaltic pumps and estimating the average shear stress through previously derived equations. The benefit of using this equation is that it is possible to compare the extent of shear stress in the various components analyzed (tubing, fittings, sterilizing filtration). As a matter of fact, it is strictly dependent on the operating conditions chosen, e.g., inlet velocity and regime considered. Nonetheless, it should be noted that the present study is based on a 2D system while the other cases our research group analyzed were 3D-based and, therefore, scaling factors should be calculated to account for the change in dimensionality. Nevertheless, a point of comparison was made by limiting the ROI to the straight inlet flow region and, therefore, considering particle pathlines unaffected by the roller motions in the initial time steps; the calculated average shear stress values are shown in **Table 7.2**.

Table 7.2 Comparison between shear stress in peristaltic pump and straight part of the tubing.

System	$\overline{u}_{out}$, m s^{-1}	$\overline{\sigma}$, Pa
Pump	0.095	0.021
Tubing	0.095	0.015

As expected, on average, the shear stress in the pump is within the same order of magnitude as that in the tubing, whilst the geometric configuration is different. The two systems, nonetheless, differ in the shear stress peaks due to the tubing squeezing, which occurs for a short time. Therefore, knowing the time required for a particle to undergo degradation under the exerted shear stress would be helpful, but that would be another story. As mentioned in **Chapter 2**, the precise role of shear stress on the stability of biotherapeutics has not yet been clarified. According to the latest studies, shear stress alone cannot drive product degradation. Still, when combined with interfacial stress, it promotes product turnover in areas in contact with the interface, thus further accelerating interface-induced instability. However, exploring shear stress distribution is critical as a first step for wider experimental investigation in this important yet controversial landscape.

7.3 Conclusion

The present work employed CFD simulations to investigate the fluid dynamics within a peristaltic pump. First, the geometry was modeled using an overset dynamic mesh in the framework of OpenFOAM. Then, an innovative workflow was developed to follow Lagrangian particles through the flow. In contrast, the flow field was solved, the particle time-varying pathlines were assessed and the average shear stress was estimated by accounting for particle shear history. For the case studied, it was observed that, beside obvious peaks, the average shear stress is in the same order of magnitude of that experienced by the product in a 2D tubing. The following approach paves the way for future analysis, i.e., turbulent conditions, 3D modeling. In a broader perspective, the same post-processing approach can be employed to analyze the shear stress distribution for other components of the line where the fluid flow and

mesh vary with time, i.e., the mixing tank modeled within the dynamic mesh framework. From an experimental point of view, on the other hand, laboratory tests could be conducted to explore the impact of different pump speeds on the product while maintaining the same interfacial exposure. Given the magnitude of numerically computable shear stress as we have proposed, one could advocate a deconvolution of shear impact with respect to interfacial stress.

Chapter 8

Conclusions

This work presented some novel strategies to investigate the fluid dynamics within some standard filling operations, with particular emphasis on the extent of shear stress exposure to the product. The work not only demonstrated the ability of CFD modeling to aid pharmaceutical engineering operation, but also exhibited the potential for future application in other engineering domains. The study started out as an effort to address a few important issues that have long been present in the industrial pharmaceutical environment. These research questions, posed in the Introduction, are finally attempted to be handled following the thorough exploration of fluid dynamics that is supported by experimental data that was gathered in the literature.

1. How does the present work fit into the current state of the art? How does it provide aids for industrial practices?

As explained in **Chapter 2**, filling lines expose the product to high hydrodynamic stresses, e.g., shear stress. Product stability is critical since the product is intended for parenteral use and thus the occurrence of side effects is highly undesirable. Although not universally recognized, shear stresses are believed to play a role in protein-based product degradation, especially when synergistically associated with high interfacial exposure. For this reason, knowing the magnitude of shear stress is the first step in further investigating the problem experimentally. Several authors have studied shear stress in individual filling line components, but this comprehensive work analyzing the shear stress exposure in different line components through the definition of equations for potentially universal use is, to the best of our knowledge, the first of its kind.

In this framework, CFD analyses were leveraged to probe the fluid dynamic stresses that the product experiences during different steps of the filling line. Downstream of this exploration, some numerically validated scale-down approaches were proposed. Support was provided to the company's Manufacturing Sciences & Technology (MSAT) department. Through the use of these models, the number of experiments conducted was greatly reduced. These scale-down equations were derived so that it is possible to accurately replicate in the laboratory the same shear stress conditions that the product would experience at the commercial scale.

2. Is it possible to derive modeling-based scale-down approaches which ensure representativeness between laboratory and commercial scales?

It is indeed possible to derive scale-down equations that preserve representativeness between the two scales. The key issue is to figure out which property should be maintained between the two scales. As explained in **Chapter 1**, there are several ways to scale down a process, ensuring geometric, kinematic, or dynamic similarity. In this specific case, looking at the focus of the project, it was decided to consider precisely shear stress exposure as a scaling parameter.

As explained in **Chapter 1** (and further investigated in **Chapter 4**), current methods to scale commercial processes are traditionally based on design of experiments or worst-case scenario. At the laboratory scale, the same product as at the commercial scale is employed, whereas the characteristic size of the operating unit is diminished so as to reduce product consumption. Traditionally, GSK did not resort to mathematical modeling to scale down pharmaceutical operations, but experiments were simply planned in such a way as to cover all possible operating conditions encountered industrially. This of course involved a high number of experiments and thus wasted time and money, particularly given that pharmaceuticals are typically very expensive. Furthermore, it was not possible to make predictions in the case of deviation from standard conditions of the filling lines. For all these reasons, scale-down methods based on mathematical modeling became necessary and laid the basis for the present doctoral work.

To clarify, scale-down strategies were only proposed for two out of the four unit operations studied, i.e., tubing and sterilizing filtration. In the case of fittings, indeed, no scale-down approach is needed as they are generally not used at the laboratory scale: the investigation served the purpose of enriching the range of fluid dynamics conditions which were considered in the case of tubing, and consolidating the obtained results. Concerning the pumps, no equations were derived as those for tubing still hold valid.

3. What is the role of exposure time in (potential) shear stress-induced damage? Should it be taken into account when defining the scale-down strategy? If yes, how?

Although widely documented and studied in the literature, the role of exposure time in shear stress-induced damage is not well understood. As reported in **Chapter 2**, earlier experiments found that the higher the exposure time the higher the product degradation, even given a small shear stress. On the other hand, recent works blamed the interfacial stress as the main culprit of product degradation, with the shear stress cooperatively accelerating the degradation by promoting product turnover in areas in contact with interfaces, where proteins are proven to adsorb and aggregate under specific conditions. Given this new perspective, exposure time seems to play a pivotal role, by prolonging the time the product experiences a defined shear.

For these reasons, considering the exposure time in the definition of the scale-down strategy is critical. To provide an example, in the case of the tubing scenario, as reported in **Chapter 4**, the length of the tubing to be used for laboratory testing was precisely chosen in order to preserve the shear stress exposure time that the pharmaceutical experienced at the commercial scale.

In addition, the exposure time varies significantly from operation to operation; if mixing exposes the product to low shear stresses for a long time, filtration can exert high shear stresses for a very short time. For the same shear stress, therefore, not only the stress exposure time is important but also the geometric configuration. To provide an example, it has been estimated that the shear stress in the pump is of the same order of magnitude as the shear in the tubing under the same operating conditions; however, the different geometric configuration results in the product in the pump being exposed to greater interfaces, which can drive product degradation, then accelerated by the shear stress. Knowing the minimum time to degrade a protein in the face of mechanical stress could help to discern the role of shear, but the exploration of stress-induced degradation phenomena has traditionally been very complicated.

In particular, separating shear forces from other denaturing factors, mainly the solid-liquid and air-liquid interfaces, poses unique challenges because it is difficult to quantify shear stress under interface-free conditions. Shear stress threshold values depend not only on the method of determination, i.e., the flow conditions in the adopted device, but also on the evaluated product.

4. Is the proposed shear stress estimation strategy extendable to other components of the line? Are comparisons within equipment possible?

A key advantage of using the proposed strategy to quantify shear stress is that it can be extended to other components of the filling line to allow comparison. The strategy begins by considering the local (or temporal) variation in shear stress through information provided by the streamlines (or pathlines) of biological particles within the fluid. In this way, the actual shear history experienced by the product can be accounted for. In addition, the shear stress contributions are weighed on their volume fractions to account for the actual flowrate. This operation is equivalent to considering the product particles proportional to the actual flowrate.

Given the same operating units, comparison can be drawn to find out the operation which stresses the product the most. Nonetheless, care must be taken in the interpretation of the results. As mentioned in the previous discussion (answer 3.), shear stress alone seems unlikely to drive product degradation; rather, its cooperation with interfacial stress represents the triggering phenomenon. Therefore, a high shear stress is not necessarily associated with higher product impact, as other factors should be considered (presence of interfaces, product properties, effect of exposure time). This work represents the first step for subsequent experimental analysis. It is the first of its kind to propose a universal method for estimating shear in various operations taking into account shear history and flowrates involved. It facilitates scale-down operations using modeling-based methods while reducing product consumption and related costs.

5. Which unit operation of the filling line exposes the product to the maximum shear stress? How do you move from a single block process view to an overview along the entire process line?

Given the operating conditions considered, CFD modeling suggested that the filtration exposes the product to the highest shear stresses and this found high consistency with literature data. Average shear rate values of 10^4 s^{-1} were estimated for standard sterilizing filter, which are significantly higher than those calculated for flow through tubing, fittings, and pumping. They result from the fluid passage through very narrow pores (in the order of 0.22 μm), which makes the velocity gradients increase.

Not only do shear stresses vary from one operation to the other, but also as a function of operating conditions, i.e., inlet velocity and flow regime. Along the line, the product is exposed to shear stresses of varying magnitude and, downstream of the literature review proposed in **Chapter 2** and the numerical investigations proposed in **Chapters 4**, **5**, **6** and **7**, we believe that a cumulative "damage factor" is not an optimal indicator of (potential) shear-induced degradation. Indeed, the shear stress in each unit operation must be considered individually, along with the relative geometric configuration and time of exposure to shear stress.

6.   What are the future steps of this work, especially from an experimental perspective?

Given the premises made in the previous points of discussion, we foster detailed experimental campaigns to shed more light into this well studied yet still controversial realm. More targeted investigation of each operating unit should be conducted to find the actual relative contribution of interfacial and shear stresses on protein degradation; indeed, it is difficult to deconvolute these two factors both experimentally and *in silico*. In particular, we advocate technological advancements in designing lab chips for shear stress tests under interface-free conditions. Finally, molecular dynamics techniques could come to the rescue to help study protein behavior upon shear.

References

Affandy, A., 2013. Fundamental studies of the sterile filtration of large plasmid DNA. University College London.

Agostini, E., 2023. Fluid dynamics and mass transfer in porous media. Politecnico di Torino.

Agostini, E., Boccardo, G., Marchisio, D., 2022. An open-source workflow for open-cell foams modelling: Geometry generation and CFD simulations for momentum and mass transport. Chem. Eng. Sci. 255, 117583. https://doi.org/10.1016/j.ces.2022.117583

Aimar, P., Bacchin, P., 2010. Slow colloidal aggregation and membrane fouling. J. Memb. Sci. 360, 70–76. https://doi.org/10.1016/j.memsci.2010.05.001

Al-Chi, A., Gupta, M.R., Stagner, W.C., 2013. Integrated Pharmaceutics. Wiley & Sons, Inc., Hoboken, New Jersey, Hoboken, New Jersey, NJ, USA.

Al-habahbeh, A.A., 2013. Simulations of newtonian and non-newtonian flows in deformable tubes. Open Access Dissertation, Michigan Technological University. https://doi.org/10.37099/mtu.dc.etds/593

Allmendinger, A., Fischer, S., Huwyler, J., Mahler, H.C., Schwarb, E., Zarraga, I.E., Mueller, R., 2014. Rheological characterization and injection forces of concentrated protein formulations: An alternative predictive model for non-Newtonian solutions. Eur. J. Pharm. Biopharm. 87, 318–328. https://doi.org/10.1016/j.ejpb.2014.01.009

Allmendinger, A., Mueller, R., Huwyler, J., Mahler, H.C., Fischer, S., 2015. Sterile filtration of highly concentrated protein formulations: impact of protein concentration, formulation composition, and filter material. J. Pharm. Sci. 104, 3319–3329. https://doi.org/10.1002/jps.24561

Alokaily, S., 2017. Modeling and simulation of the peristaltic flow of newtonian and non newtonian fluids with application to the human body. Open Access Dissertation, Michigan Technological University, https://doi.org/10.37099/mtu.dc.etds/593

Anderson, J., 2019. A Guide To Wall Shear Stress Measurement - #2 - Indirect Measurements [WWW Document]. URL https://thinkic2.com/blog/a-guide-to-wall-shear-stress-measurement-2-indirect-measurements/

Arsiccio, A., McCarty, J., Pisano, R., Shea, J.E., 2020. Heightened cold-denaturation of proteins at the ice-water interface. J. Am. Chem. Soc. 142, 5722–5730. https://doi.org/10.1021/jacs.9b13454

Arsiccio, A., McCarty, J., Pisano, R., Shea, J.E., 2018. Effect of surfactants on surface-induced denaturation of Proteins: evidence of an orientation-dependent mechanism. J. Phys. Chem. B 122, 11390–11399. https://doi.org/10.1021/acs.jpcb.8b07368

Arsiccio, A., Pisano, R., 2020. The ice-water interface and protein stability: A review. J. Pharm. Sci. 109, 2116–2130. https://doi.org/10.1016/j.xphs.2020.03.022

Ashton, L., Dusting, J., Imomoh, E., Balabani, S., Blanch, E.W., 2009. Shear-induced unfolding of lysozyme monitored in situ. Biophys. J. 96, 4231–4236. https://doi.org/10.1016/j.bpj.2009.02.024

Atkinson, K.E., 1989. An Introduction to Numerical Analysis, Second. ed. John Wildey & Sons, Canada. https://doi.org/10.1080/00401706.1966.10490427

Ayachit, U., 2018. The ParaView Guide: A Parallel Visualization Application. Kitware Inc 274.

Babinchak, W.M., Surewicz, W.K., 2020. Liquid–Liquid Phase Separation and Its Mechanistic Role in Pathological Protein Aggregation. J. Mol. Biol. 432, 1910–1925. https://doi.org/10.1016/j.jmb.2020.03.004

Babnik, S., Erklavelc-Zajec, V., Oblak, B., Pohar, A., 2020. A review of computational fluid dynamics (CFD) simulations of mixing in the pharmaceutical industry. Biomed. J. Sci. Tech. Res. 27, 20732–20736. https://doi.org/10.26717/bjstr.2020.27.004494

Bach, D., Schmich, F., Masselter, T., Speck, T., 2015. A review of selected pumping systems in nature and engineering - Potential biomimetic concepts for improving displacement pumps and pulsation damping. Bioinspir and Biomim 10. https://doi.org/10.1088/1748-3190/10/5/051001

Bachmann, M.F., Jennings, G.T., 2010. Vaccine delivery: A matter of size, geometry, kinetics and molecular patterns. Nat. Rev. Immunol. 10, 787–796. https://doi.org/10.1038/nri2868

Bachmat, Y., Bear, J., 1986. Macroscopic modelling of transport phenomena in porous media. 1: The continuum approach. Transp. Porous Media 1, 213–240. https://doi.org/10.1007/BF00238181

Baruah, G.L., Venkiteshwaran, A., Belfort, G., 2005. Global model for optimizing crossflow microfiltration and ultrafiltration processes: A new predictive and design tool. Biotechnol. Prog. 21, 1013–1025. https://doi.org/10.1021/bp050184r

Battiato, I., Ferrero V, P.T., O' Malley, D., Miller, C.T., Takhar, P.S., Valdés-Parada, F.J., Wood, B.D., 2019. Theory and Applications of Macroscale Models in Porous Media. Transp. Porous Media 130, 5–76. https://doi.org/10.1007/s11242-019-01282-2

Bausch, U., 2008. Impact of filling processes on protein solutions. Universität Basel.

Bee, J.S., Stevenson, J.L., Mehta, B., Svitel, J., Pollastrini, J., Platz, R., Freund, E., Carpenter, J.F., Randolph, T.W., 2009. Response of a concentrated monoclonal antibody formulation to high shear. Biotechnol. Bioeng. 103, 936–943. https://doi.org/10.1002/bit.22336

Bekard, I.B., Asimakis, P., Bertolini, J., Dunstan, D.E., 2011a. The effects of shear flow on protein structure and function. Biopolymers 95, 733–745. https://doi.org/10.1002/bip.21646

Bekard, I.B., Barnham, K.J., White, L.R., Dunstan, D.E., 2011b. α-Helix unfolding in simple shear flow. Soft Matter 7, 203–210. https://doi.org/10.1039/c0sm00692k

Bekard, I.B., Dunstan, D.E., 2009. Shear-Induced deformation of bovine insulin in couette flow. J. Phys. Chem. B 113, 8453–8457. https://doi.org/10.1021/jp903522e

Biddlecombe, J.G., Craig, A. V., Zhang, H., Uddin, S., Mulot, S., Fish, B.C., Bracewell, D.G., 2007. Determining antibody stability: Creation of solid - Liquid interfacial effects within a high shear environment. Biotechnol. Prog. 23, 1218–1222. https://doi.org/10.1021/bp0701261

Boccardo, G., Marchisio, D.L., Sethi, R., 2014. Microscale simulation of particle deposition in porous media. J. Colloid Interface Sci. 417, 227–237. https://doi.org/10.1016/j.jcis.2013.11.007

Bódalo, A., Gómez, J.L., Gómez, E., Máximo, M.F., Montiel, M.C., 2004. Study of L-aminoacylase deactivation in an ultrafiltration membrane reactor. Enzyme Microb. Technol. 35, 261–266. https://doi.org/10.1016/j.enzmictec.2004.05.003

Brange, J., Havelund, S., 1983. Insulin pumps and insulin quality. Acta Med. Scand. 213, 135–138.

Brown, A.I., Levison, P., Titchener-Hooker, N.J., Lye, G.J., 2009. Membrane pleating effects in 0.2 μm rated microfiltration cartridges. J. Memb. Sci. 341, 76–83. https://doi.org/10.1016/j.memsci.2009.05.044

Brückl, L., Hahn, R., Sergi, M., Scheler, S., 2016a. A systematic evaluation of mechanisms, material effects, and protein-dependent differences on friction-related protein particle formation in formulation and filling steps. Int. J. Pharm. 511, 931–945. https://doi.org/10.1016/j.ijpharm.2016.08.006

Brückl, L., Schröder, T., Scheler, S., Hahn, R., Sonderegger, C., 2016b. The Effect of Shear on the Structural Conformation of rhGH and IgG1 in Free Solution. J. Pharm. Sci. 105, 1810–1818. https://doi.org/10.1016/j.xphs.2016.03.020

Byron Bird, R., Stewart, W.E., Lightfoot, E.N., 2002. Transport Phenomena, Second Edi. ed. John Wiley & Sons, Inc., New York, NY.

Callahan, D.J., Stanley, B., Li, Y., 2014. Control of protein particle formation during ultrafiltration/diafiltration through interfacial protection. J. Pharm. Sci. 103, 862–869. https://doi.org/10.1002/jps.23861

Campesi, A., Cerri, M.O., Hokka, C.O., Badino, A.C., 2009. Determination of the average shear rate in a stirred and aerated tank bioreactor. Bioprocess Biosyst. Eng. 32, 241–248. https://doi.org/10.1007/s00449-008-0242-4

Capozzi, L.C., Arsiccio, A., Sparavigna, A.C., Pisano, R., Barresi, A.A., 2018. Image segmentation and 3D reconstruction for improved prediction of the sublimation rate during freeze, in: 21st International Drying Symposum.

Carpenter, J.F., Kendrick, B.S., Chang, B.S., Manning, M.C., Randolph, T.W., 1999. Inhibition of stress-induced aggregation of protein therapeutics. Methods Enzymol. 309, 236–255. https://doi.org/10.1016/S0076-6879(99)09018-7

Carpenter, J.F., Randolph, T.W., Jiskoot, W., Crommelin, D.J.A., Middaugh, C.R., Winter, G., Fan, Y.-X., Kirshner, S., Verthelyi, D., Kozlowski, S., Clouse, K.A., Swann, P.G., Rosenberg, M., Cherney, B., 2009. Overlooking subvisible particles in therapeutic protein products: gaps that may compromise product quality. J. Pharm. Sci. 98, 1201–1205. https://doi.org/10.1002/jps

Charm, S.E., Lai, C.J., 1971. Comparison of ultrafiltration systems for concentration of

biologicals. Biotechnol. Bioeng. 13, 185–202. https://doi.org/10.1002/bit.260130203

Charm, S.E., Wong, B.L., 1970a. Enzyme inactivation with shearing. Biotechnol. Bioeng. 12, 1103–1109. https://doi.org/10.1002/bit.260120615

Charm, S.E., Wong, B.L., 1970b. Shear degradation of fibrinogen in the circulation. Science (80-.). 170.

Chaubard, J.-F., Dessoy, S., Ghislain, Y., Gerkens, P., Barbier, B., Battisti, R., Peeters, L., 2010. Disposable bioreactors for viral vaccine production: challenges and opportunities switching. Biopharm Int. Guid. 22–31.

Conner, J., Wuchterl, D., Lopez, M., Minshall, B., Prusti, R., Boclair, D., Peterson, J., Allen, C., 2014. The Biomanufacturing of Biotechnology Products, Biotechnology Entrepreneurship. Elsevier. https://doi.org/10.1016/B978-0-12-404730-3.00026-9

Converti, A., Del Borghi, M., Ferraiolo, G., Sommariva, C., 1996. Mechanical mixing and biological deactivation: The role of shear stress application time. Chem. Eng. J. 62, 155–167. https://doi.org/10.1016/0923-0467(96)03092-8

Creighton, T.E., 1990. Protein folding. Biochem. J. 270, 1–16. https://doi.org/10.1007/978-981-10-4968-2_2

Cromwell, M.E.M., Hilario, E., Jacobson, F., 2006. Protein aggregation and bioprocessing. AAPS J. 8. https://doi.org/10.1208/aapsj080366

Crowley, P.J., 1999. Excipients as stabilizers. Pharm. Sci. Technol. Today 2, 237–243. https://doi.org/10.1016/S1461-5347(99)00158-3

Das, T.K., Sreedhara, A., Colandene, J.D., Chou, D.K., Filipe, V., Grapentin, C., Searles, J., Christian, T.R., Narhi, L.O., Jiskoot, W., 2022. Stress factors in protein drug product manufacturing and their impact on product quality. J. Pharm. Sci. 111, 868–886. https://doi.org/10.1016/j.xphs.2021.09.030

de Boulard, A., Kienle, K., 2022. Trends in single-use mixing for biomanufacturing with an insight into Lonza Ibex® Solutions. Chemie-Ingenieur-Technik 94, 1962–1967. https://doi.org/10.1002/cite.202200090

Deiringer, N., Leitner, I., Friess, W., 2023. Effect of the tubing material used in peristaltic pumping in tangential flow filtration processes of biopharmaceutics on particle formation and flux. J. Pharm. Sci. 112, 665–672. https://doi.org/10.1016/j.xphs.2022.10.005

Den Engelsman, J., Garidel, P., Smulders, R., Koll, H., Smith, B., Bassarab, S., Seidl, A., Hainzl, O., Jiskoot, W., 2011. Strategies for the assessment of protein aggregates in pharmaceutical biotech product development. Pharm. Res. 28, 920–933. https://doi.org/10.1007/s11095-010-0297-1

Devkate, G., Hardikar, S., Patil, R., 2016. Protein aggregation: A review. Int. J. Biochem. Res. Rev. 14, 1–14. https://doi.org/10.9734/ijbcrr/2016/29829

Di Stasio, E., De Cristofaro, R., 2010. The effect of shear stress on protein conformation: Physical forces operating on biochemical systems: The case of von Willebrand factor. Biophys. Chem. 153, 1–8. https://doi.org/10.1016/j.bpc.2010.07.002

Dippel, J., Handt, S., Stute, B., von Lieres, E., Loewe, T., 2021. Fluid dynamics in pleated

membrane filter devices. Sep. Purif. Technol. 267, 118580.
https://doi.org/10.1016/j.seppur.2021.118580

Dixit, M., 2008. Membranes and filtration: Membrane filtration in the biopharm industry.
Filtr. Sep. 45, 18–21. https://doi.org/10.1016/S0015-1882(08)70294-5

Dobson, J., Kumar, A., Willis, L.F., Tuma, R., Higazi, D.R., Turner, R., Lowe, D.C.,
Ashcroft, A.E., Radford, S.E., Kapur, N., Brockwell, D.J., 2017. Inducing protein
aggregation by extensional flow. Proc. Natl. Acad. Sci. U. S. A. 114, 4673–4678.
https://doi.org/10.1073/pnas.1702724114

Dreckmann, T., Boeuf, J., Ludwig, I.S., Lümkemann, J., Huwyler, J., 2020a. Low volume
aseptic filling: Impact of pump systems on shear stress. Eur. J. Pharm. Biopharm. 147,
10–18. https://doi.org/10.1016/j.ejpb.2019.12.006

Dreckmann, T., Boeuf, J., Ludwig, I.S., Lümkemann, J., Huwyler, J., 2020b. Low volume
aseptic filling: Impact of pump systems on shear stress. Eur. J. Pharm. Biopharm. 147,
10–18. https://doi.org/10.1016/j.ejpb.2019.12.006

du Plessis, A., Broeckhoven, C., Guelpa, A., le Roux, S.G., 2017. Laboratory x-ray micro-
computed tomography: A user guideline for biological samples. Gigascience 6, 1–11.
https://doi.org/10.1093/gigascience/gix027

Du, Z., Motevalian, S.P., Carrillo Conde, B., Reilly, K., Zydney, A.L., 2022. Scale-up issues
during sterile filtration of glycoconjugate vaccines. Biotechnol. Prog. 38, 1–7.
https://doi.org/10.1002/btpr.3260

Duerkop, M., Berger, E., Dürauer, A., Jungbauer, A., 2018a. Impact of Cavitation, High
Shear Stress and Air/Liquid Interfaces on Protein Aggregation. Biotechnol. J. 13.
https://doi.org/10.1002/biot.201800062

Duerkop, M., Berger, E., Dürauer, A., Jungbauer, A., 2018b. Influence of cavitation and high
shear stress on HSA aggregation behavior. Eng. Life Sci. 18, 169–178.
https://doi.org/10.1002/elsc.201700079

Edwards, P.J.B., Kakubayashi, M., Dykstra, R., Pascals, S.M., Williams, M.A.K., 2010.
Rheo-NMR studies of an enzymatic reaction: Evidence of a shear-stable
macromolecular system. Biophys. J. 98, 1986–1994.
https://doi.org/10.1016/j.bpj.2010.01.022

Eibl, R., Eibl, D., 2011. Single-use technology in biopharmaceutical manufacture, Applied
Sciences. John Wiley & Sons, Inc., Hoboken, New Jersey.

Elghobashi, S., 1994. On predicting particle-laden turbulent flows. Appl. Sci. Res. 52, 309–
329. https://doi.org/10.1007/BF00936835

Elias, C.B., Joshi, J.B., 1998. Role of hydrodynamic shear on activity and structure of
proteins. Adv. Biochem. Eng. Biotechnol. 59, 47–71.
https://doi.org/10.1007/bfb0102296

Fallahianbijan, F., Emami, P., Hillsley, J.M., Motevalian, S.P., Conde, B.C., Reilly, K.,
Zydney, A.L., 2021. Effect of membrane pore structure on fouling behavior of
glycoconjugate vaccines. J. Memb. Sci. 619, 118797.
https://doi.org/10.1016/j.memsci.2020.118797

Fernandez-Cerezo, L., Rayat, A.C.M.E., Chatel, A., Pollard, J.M., Lye, G.J., Hoare, M.,

2019. An ultra scale-down method to investigate monoclonal antibody processing during tangential flow filtration using ultrafiltration membranes. Biotechnol. Bioeng. 116, 581–590. https://doi.org/10.1002/bit.26859

Fischer, H., Polikarpov, I., Craievich, A.F., 2009. Average protein density is a molecular-weight-dependent function. Protein Sci. 13, 2825–2828. https://doi.org/10.1110/ps.04688204

Gao, Y., Li, M., Jiang, M., Zhang, Y., Wu, C., Ji, X., 2023. Hemolysis performance analysis and a novel estimation model of roller pump system. Comput. Biol. Med. 159, 106842. https://doi.org/10.1016/j.compbiomed.2023.106842

Giglia, S., Rautio, K., Kazan, G., Backes, K., Blanchard, M., Caulmare, J., 2010. Improving the accuracy of scaling from discs to cartridges for dead end microfiltration of biological fluids. J. Memb. Sci. 365, 347–355. https://doi.org/10.1016/j.memsci.2010.09.032

Giglia, S., Yavorsky, D., 2007. Scaling from discs to pleated devices. PDA J. Pharm. Sci. Technol. 61, 314–323.

Gikanga, B., Chen, Y., Stauch, O.B., Maa, Y.F., 2015. Mixing monoclonal antibody formulations using bottom-mounted mixers: impact of mechanism and design on drug product quality. PDA J. Pharm. Sci. Technol. 69, 284–296. https://doi.org/10.5731/pdajpst.2015.01031

Gostick, J., Khan, Z., Tranter, T., Kok, M., Agnaou, M., Sadeghi, M., Jervis, R., 2019. PoreSpy: A Python Toolkit for Quantitative Analysis of Porous Media Images. J. Open Source Softw. 4, 1296. https://doi.org/10.21105/joss.01296

Guerrero, J., 2021. OpenFOAM advanced training. Dynamic meshes in OpenFOAM [WWW Document]. Wolfdynamics. URL http://www.wolfdynamics.com/training/movingbodies/OF2021/dynamicmeshes_2021_OF8.pdf

Guerrero, J., 2013. Tips and tricks in OpenFOAM [WWW Document]. URL http://www.wolfdynamics.com/wiki/tipsandtricks.pdf

Haindl, S., Stark, J., Dippel, J., Handt, S., Reiche, A., 2020. Scale-up of Microfiltration Processes. Chemie-Ingenieur-Technik 92, 746–758. https://doi.org/10.1002/cite.201900025

Hallow, D.M., Seeger, R.A., Kamaev, P.P., Prado, G.R., LaPlaca, M.C., Prausnitz, M.R., 2008. Shear-induced intracellular loading of cells with molecules by controlled microfluidics. Biotechnol. Bioeng. 99, 846–854. https://doi.org/10.1002/bit

Hawe, A., Wiggenhorn, M., van de Weert, M., Garbe, J.H.O., Mahler, H.-C., Jiskoot, W., 2012. Forced degradation of therapeutic proteins. J. Pharm. Sci. 101, 895–913. https://doi.org/10.1002/jps

Heinzelmann, U., Norderstedt, P.G., Mittelbiberacj, H.-J.K., Maselheim, A.L., Ingerkingen, J.W., 2008. Apparatus for quantifying shear stress on a formulation comprising biomolecules. US 2008/0246945 A1.

Hermeling, S., Crommelin, D.J.A., Schellekens, H., Jiskoot, W., 2004. Structure-immunogenicity relationships of therapeutic proteins. Pharm. Res. 21, 897–903. https://doi.org/10.1023/B:PHAM.0000029275.41323.a6

Hoots, W.K., 2006. Urgent inhibitor issues: targets for expanded research. Haemophilia 12, 107–113. https://doi.org/10.1111/j.1365-2516.2006.01374.x

Hudson, S.D., Sarangapani, P., Pathak, J.A., Migler, K.B., 2015. A Microliter Capillary Rheometer for Characterization of Protein Solutions. J. Pharm. Sci. 104, 678–685. https://doi.org/10.1002/jps.24201

Hussain, M.S., 2019. Modelling and prediction of non-linear scale-up from an Ultra Scale-Down membrane device to process scale tangential flow filtration. University College London.

Ibrahim, M., Wallace, I., Ghazvini, S., Manetz, S., Cordoba-Rodriguez, R., Patel, S.M., 2023. Protein aggregates in inhaled biologics: Challenges and considerations. J. Pharm. Sci. 112, 1341–1344. https://doi.org/10.1016/j.xphs.2023.02.010

ICH, 1996. Guideline for industry ICH Q5C Quality of biotechnological products: Stability testing of biotechnological/biological products [WWW Document]. Fed. Regist. URL https://www.ema.europa.eu/en/documents/scientific-guideline/ich-topic-q-5-c-quality-biotechnological-products-stability-testing-biotechnological/biological-products_en.pdf

Ikeda, Y., Handa, M., Kawano, K., Kamata, T., Murata, M., Araki, Y., Anbo, H., Kawai, Y., Watanabe, K., Itagaki, I., 1991. The role of von Willebrand factor and fibrinogen in platelet aggregation under varying shear stress. J. Clin. Invest. 87, 1234–1240. https://doi.org/10.1172/JCI115124

Inayat, A., Klumpp, M., Lammermann, M., Freund, H., Schwieger, W., 2012. Development of a new pressure drop correlation for open-cell foams based completely on theoretical grounds: Taking into account strut shape and geometric tortuosity. Chem. Eng. J. 704–719.

Iwakawa, N., Morimoto, D., Walinda, E., Shirakawa, M., Sugase, K., 2021. Multiple-State Monitoring of SOD1 Amyloid Formation at Single-Residue Resolution by Rheo-NMR Spectroscopy. J. Am. Chem. Soc. 143, 10604–10613. https://doi.org/10.1021/jacs.1c02974

Jagannathan, B., Marqusee, S., 2013. Protein folding and unfolding under force. Biopolymers 99, 860–869. https://doi.org/10.1002/bip.22321

Jameel, F., Hershenshon, S., 2010. Formulation and process development strategies for manufacturing biopharmaceuticals. John Wiley & Sons, Inc., Hoboken, New Jersey, NJ, USA. https://doi.org/10.1128/AAC.03728-14

James, D.E., Jenkins, A.B., Kraegen, E.W., Chisholm, D.J., 1981. Insulin precipitation in artificial infusion devices. Diabetologia 7, 554–557.

Jaspe, J., Hagen, S.J., 2006. Do protein molecules unfold in a simple shear flow? Biophys. J. 91, 3415–3424. https://doi.org/10.1529/biophysj.106.089367

Johnson, C.R., Hansen, C.D., 2005. The Visualization Handbook. Elsevier Butterworth-Heinermann, Burlington, MA, USA.

Jones, L.S., Kaufmann, A., Middaugh, C.R., 2005. Silicone oil induced aggregation of proteins. J. Pharm. Sci. 94, 918–927. https://doi.org/10.1002/jps.20321

Jørgensen, F., Lambert, P., 2008. Accurate biopharmaceutical dispensing: Peristaltic or piston pumps? Innov. Pharm. Technol. 78–80.

Jornitz, M., Meltzer, T.H., 2008. Promoting patient safety. Pharm. Technol. Eur. 20, 41–45.

Jornitz, M.W., 2020. Filtration and purification in the pharmaceutical industry, Third. ed. CRC Press Taylor & Francis Group, Boca Raton, Florida.

Joyce, M.A., Witchey-Lakshmanan, L.C., 2013. Basic principles of sterile product formulation development, in: Sterile Product Development. Springer, pp. 3–32. https://doi.org/10.1007/978-1-4614-7978-9_1

Junne, S., Neubauer, P., 2018. How scalable and suitable are single-use bioreactors? Curr. Opin. Biotechnol. 53, 240–247. https://doi.org/10.1016/j.copbio.2018.04.003

Kalonia, C.K., Heinrich, F., Curtis, J.E., Raman, S., Miller, M.A., Hudson, S.D., 2018. Protein adsorption and layer formation at the stainless steel–solution interface mediates shear-induced particle formation for an IgG1 monoclonal antibody. Mol. Pharm. 15, 1319–1331. https://doi.org/10.1021/acs.molpharmaceut.7b01127

Karassik, I.J., Messina, J.P., Cooper, P., Heald, C.C., 2001. Pump handbook, Third. ed. McGraw-Hill Companies, Inc, New York, NY, USA.

Katritsis, D., Kaiktsis, L., Chaniotis, A., Pantos, J., Efstathopoulos, E.P., Marmarelis, V., 2007. Wall shear stress: Theoretical considerations and methods of measurement. Prog. Cardiovasc. Dis. 49, 307–329. https://doi.org/10.1016/j.pcad.2006.11.001

Kefayati, S., Milner, J.S., Holdsworth, D.W., Poepping, T.L., 2014. In vitro shear stress measurements using particle image velocimetry in a family of carotid artery models: Effect of stenosis severity, plaque eccentricity, and ulceration. PLoS One 9. https://doi.org/10.1371/journal.pone.0098209

Klespitz, J., Kovács, L., 2014. Peristaltic pumps - A review on working and control possibilities, in: SAMI 2014 - IEEE 12th International Symposium on Applied Machine Intelligence and Informatics, Proceedings. IEEE, pp. 191–194. https://doi.org/10.1109/SAMI.2014.6822404

Kong, S.Y., 2006. Plasmid DNA and Bacterial Artificial Chromosomes Processing for Gene Therapy and Vaccination : Studies on Membrane Sterile Filtration. University College London.

Kopp, M.R.G., Grigolato, F., Zürcher, D., Das, T.K., Chou, D., Wuchner, K., Arosio, P., 2023. Surface-Induced Protein Aggregation and Particle Formation in Biologics: Current Understanding of Mechanisms, Detection and Mitigation Strategies. J. Pharm. Sci. 112, 377–385. https://doi.org/10.1016/j.xphs.2022.10.009

Kovarcik, D.P., 2016. Critical factors for fill-finish manufacturing of biologics [WWW Document]. Bioprocess Int. URL https://www.bioprocessintl.com/fill-finish/critical-factors-for-fill-finish-manufacturing-of-biologics

Krause, M.E., Narang, A.S., Barker, G., Herzer, S., Deshmukh, S., Lan, W., Fichana, D., Wasylyk, J.M., Demirdirek, B., Zhang, L., Fiske, J., McGann, M., Adams, M.L., Gandhi, R.B., 2018. Buffer exchange path influences the stability and viscosity upon storage of a high concentration protein. Eur. J. Pharm. Biopharm. 131, 60–69. https://doi.org/10.1016/j.ejpb.2018.07.014

Krayukhina, E., Fukuhara, A., Uchiyama, S., 2020. Assessment of the injection performance of a tapered needle for use in prefilled biopharmaceutical products. J. Pharm. Sci. 109,

515–523. https://doi.org/10.1016/j.xphs.2019.10.033

Kudela, H., n.d. Turbulent Flow [WWW Document]. URL http://www.itcmp.pwr.wroc.pl/~znmp/dydaktyka/fundam_FM/Lecture_no3_Turbulent_flow_Modelling.pdf

Kumar, A., Martin, J., Kuriyel, R., 2015. Scale-up of sterilizing-grade membrane filters from discs to pleated cartridges: Effects of operating parameters and solution properties. PDA J. Pharm. Sci. Technol. 69, 74–87. https://doi.org/10.5731/pdajpst.2015.01006

Kumar, G., Banerjee, R., Kr Singh, D., Choubey, N., Arnaw, 2020. Mathematics for Machine Learning. J. Math. Sci. Comput. Math. 1, 229–238. https://doi.org/10.15864/jmscm.1208

Lapidus, L.J., 2017. Protein unfolding mechanisms and their effects on folding experiments. F1000Research 6, 1–8. https://doi.org/10.12688/f1000research.12070.1

Lee, S.L., Yang, J.H., 1997. Modeling of darcy-forchheimer drag for fluid flow across a bank of circular cylinders. Int. J. Heat Mass Transf. 40, 3149–3144.

Lehr, H.-A., Brunner, J., Rangoonwala, R., James Kirkpatrick, C., 2002. Particulate matter contamination of intravenous antibiotics aggravates loss of functional capillary density in postischemic striated muscle. Am. J. Respir. Crit. Care Med. 165, 514–520. https://doi.org/10.1164/ajrccm.165.4.2108033

Leiske, D.L., Shieh, I.C., Tse, M.L., 2016. A method to measure protein unfolding at an air–liquid interface. Langmuir 32, 9930–9937. https://doi.org/10.1021/acs.langmuir.6b02267

Levin, M., 2001. Pharmaceutical process scale-up. New York, NY, USA. https://doi.org/10.1201/9781420026658.ch5

Ley, A., Altschuh, P., Thom, V., Selzer, M., Nestler, B., Vana, P., 2018. Characterization of a macro porous polymer membrane at micron-scale by Confocal-Laser-Scanning Microscopy and 3D image analysis. J. Memb. Sci. 564, 543–551. https://doi.org/10.1016/j.memsci.2018.07.062

Li, J., Krause, M.E., Chen, X., Cheng, Y., Dai, W., Hill, J.J., Huang, M., Jordan, S., LaCasse, D., Narhi, L., Shalaev, E., Shieh, I.C., Thomas, J.C., Tu, R., Zheng, S., Zhu, L., 2019. Interfacial stress in the development of biologics: Fundamental understanding, current practice, and duture perspective. AAPS J. 21, 44. https://doi.org/10.1208/s12248-019-0312-3

Li, J., Krause, M.E., Tu, R., 2021. Protein instability at interfaces during drug product development, AAPS Advances in the Pharmaceutical Sciences Series. Springer, Cham, Switzerland.

Li, W., Pots, B.F.M., Brown, B., Kee, K.E., Nesic, S., 2016. A direct measurement of wall shear stress in multiphase flow-Is it an important parameter in CO2 corrosion of carbon steel pipelines? Corros. Sci. 110, 35–45. https://doi.org/10.1016/j.corsci.2016.04.008

Ligon, M., 2020. Applications of filtration in the pharmaceutical industry. Process. Mag.

Lim, F.J., Sundaram, J., Sreedhara, A., 2015. Application of quality by design principles to the drug product technology transfer process, in: Quality by Design of Biopharmaceutical Drug Product Development. Springer Science+Business Media, pp. 661–692. https://doi.org/10.1007/978-1-4939-2316-8_27

Lin, G.L., Pathak, J.A., Kim, D.H., Carlson, M., Riguero, V., Kim, Y.J., Buff, J.S., Fuller, G.G., 2016. Interfacial dilatational deformation accelerates particle formation in monoclonal antibody solutions. Soft Matter 12, 3293–3302. https://doi.org/10.1039/c5sm02830b

Liu, C., Li, Z., 2011. On the validity of the Navier-Stokes equations for nanoscale liquid flows: The role of channel size. AIP Adv. 1. https://doi.org/10.1063/1.3621858

Liu, F., 2016. A thorough description of how wall functions Are Implemented In OpenFOAM, in: Nilsson, H. (Ed.), Proceedings of CFD with OpenSource Software.

Liu, S., Afacan, A., Masliyah, J., 1994. Steady incompressible laminar flow in porous media. Chem. Eng. Sci. https://doi.org/10.1016/0009-2509(94)00168-5

Lopez-Gavilan, P., Barrero-Gil, A., 2023. On the limits of Particle Image Velocimetry with continuous wave lasers. Exp. Therm. Fluid Sci. 144, 110873. https://doi.org/10.1016/j.expthermflusci.2023.110873

Maa, Y.F., Hsu, C.C., 1998. Investigation on fouling mechanisms for recombinant human growth hormone sterile filtration. J. Pharm. Sci. 87, 808–812. https://doi.org/10.1021/js980114x

Maa, Y.F., Hsu, C.C., 1997. Protein denaturation by combined effect of shear and air-liquid interface. Biotechnol. Bioeng. 54, 503–512.

Maa, Y.F., Hsu, C.C., 1996. Effect of high shear on proteins. Biotechnol. Bioeng. 51, 458–465. https://doi.org/10.1002/(SICI)1097-0290(19960820)51:4<458::AID-BIT9>3.0.CO;2-H

Maa, Y.F., Prestrelski, S., 2000. Biopharmaceutical powders particle formation and formulation considerations. Curr. Pharm. Biotechnol. 1, 283–302. https://doi.org/10.2174/1389201003378898

Mahler, H.C., Friess, W., Grauschopf, U., Kiese, S., 2009. Protein aggregation: Pathways, induction factors and analysis. J. Pharm. Sci. 98, 2909–2934. https://doi.org/10.1002/jps.21566

Mahler, H.C., Müller, R., Frieß, W., Delille, A., Matheus, S., 2005. Induction and analysis of aggregates in a liquid IgG1-antibody formulation. Eur. J. Pharm. Biopharm. 59, 407–417. https://doi.org/10.1016/j.ejpb.2004.12.004

Malkus, D.S., Nohel, J.A., Plohr, B.J., 1990. Dynamics of shear flow of a non-Newtonian fluid. J. Comput. Phys. 87, 464–487. https://doi.org/10.1016/0021-9991(90)90261-X

Manopoulos, C., Savva, G., Tsoukalis, A., Vasileiou, G., Rogkas, N., Spitas, V., Tsangaris, S., 2020. Optimal design in roller pump system applications for linear infusion. Computation 8. https://doi.org/10.3390/COMPUTATION8020035

Marcato, A., Santos, J.E., Boccardo, G., Viswanathan, H., Marchisio, D., Prodanović, M., 2023. Prediction of local concentration fields in porous media with chemical reaction using a multi scale convolutional neural network. Chem. Eng. J. 455, 140367. https://doi.org/10.1016/j.cej.2022.140367

McBride, S.A., Tilger, C.F., Sanford, S.P., Tessier, P.M., Hirsa, A.H., 2015. Comparison of Human and Bovine Insulin Amyloidogenesis under Uniform Shear. J. Phys. Chem. B 119, 10426–10433. https://doi.org/10.1021/acs.jpcb.5b04488

Mcconville, F.X., Kessler, S.B., 2019. Scale-up of mixing processes: A primer, in: am Ende, D.J. (Ed.), Chemical Engineering in the Pharmaceutical Industry: R&D to Manufacturing. John Wiley & Sons, Inc., pp. 241–259. https://doi.org/10.1002/9781119600800.ch12

Meltzer, T.H., Jornitz, M.W., 2003. The sterilizing filter and its pore size rating. Am. Pharm. Rev. 1–5.

Menter, F.R., 1994. Two-equation eddy-viscosity turbulence models for engineering applications. AIAA J. 32, 1598–1605. https://doi.org/10.2514/3.12149

Metzner, A.B., Feehs, R.H., Ramos, H.L., Otto, R.E., Tuthill, J.D., 1961. Agitation of viscous Newtonian and non-Newtonian fluids. AIChE J. 7, 3–9. https://doi.org/10.1002/aic.690070103

Meyer, B.K., Coless, L., 2012. Compounding and filling: Drug substance to drug product, in: Therapeutic Protein Drug Products. Woodhead Publishing Limited, pp. 83–95. https://doi.org/10.1016/B978-1-907568-18-3.50005-1

Mignozzi, L., 2022. A novel approach for rotating wheel aerodynamics based on the overset method in OpenFOAM.

Millipore, n.d. Durapore Family Guide [WWW Document]. URL https://www.sigmaaldrich.com/deepweb/assets/sigmaaldrich/product/documents/764/350/durapore-family-guide-pg5075en-mk.pdf (accessed 1.20.23).

Millipore Durapore Membrane Filter, 0.22 μm [WWW Document], n.d. URL https://www.emdmillipore.com/US/en/product/Durapore-Membrane-Filter-0.22m,MM_NF-GVWP04700?ReferrerURL=https%3A%2F%2Fwww.google.com%2F (accessed 1.19.23).

Mirasol, F., 2019. The Principle of Scaling Down. BioPharm Int. 32, 14–17.

Mirro, R., Voll, K., 2009. Which impeller is right for your cell line? [WWW Document]. Bioprocess Int. URL https://www.bioprocessintl.com/cell-line-development/which-impeller-is-right-for-your-cell-line-

Mishra, S., Kumar, V., Sarkar, J., Rathore, A.S., 2021. CFD based mass transfer modeling of a single use bioreactor for production of monoclonal antibody biotherapeutics. Chem. Eng. J. 412, 128592. https://doi.org/10.1016/j.cej.2021.128592

Moino, C., Scutellà, B., Bellini, M., Bourlès, E., Boccardo, G., Pisano, R., 2023. Analysis of the shear stresses in a filling line of parenteral products: The role of tubing. Processes 11, 833. https://doi.org/10.3390/pr11030833

Moreland, K., 2014. The ParaView Tutorial.

Morimoto, D., Walinda, E., Iwakawa, N., Nishizawa, M., Kawata, Y., Yamamoto, A., Shirakawa, M., Scheler, U., Sugase, K., 2017. High-Sensitivity Rheo-NMR Spectroscopy for Protein Studies. Anal. Chem. 89, 7286–7290. https://doi.org/10.1021/acs.analchem.7b01816

Moscariello, J., 2016. Scale-down models: An indispensable tool to biopharmaceutical process development. Glob. Pharm. Supply Chain Trends 19, 48–51.

Mulholland, J.W., Shelton, J.C., Luo, X.Y., 2005. Blood flow and damage by the roller

pumps during cardiopulmonary bypass. J. Fluids Struct. 20, 129–140. https://doi.org/10.1016/j.jfluidstructs.2004.10.008

Murphy, R.P., Riedel, Z.W., Nakatani, M.A., Salipante, P.F., Weston, J.S., Hudson, S.D., Weigandt, K.M., 2020. Capillary RheoSANS: Measuring the rheology and nanostructure of complex fluids at high shear rates. Soft Matter 16, 6285–6293. https://doi.org/10.1039/d0sm00941e

Na, J., Suh, D., Cho, Y.H., Baek, Y., 2022. Comparative Evaluation of the Performance of Sterile Filters for Bioburden Protection and Final Fill in Biopharmaceutical Processes. Membranes (Basel). 12. https://doi.org/10.3390/membranes12050524

Narhi, L.O., Corvari, V., Ripple, D.C., Afonina, N., Cecchini, I., Defelippis, M.R., Garidel, P., Herre, A., Koulov, A. V., Lubiniecki, T., Mahler, H.-C., Mangiagalli, P., Nesta, D., Perez-Ramirez, B., Polozova, A., Rossi, M., Schmidt, R., Simler, R., Singh, S., Spitznagel, T.M., Weiskopf, A., Wuchner, K., 2015. Subvisible (2-100 μm) particle analysis during biotherapeutic drug product development: Part 1, considerations and strategy. J. Pharm. Sci. 104, 1899–1908. https://doi.org/10.1002/jps.24437

Nathan, S.J., Sundran, K.C.S.B., Venkataramana, K.N., Mani, K.R., 2008. Filtration Technique in Vaccine Manufacturing. Adv. Biotech 37–41.

Naughton, J.W., Sheplak, M., 2002. Modern developments in shear-stress measurement. Prog. Aerosp. Sci. 38, 515–570. https://doi.org/10.1016/S0376-0421(02)00031-3

Nayak, A., Colandene, J., Bradford, V., Perkins, M., 2011. Characterization of subvisible particle formation during the filling pump operation of a monoclonal antibody solution. J. Pharm. Sci. 100, 4198–4204. https://doi.org/10.1002/jps

Nema, S., Ludwig, J.D., 2010. Pharmaceutical Dosage Forms, Third. ed. Informa Healthcare, New York, NY, USA. https://doi.org/10.1002/14356007.a19_241

Nesta, D., Nanda, T., He, J., Haas, M., Shpungin, S., Rusanov, I., Sweder, R., Brisbane, C., 2017. Aggregation from shear stress and surface interaction: molecule-specific or universal phenomenon? [WWW Document]. Bioprocess Int. URL https://www.bioprocessintl.com/formulation/aggregation-from-shear-stress-and-surface-interaction-molecule-specific-or-universal-phenomenon-

Ogunyankin, M.O., Deshmukh, S., Krause, M.E., Carvalho, T., Huang, M., Ilott, A., Remy, B., Khossravi, M., 2019. Small-scale tools to assess the impact of interfacial and shear stress on biologic drug products. AAPS PharmSciTech 20, 1–9. https://doi.org/10.1208/s12249-019-1378-z

Ostadfar, A., 2016. Biofluid Flow in Artificial, Assistive and Implantable Devices, in: Biofluid Mechanics - Principles and Applications. Academic Press, pp. 205–242. https://doi.org/10.1016/b978-0-12-802408-9.00005-3

Pace, C.N., Shirley, B.A., Thomson, J.A., 1997. Measuring the conformational stability of a protein. Protein Struct. A Pract. approach.

Palmada, N., Cater, J.E., Cheng, L.K., Suresh, V., 2022. Experimental and Computational Studies of Peristaltic Flow in a Duodenal Model. Fluids 7, 1–15. https://doi.org/10.3390/fluids7010040

Papež, P., Merzel, F., Praprotnik, M., 2023. Rotational Dynamics of a Protein under Shear

Flow Studied by the Eckart Frame Formalism. J. Phys. Chem. B 127, 7231–7243. https://doi.org/10.1021/acs.jpcb.3c02324

Particulate contamination: Sub-visible particles, 2016. , in: European Pharmacopoeia.

Particulate contamination: visible particles, 2008. . Eur. Pharmacopoeia.

Patro, S.Y., Freund, E., Chang, B.S., 2002. Protein formulation and fill-finish operations. Biotechnol. Annu. Rev. 8, 55–84. https://doi.org/10.1016/S1387-2656(02)08004-3

Perevozchikova, T., Nanda, H., Nesta, D.P., Roberts, C.J., 2015. Protein adsorption, desorption, and aggregation mediated by solid-liquid interfaces. J. Pharm. Sci. 104, 1946–1959. https://doi.org/10.1002/jps.24429

Peterson, A., Isberg, E., Schlicht, A., 2007. Capability of filling systems to dispense micro-doses of liquid pharmaceutical product. Pharm. Eng. 27, 1–7.

Peterson, D.M., Stathopoulos, N.A., Giorgio, T.D., Hellums, J.D., Moake, J.L., 1987. Shear-induced platelet aggregation requires von Willebrand factor and platelet membrane glycoproteins Ib and IIb-IIIa. Blood 69, 625–628. https://doi.org/10.1182/blood.v69.2.625.bloodjournal692625

Pham, N.B., Meng, W.S., 2020. Protein aggregation and immunogenicity of biotherapeutics. Int. J. Pharm. 585, 119523. https://doi.org/10.1016/j.ijpharm.2020.119523

Piedmonte, D.M., Gu, J.H., Brych, S.R., Goss, M.M., 2018. Practical considerations for high concentration protein formulations, in: Warne, N.W., Mahler, H.-C. (Eds.), Changelles in Protein Product Development. Springer. https://doi.org/10.1007/978-3-319-90603-4_19

Pillai, S.A., Chobisa, D., Urimi, D., Ravindra, N., 2016. Filters and filtration: A review of mechanisms that impact cost, product quality and patient safety. J. Pharm. Sci. Res. 8, 271–278.

Pope, S.B., 2000. Turbulent Flows. Cambridge University Press, Cambridge.

Pordal, H.S., Matice, C.J., Fry, T.J., 2002. The role of computational fluid dynamics in the pharmaceutical industry. Pharm. Technol. 26, 72–79.

Priebe, P.M., Jornitz, M.W., Meltzer, T.H., 2003. Making an informed membrane filter choice. Bioprocess Int.

Rajan, R., Ahmed, S., Sharma, N., Kumar, N., Debas, A., Matsumura, K., 2021. Review of the current state of protein aggregation inhibition from a materials chemistry perspective: Special focus on polymeric materials. Mater. Adv. 2, 1139–1176. https://doi.org/10.1039/d0ma00760a

Ramstorp, M., 2003. Contamination Control in Practice, Contamination control in practice. WILEY-VCH GmbH & Co. KGaA, Weinheim, Germany. https://doi.org/10.1002/9783527612604

Ratanji, K.D., Derrick, J.P., Dearman, R.J., Kimber, I., 2014. Immunogenicity of therapeutic proteins: Influence of aggregation. J. Immunotoxicol. 11, 99–109. https://doi.org/10.3109/1547691X.2013.821564

Rathore, A.S., Sharma, C., Persad, A., 2012. Use of computational fluid dynamics as a tool for establishing process design space for mixing in a bioreactor. Biotechnol. Prog. 28,

382–391. https://doi.org/10.1002/btpr.745

Rathore, A.S., Sofer, G., 2005. Process validation in manufacturing of biopharmaceuticals. Taylor & Francis Group, LLC, Boca Raton, FL. https://doi.org/10.1201/b13997

Rathore, N., Pranay, P., Bernacki, J., Eu, B., Ji, W., Walls, E., 2012. Characterization of protein rheology and delivery forces for combination products. J. Pharm. Sci. 1–9. https://doi.org/10.1002/jps

Rathore, N., Rajan, R.S., 2008. Current perspectives on stability of protein drug products during formulation, fill and finish operations. Biotechnol. Prog. 24, 504–514. https://doi.org/10.1021/bp070462h

Reipert, B.M., Van Den Helden, P.M.W., Schwarz, H.P., Hausl, C., 2007. Mechanisms of action of immune tolerance induction against factor VIII in patients with congenital haemophilia A and factor VIII inhibitors. Br. J. Haematol. 136, 12–25. https://doi.org/10.1111/j.1365-2141.2006.06359.x

Roffi, K., Li, L., Pantazis, J., 2021. Adsorbed protein film on pump surfaces leads to particle formation during fill-finish manufacturing. Biotechnol. Bioeng. 118, 2947–2957. https://doi.org/10.1002/bit.27801

Roghair, I., Gallucci, F., van Sint Annaland, M., 2014. Novel Developments in Fluidized Bed Membrane Reactor Technology, 1st ed, Advances in Chemical Engineering. Elsevier Inc. https://doi.org/10.1016/B978-0-12-800422-7.00004-2

Rosenberg, A.S., 2006. Effects of protein aggregates: An Immunologic perspective. AAPS J 8, 501–507. https://doi.org/10.1208/aapsj080359

Rospiccio, M., Arsiccio, A., Winter, G., Pisano, R., 2021. The role of cyclodextrins against interface-induced denaturation in pharmaceutical formulations: A molecular dynamics approach. Mol. Pharm. 18, 2322–2333. https://doi.org/10.1021/acs.molpharmaceut.1c00135

Saller, V., Matilainen, J., Grauschopf, U., Bechtold-Peters, K., Mahler, H.-C., Friess, W., 2015. Particle shedding from peristaltic pump tubing in biopharmaceutical drug product manufacturing. J. Pharm. Sci. 104, 1440–1450. https://doi.org/10.1002/jps.24357

Sánchez Pérez, J.A., Rodríguez Porcel, E.M., Casas López, J.L., Fernández Sevilla, J.M., Chisti, Y., 2006. Shear rate in stirred tank and bubble column bioreactors. Chem. Eng. J. 124, 1–5. https://doi.org/10.1016/j.cej.2006.07.002

Sankar Raju. N, 2017. Evoking existing function objects and creating new user-defined function objects for Post-Processing, in: Proceedings of CFD with OpenSource Software. Edited by Nilsson. H.,. https://doi.org/10.17196/OS_CFD#YEAR_2017

Scharnowski, S., Hain, R., Kähler, C.J., 2010. Estimation of reynolds stresses from PIV measurements with single-pixel resolution. 15th Int. Symp. Appl. Laser Tech. to Fluid Mech. 5–8.

Schellekens, H., 2005. Factors influencing the immunogenicity of therapeutic proteins. Nephrol. Dial. Transplant. 20, 3–9. https://doi.org/10.1093/ndt/gfh1092

Schlichting, H., 1979. Boundary Layer Theory, Seventh Ed. ed. McGraw-Hill, Inc., New York.

Schmirler, M., Matěcha, J., Netřebská, H., Ježek, J., Adamec, J., 2013. The measurement of wall shear stress in the low-viscosity liquids. EPJ Web Conf. 45, 1–7. https://doi.org/10.1051/epjconf/20134501084

Scott, D.W., 2009. Sturges' rule. WIRES Comput. Stat. 1, 303–306. https://doi.org/10.1002/wics.035

Sediq, A.S., Van Duijvenvoorde, R.B., Jiskoot, W., Nejadnik, M.R., 2016. No touching! Abrasion of adsorbed protein is the root cause of subvisible particle formation during stirring. J. Pharm. Sci. 105, 519–529. https://doi.org/10.1016/j.xphs.2015.10.003

Serno, T., Carpenter, J.F., Randolph, T.W., Winter, G., 2010. Inhibition of agitation-induced aggregation of an IgG-antibody by hydroxypropyl-β-cyclodextrin. J. Pharm. Sci. 99, 1193–1206. https://doi.org/10.1002/jps.21931

Sharma, A., Khamar, D., Cullen, S., Hayden, A., Hughes, H., 2021. Innovative Drying Technologies for Biopharmaceuticals. Int. J. Pharm. 609, 1–28. https://doi.org/10.1016/j.ijpharm.2021.121115

Sharma, C., Malhotra, D., Rathore, A.S., 2011. Review of computational fluid dynamics applications in biotechnology processes. Biotechnol. Prog. 27, 1497–1510. https://doi.org/10.1002/btpr.689

Shemer, L., Wygnanski, I., Kit, E., 1985. Pulsating flow in a pipe. J. Fluid Mech. 153, 313–337. https://doi.org/10.1017/S0022112085001276

Shire, S.J., 2009. Formulation and manufacturability of biologics. Curr. Opin. Biotechnol. 20, 708–714. https://doi.org/10.1016/j.copbio.2009.10.006

Sieck, J.B., Cordes, T., Budach, W.E., Rhiel, M.H., Suemeghy, Z., Leist, C., Villiger, T.K., Morbidelli, M., Soos, M., 2013. Development of a Scale-Down Model of hydrodynamic stress to study the performance of an industrial CHO cell line under simulated production scale bioreactor conditions. J. Biotechnol. 164, 41–49. https://doi.org/10.1016/j.jbiotec.2012.11.012

Simon, S., Krause, H.J., Weber, C., Peukert, W., 2011. Physical degradation of proteins in well-defined fluid flows studied within a four-roll apparatus. Biotechnol. Bioeng. 108, 2914–2922. https://doi.org/10.1002/bit.23257

Song, X., Throckmorton, A.L., Wood, H.G., Antaki, J.F., Olsen, D.B., 2003. Computational fluid dynamics prediction of blood bamage in a centrifugal pump. Artif. Organs 27, 938–941. https://doi.org/10.1046/j.1525-1594.2003.00026.x

Stigler, J., 2014. Analytical Velocity Profile. Eng. Mech. 21, 371–379.

Talukdar, M.S., Torsaeter, O., Ioannidis, M.A., 2002. Stochastic Reconstruction of Particulate Media from Two-Dimensional Stochastic Reconstruction of Particulate Media from Two-Dimensional Images. J. Colloid Interface Sci. 248, 419–428. https://doi.org/10.1006/jcis.2001.8064

Tavakoli-Keshe, R., Phillips, J.J., Turner, R., Bracewell, D.G., 2014. Understanding the relationship between biotherapeutic protein stability and solid-liquid interfacial shear in constant region mutants of IgG1 and IgG4. J. Pharm. Sci. 103, 437–444. https://doi.org/10.1002/jps.23822

Thite, N.G., Ghazvini, S., Wallace, N., Feldman, N., Calderon, C.P., Randolph, T.W., 2023.

Interfacial Adsorption Controls Particle Formation in Antibody Formulations Subjected to Extensional Flows and Hydrodynamic Shear. J. Pharm. Sci. 112, 2766–2777. https://doi.org/10.1016/j.xphs.2023.07.010

Thomas, C.R., Dunnill, P., 1979. Action of shear on enzymes: Studies with catalase and urease. Biotechnol. Bioeng. 21, 2279–2302. https://doi.org/10.1002/bit.260211209

Thomas, C.R., Geer, D., 2011. Effects of shear on proteins in solution. Biotechnol. Lett. 33, 443–456. https://doi.org/10.1007/s10529-010-0469-4

Tisovska, P., 2019. Description of the overset mesh approach in ESI version of OpenFOAM, in: Proceedings of CFD with OpenSource Software. Edited by Nilsson. H.,. https://doi.org/10.17196/OS_CFD#YEAR_2019

Trinh, K.T., 2010. On the Blasius correlation for friction factors.

Tu, J., Yeoh, G.-H., Liu, C., 2018. Computational Fluid Dynamics. Elsevier Ltd. https://doi.org/10.1016/b978-0-08-101127-0.00003-9

Tukey, J.W., 1977. Exploratory Data Analysis. Addison-Wesley Publishing Company, USA.

Tyagi, A.K., Randolph, T.W., Dong, A., Maloney, K.M., Hitscherich Jr., C., Carpenter, J.F., 2009. IgG particle formation during filling pump operation: a case study of heterogeneous nucleation on stainless steel nanoparticles. J. Pharm. Sci. 98, 94–104. https://doi.org/10.1002/jps

U.S. Department of Health and Human Services Food and Drug Administration, 2009. ICH Q8(R2) Pharmaceutical Development. Work. Qual. by Des. Pharm. 8.

USP 29-NF 24, 2006. Injections. United States Pharmacopoeia Convention, Inc., Rockville, MD, USA.

USP 788, 2006. Particulate matter in injections [WWW Document]. URL https://www.uspnf.com/sites/default/files/usp_pdf/EN/USPNF/788ParticulateMatter.pdf

Van Der Veen, M.E., Van Iersel, D.G., Van Der Goot, A.J., Boom, R.M., 2004. Shear-induced inactivation of α-amylase in a plain shear field. Biotechnol. Prog. 20, 1140–1145. https://doi.org/10.1021/bp049976w

van Hooff, T., Blocken, B., Tominaga, Y., 2017. On the accuracy of CFD simulations of cross-ventilation flows for a generic isolated building: Comparison of RANS, LES and experiments. Build. Environ. 114, 148–165. https://doi.org/10.1016/j.buildenv.2016.12.019

Vásárhelyi, L., Kónya, Z., Kukovecz, Vajtai, R., 2020. Microcomputed tomography–based characterization of advanced materials: a review. Mater. Today Adv. 8, 1–13. https://doi.org/10.1016/j.mtadv.2020.100084

Velali, E., Dippel, J., Stute, B., Handt, S., Loewe, T., von Lieres, E., 2020. Model-based performance analysis of pleated filters with non-woven layers. Sep. Purif. Technol. 250, 1–22. https://doi.org/10.1016/j.seppur.2020.117006

Versteeg, H.K., Malalasekera, W., 2007. An Introduction to Computational Fluid Dynamics, Second Edi. ed. Pearson Education, Inc., Harlow. https://doi.org/10.1109/mcc.1998.736434

Viscosity and shear stresses [WWW Document], n.d. URL

https://www.homepages.ucl.ac.uk/~uceseug/Fluids2/Notes_Viscosity.pdf (accessed 6.9.23).

Wang, W., Nema, S., Teagarden, D., 2010. Protein aggregation-Pathways and influencing factors. Int. J. Pharm. 390, 89–99. https://doi.org/10.1016/j.ijpharm.2010.02.025

Wang, W., Singh, S.K., Li, N., Toler, M.R., King, K.R., Nema, S., 2012. Immunogenicity of protein aggregates - Concerns and realities. Int. J. Pharm. 431, 1–11. https://doi.org/10.1016/j.ijpharm.2012.04.040

Weisenfeld, S., Podolsky, S., Goldsmith, L., Ziff, L., 1968. Adsorption of insulin to infusion bottles and tubing. Diabetes 17, 766–771. https://doi.org/10.2337/diab.17.12.766

Werner, B.P., Winter, G., 2015. Particle contamination of parenteralia and in-line filtration of proteinaceous drugs. Int. J. Pharm. 496, 250–267. https://doi.org/10.1016/j.ijpharm.2015.10.082

Whitaker, S., 2013. The method of volume averaging. Springer Science+Business Media.

White, F.M., 2006. Viscous fluid flow, Third. ed. McGraw-Hill Companies, Inc, New York, NY, USA.

Whitford, D., 2005. Proteins structure and function. John Wildey & Sons, Ltd, Chichester, England.

WHO, 2005. Annex 4 WHO guidelines for sampling of pharmaceutical. WHO Guidel. Sampl. Pharm. Prod. Relat. Mater. 61–93.

WHO, 1996. Guidelines for stability testing of pharmaceutical products containing well established drug substances in conventional dosage forms. World Health Organ. Tech. Rep. Ser. 65–80.

Wilcox, D.C., 1994. Turbulence Modeling for CFD. DCW Industries, Inc., La Canada, CA.

Winter, K.G., 1979. An outline of the techniques available for the measurement of skin friction in turbulent boundary layers. Prog. Aerosp. Sci. 18, 1–57. https://doi.org/10.1016/0376-0421(77)90002-1

Womersley, J.R., 1955. Method for the calculation of velocity, rate of flow and viscous drag in arteries when the pressure gradient is known. J. Physiol. 127, 553–563. https://doi.org/10.1113/jphysiol.1955.sp005276

Wu, H., Randolph, T.W., 2020. Aggregation and particle formation during pumping of an antibody formulation are controlled by electrostatic interactions between pump surfaces and protein Molecules. J. Pharm. Sci. 109, 1473–1482. https://doi.org/10.1016/j.xphs.2020.01.023

Xiao, X., Long, A., Qian, K., Zeng, X., Hua, T., 2017. Through-thickness permeability of woven fabric under increasing air pressure: Theoretical framework and simulation. Text. Res. J. 87, 1631–1642. https://doi.org/10.1177/0040517516657062

Zanowiak, P., 2000. Pharmaceutical Dosage Forms, Ullmann's Encyclopedia of Industrial Chemistry. https://doi.org/10.1007/978-1-4684-3444-6_2

Zhan, C., Bidkhori, G., Schwarz, H., Malm, M., Mebrahtu, A., Field, R., Sellick, C., Hatton, D., Varley, P., Mardinoglu, A., Rockberg, J., Chotteau, V., 2020. Low shear stress increases recombinant protein production and high shear stress increases apoptosis in

human cells. iScience 23. https://doi.org/10.1016/j.isci.2020.101653

Zhou, X., Liang, X.M., Zhao, G., Su, Y., Wang, Y., 2014. A New Computational Fluid Dynamics Method for In-Depth Investigation of Flow Dynamics in Roller Pump Systems. Artif. Organs 38, 15–17. https://doi.org/10.1111/aor.12319

Zhou, Y., Sun, B., Chen, M., Cui, C., 2021. Research of flow dynamics and occlusion condition in roller pump systems used for ventricular assist. Artif. Organs 45, E1–E13. https://doi.org/10.1111/aor.13790

Zweifach, B.W., 1955. Structural make up of capillary wall. Ann NY Acad Sci 61, 670–677.

Appendix

A1 Lagrangian Particle Tracking

In the framework of LPT used to track product particles in the peristaltic pump scenario, the dictionary *kinematicCloudProperties* was added in the directory *constant* and some lines were implemented in the controlDict:

```
functions
{
   tracks
        {
                libs ("liblagrangianFunctionObjects.so");
                type icoUncoupledKinematicCloud;
                kinematicCloud kinematicCloud;
        }
};
```

A2 Fittings

Figure A2.1, **Figure A2.2** and **Figure A2.3** display the numerical verification and validation analyses for Y-fitting under laminar conditions and T- and Y-fitting under turbulent conditions.
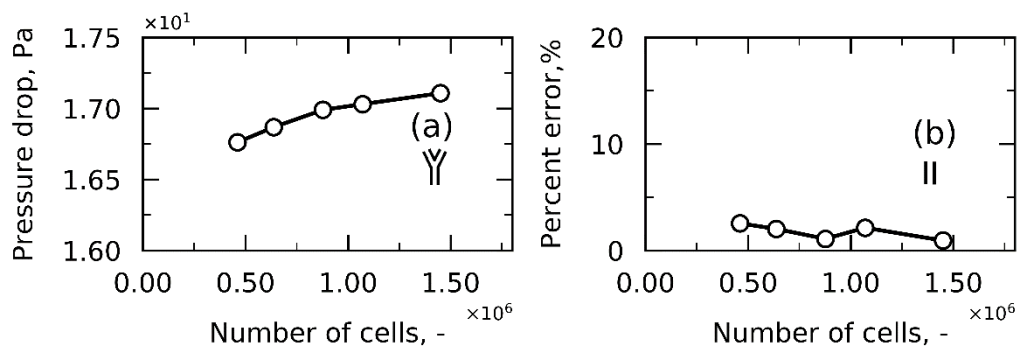
Figure A2.1 Numerical verification and validation analyses for Y-fitting under laminar conditions: grid independence analysis (a), the percent error between the numerical and analytical shear stress in the inlet branch of the fitting (where the fluid dynamics develop as in a tubing) is monitored by varying the number of cells (b).
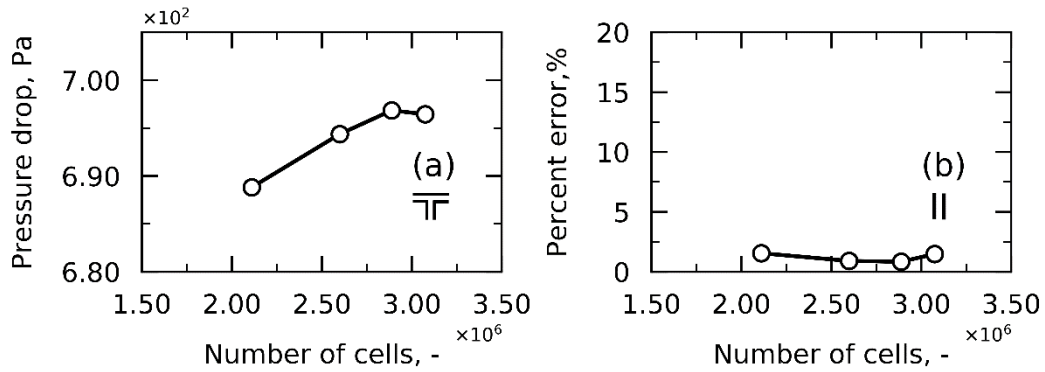
Figure A2.2 Numerical verification and validation analyses for T-fitting under turbulent conditions: grid independence analysis (a), the percent error between the numerical and analytical shear stress in the inlet branch of the fitting (where the fluid dynamics develop as in a tubing) is monitored by varying the number of cells (b).
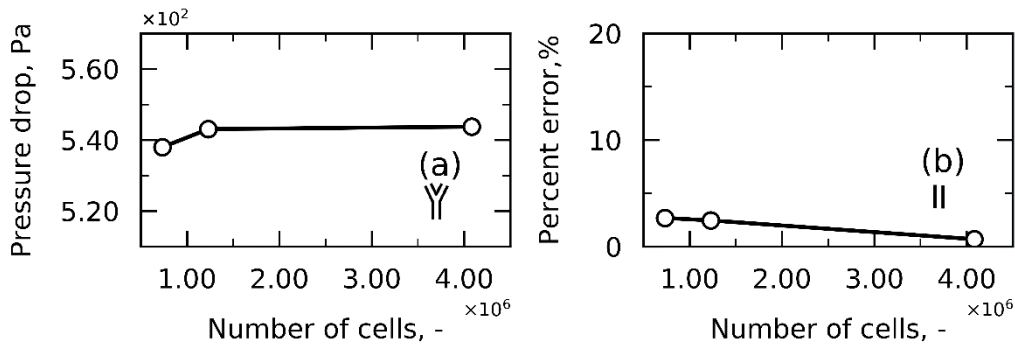
Figure A2.3 Numerical verification and validation analyses for Y-fitting under turbulent conditions: grid independence analysis (a), the percent error between the numerical and the analytical shear stress in the inlet branch of the fitting (where the fluid dynamics develops as in a tubing) is monitored by varying the number of cells (b).

Figure A2.4, **Figure A2.5** and **Figure A2.6** present details of the grid for Y-fitting under laminar conditions and T- and Y-fittings under turbulent conditions.
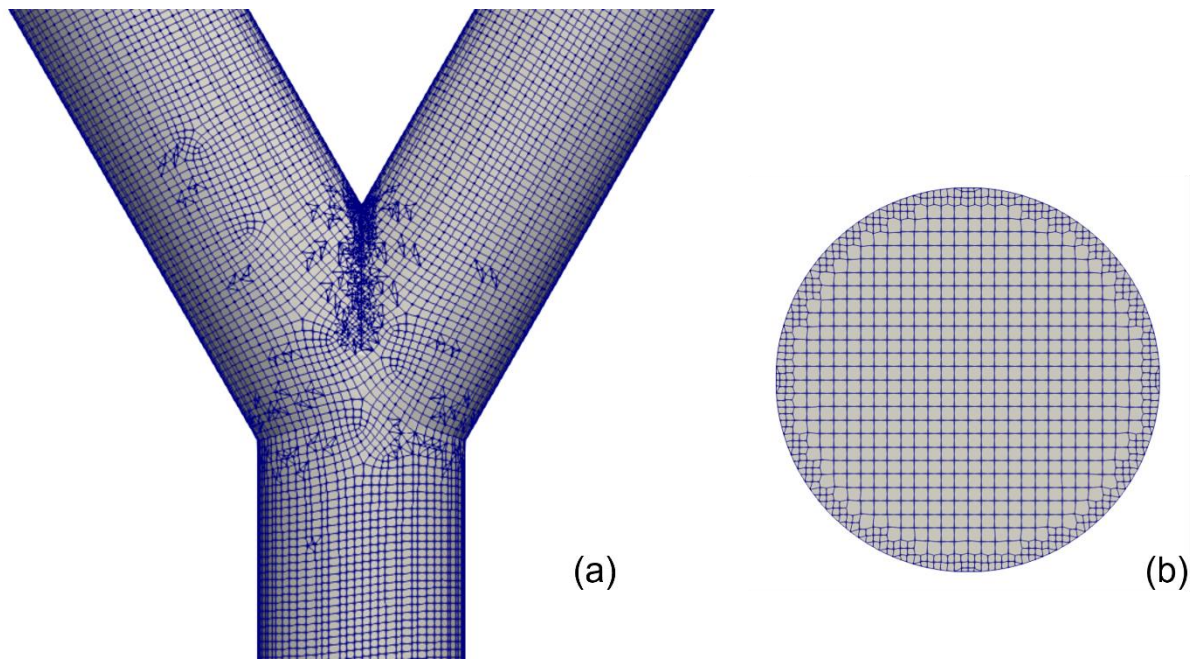
Figure A2.4 Details of the mesh for Y-fitting under laminar conditions: outer mesh (a) and inlet patch mesh (b).
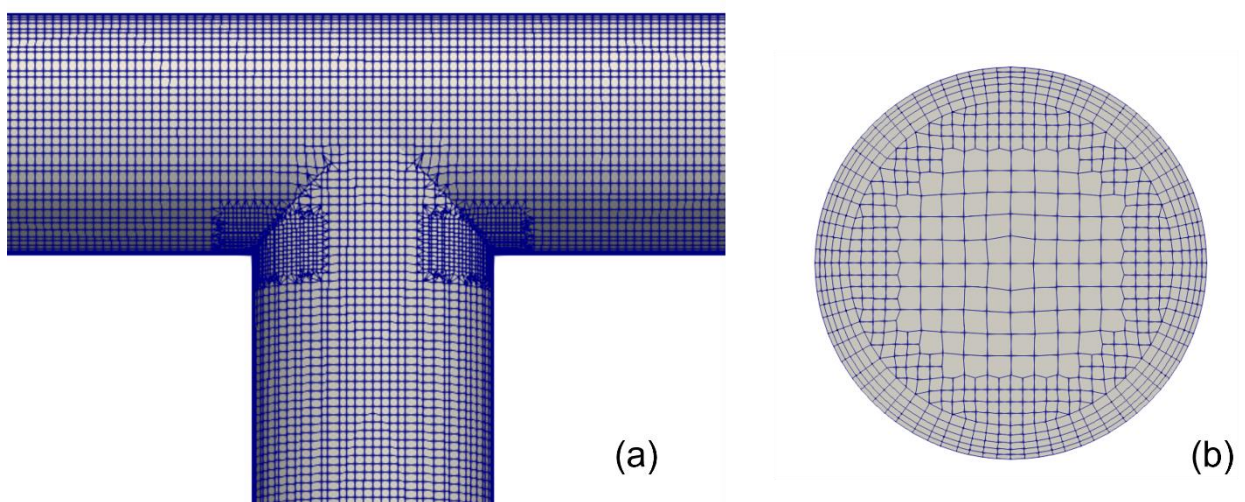
Figure A2.5 Details of the mesh for T-fitting under turbulent conditions: outer mesh (a) and inlet patch mesh (b).
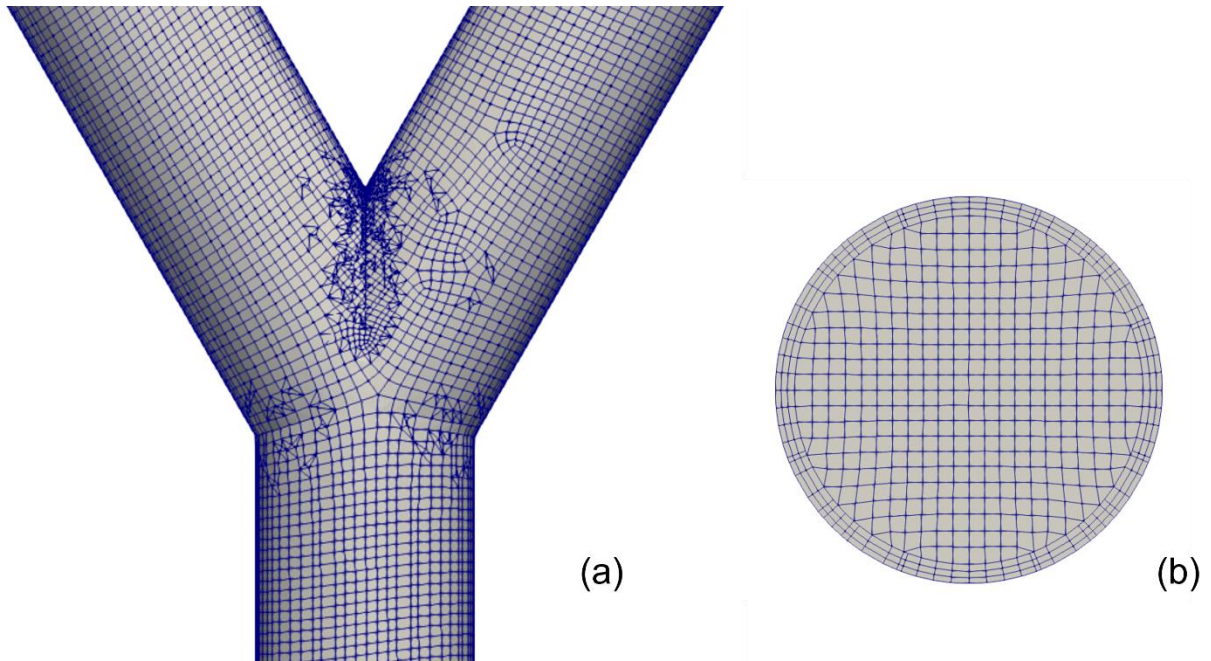
Figure A2.6 Details of the mesh for Y-fitting under turbulent conditions: outer mesh (a) and inlet patch mesh (b).

Figure A2.7 shows an instance of fluid dynamics inside T-fitting (a) and Y-fitting (b) under turbulent conditions; in particular, 520 particles were followed through their trajectories. As for laminar conditions, a 'dead zone' can be seen.
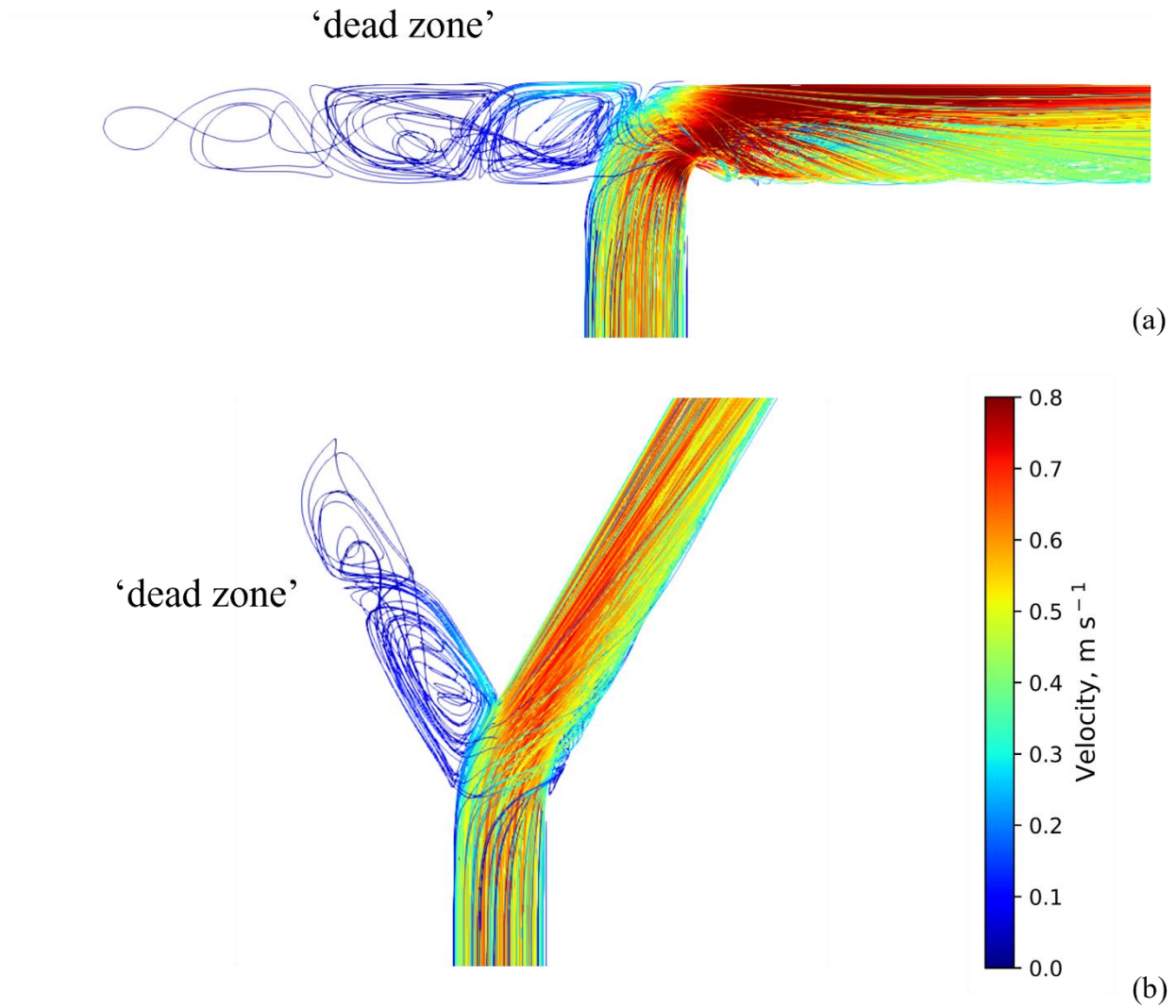
Figure A2.7 A total of 520 particles are followed through their streamlines and their trajectories and velocities are displayed for T-fitting (**a**) and Y-fitting (**b**) under turbulent conditions.

Figure A2.8 and **Figure A2.9** respectively display the frequency histograms for Approaches 3 and 4 for T- and Y-fittings under laminar conditions.
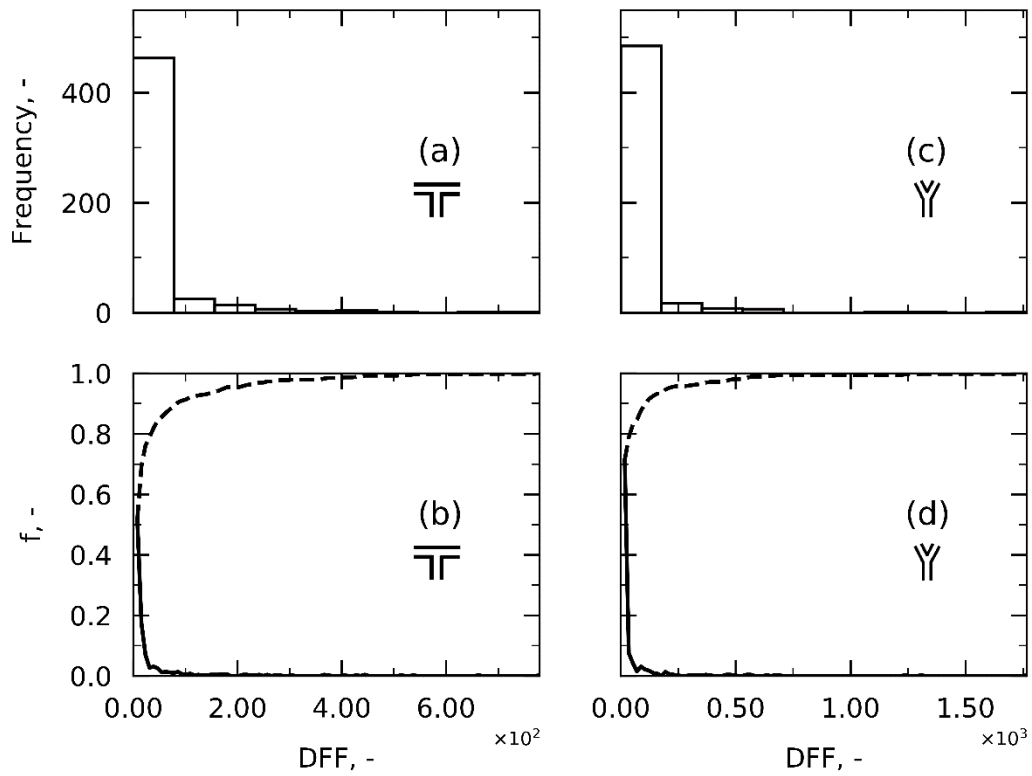
Figure A2.8 Frequency histograms of the *DFF* for T- (a) and Y- (c) fittings under laminar conditions. *PDF* (continuous line) and *CDF* (dotted line) are also presented for T- (b) and Y- (d) fittings.
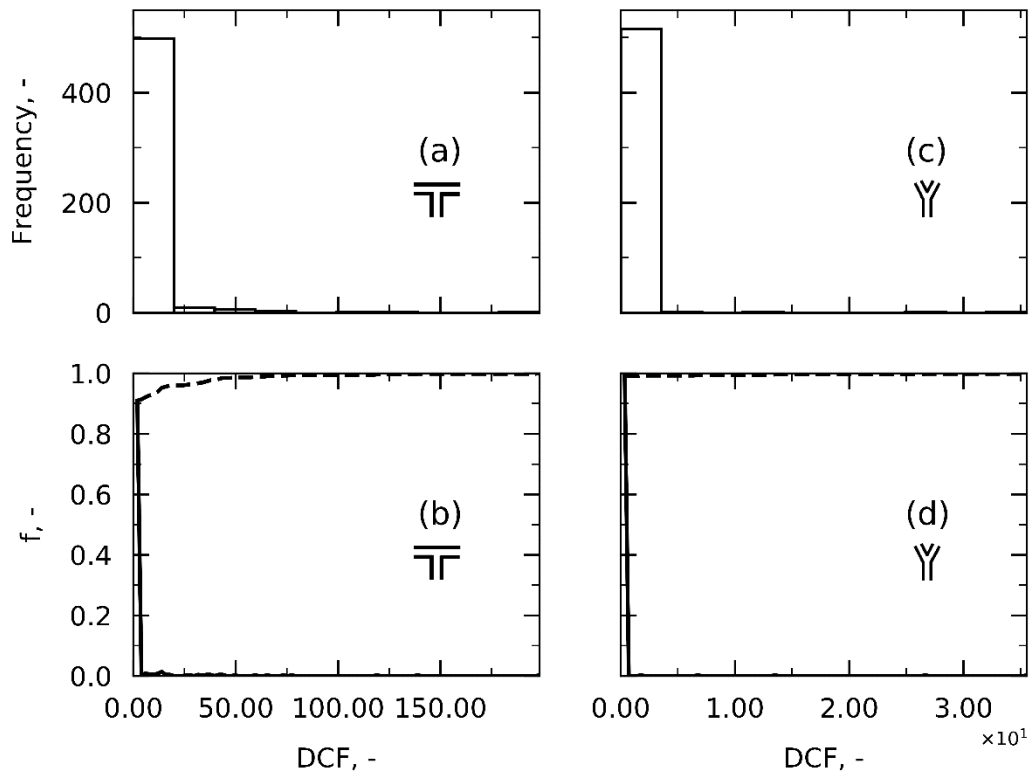
Figure A2.9 Frequency histograms of the *DCF* for T- (a) and Y- (c) fittings under laminar conditions. *PDF* (continuous line) and *CDF* (dotted line) are also presented for T- (b) and Y- (d) fittings.

Figure A2.10, Figure A2.11, Figure A2.12 and Figure A2.13 respectively present the frequency histograms for Approaches 1, 2, 3 and 4 for T- and Y-fittings under turbulent conditions.
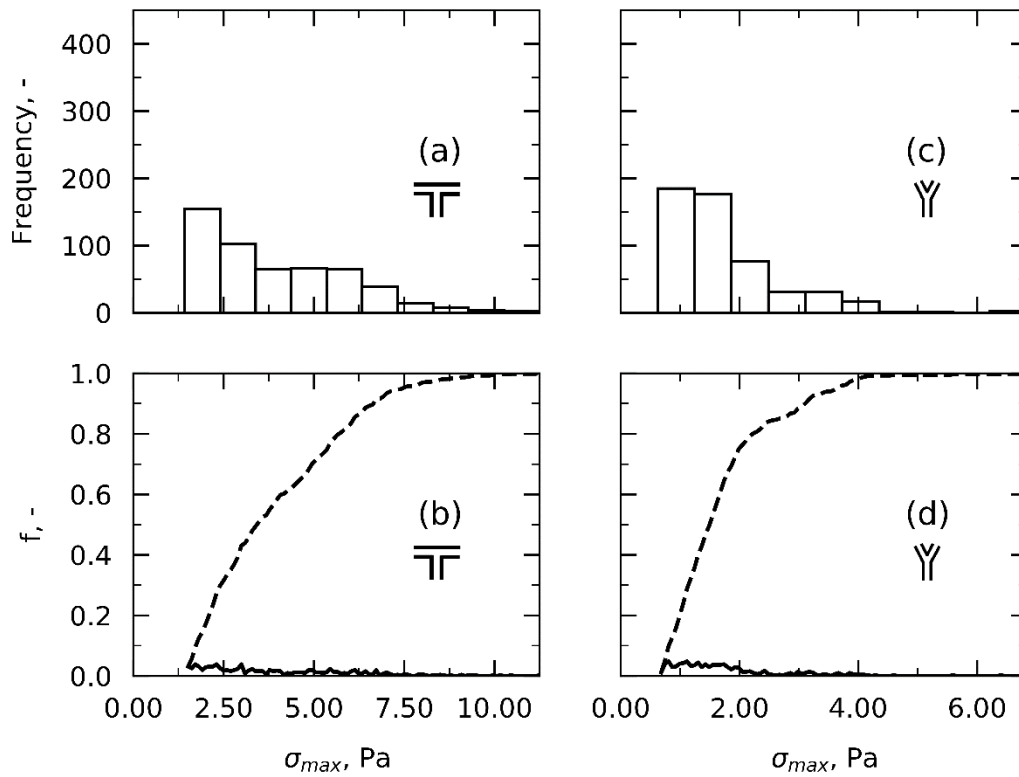

Figure A2.10 Frequency histograms of the maximum shear stress for T- (a) and Y- (c) fittings under turbulent conditions. *PDF* (continuous line) and *CDF* (dotted line) are also presented for T- (b) and Y- (d) fittings.
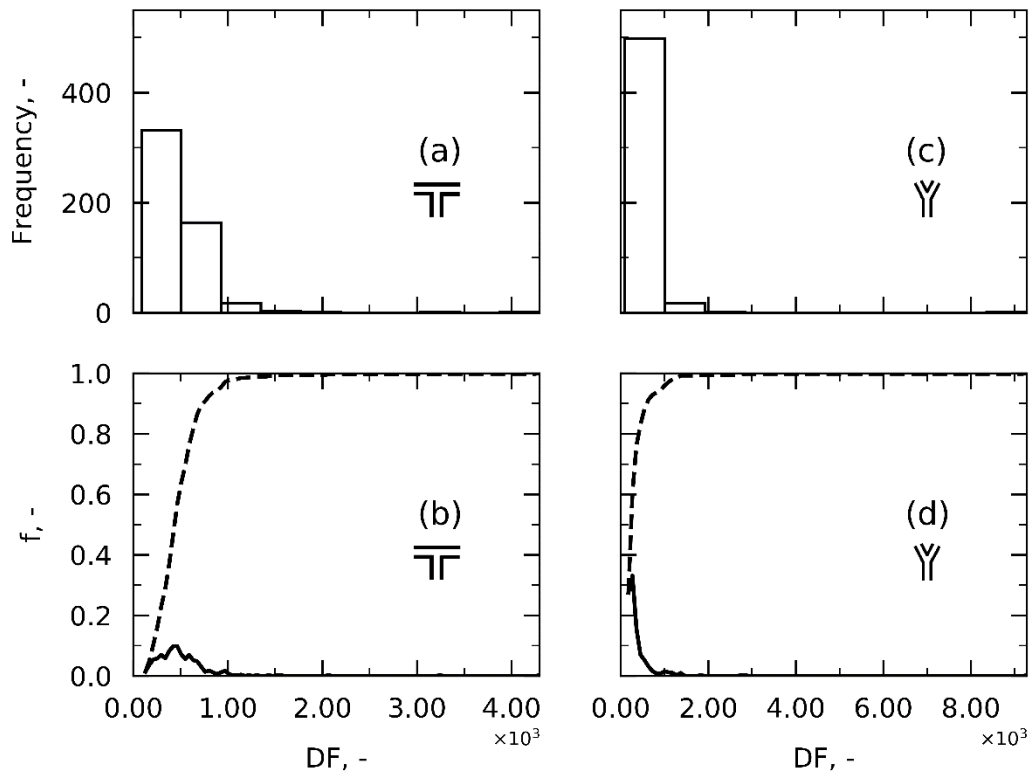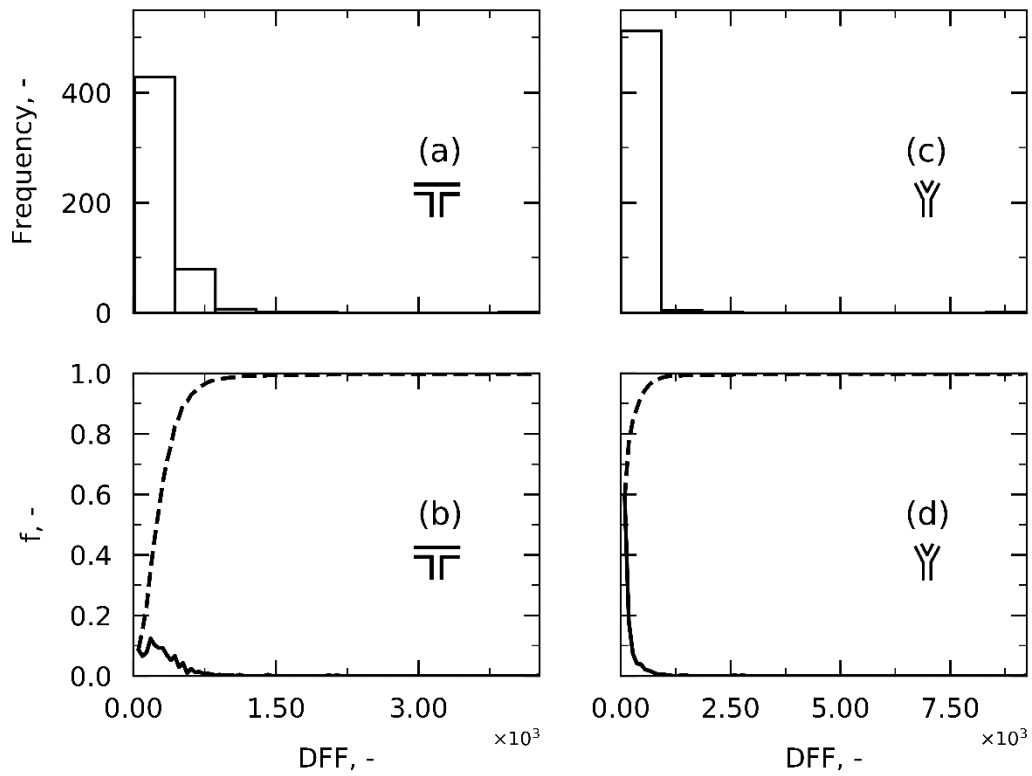
Figure A2.11 Frequency histograms of the *DF* for T- (a) and Y- (c) fittings under turbulent conditions. *PDF* (continuous line) and *CDF* (dotted line) are also presented for T- (b) and Y- (d) fittings.

Figure A2.12 Frequency histograms of the *DFF* for T- (a) and Y- (c) fittings under turbulent conditions. *PDF* (continuous line) and *CDF* (dotted line) are also presented for T- (b) and Y- (d) fittings.

Figure A2.13 Frequency histograms of the *DCF* for T- (a) and Y- (c) fittings under turbulent conditions. *PDF* (continuous line) and *CDF* (dotted line) are also presented for T- (b) and Y- (d) fittings.
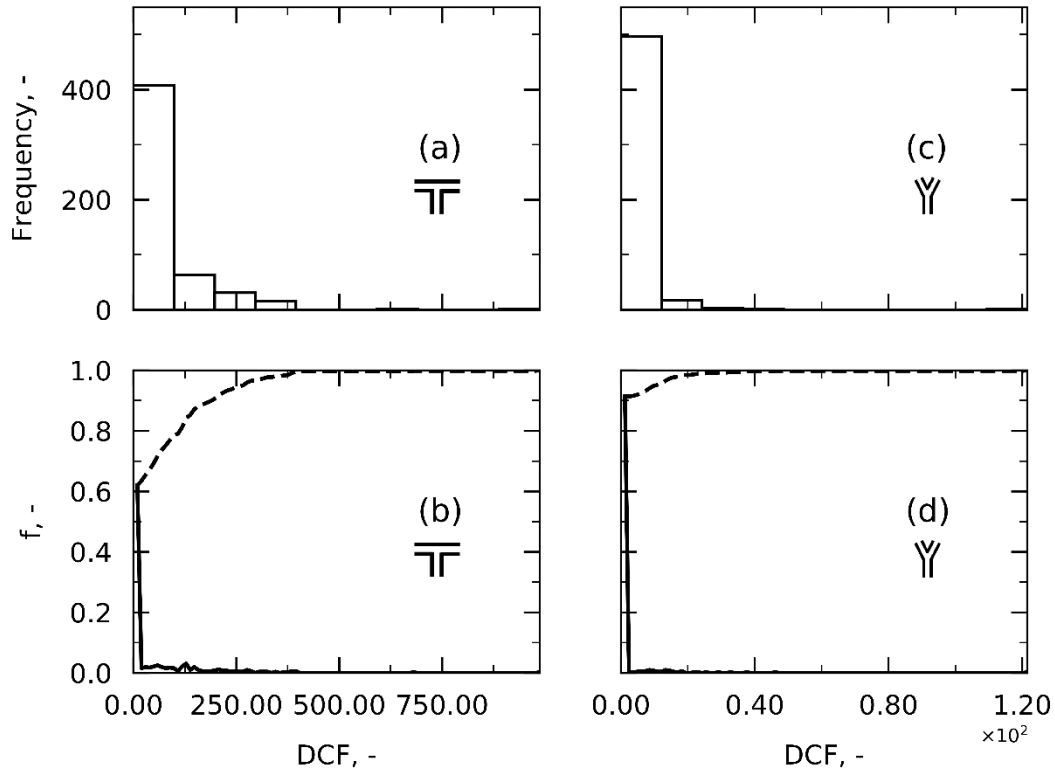
Finally, **Table A2.1** shows the comparison in $\overline{DF}$, $\overline{DFF}$, $\overline{DCF}$ for T- and Y-fittings in turbulent flow. As for laminar flow, it can be observed that when a threshold to the shear rate is introduced ($\overline{DFF}$, $\overline{DCF}$), the cumulative damage decreases within both shapes of fitting.

Table A2.1 Comparison in $\overline{DF}$, $\overline{DFF}$, $\overline{DCF}$ for T- and Y-fittings under turbulent conditions.

Case	$\overline{u}, m\ s^{-1}$	$\overline{DF}, -$	$\overline{DFF}, -$	$\overline{DCF}, -$
T-	0.500	480.37	297.29	53.8
Y-	0.500	340.12	161.07	1.38

A3 Pumping

In the case of a Newtonian and incompressible fluid (like the present case), rate-of-shear tensor and rate-of-strain tensor are the same. Therefore, a functionObject called *shearRate* is implemented and reads as follows:

138

```
bool Foam::functionObjects::shearRate::calc()
{
    if (foundObject<volVectorField>(fieldName_))
    {
        return store
        (
            resultName_,

sqrt(2.0)*mag(symm(fvc::grad(lookupObject<volVectorField>(fieldName_)))
)
        );
    }
    else
    {
        return false;
    }

    return true;

    }
```

```
bool Foam::functionObjects::shearRate::calc()
```